

Stochastic Approaches for Quantification of Near- and Long-Term Structural Reliability

A Dissertation
Presented to
The Academic Faculty

by

Ajay Singh Saini

In Partial Fulfillment
of the Requirements for the Degree
Doctor of Philosophy in the
College of Civil and Environmental Engineering

Georgia Institute of Technology
[December, 2019]

COPYRIGHT © 2019 BY AJAY SINGH SAINI

STOCHASTIC APPROACHES FOR QUANTIFICATION OF NEAR- AND LONG-TERM STRUCTURAL RELIABILITY

Approved by:

Dr. Iris Tien, Advisor
School of Civil and Environmental
Engineering
Georgia Institute of Technology

Dr. Kamran Paynabar
School of Industrial and Systems
Engineering
Georgia Institute of Technology

Dr. Lauren Stewart
School of Civil and Environmental
Engineering
Georgia Institute of Technology

Dr. Lauren Linderman
School of Civil, Environmental, and
Geo-Engineering
University of Minnesota

Dr. Yang Wang
School of Civil and Environmental
Engineering
Georgia Institute of Technology

Date Approved: [11 01, 2019]

ACKNOWLEDGEMENTS

I would like to thank Dr. Iris Tien for providing the opportunity to work on different problems in the field of civil engineering and her mentorship over the years.

I would also like to thank Dr. Lauren Linderman and her research group from University of Minnesota for providing the data from shake table tests for the experimental verification of our proposed methodologies on estimating and predicting the structural response.

I also thank Dr. Branko Glisic and his research group from Princeton University for providing us the data for the Streicker Bridge, which is used to illustrate and analyze the performance of our proposed degradation model.

Table of Contents

| | |
|--|------|
| ACKNOWLEDGEMENTS | iii |
| List of Tables | vii |
| List of Figures | viii |
| Summary | xiii |
| CHAPTER 1. Introduction..... | 1 |
| CHAPTER 2. Motivation..... | 8 |
| CHAPTER 3. Background..... | 13 |
| CHAPTER 4. Near-term reliability: Assessment of nonlinear structural response based on sensor measurements | 19 |
| 4.1 Theoretical study..... | 19 |
| 4.1.1 Introduction..... | 19 |
| 4.1.2 Background and Related Work..... | 21 |
| 4.1.3 Methodology | 23 |
| 4.1.4 Application..... | 37 |
| 4.1.5 Results..... | 41 |
| 4.2 Experimental study | 51 |
| 4.2.1 Introduction..... | 51 |
| 4.2.2 Experimental setup..... | 52 |
| 4.2.3 Evaluation | 54 |
| 4.2.4 Results..... | 55 |
| 4.3 Conclusion | 65 |
| CHAPTER 5. Near-term reliability: Real time prediction of structural seismic risk and a structure-specific earthquake early warning system | 67 |
| 5.1 Theoretical study..... | 67 |
| 5.1.1 Introduction..... | 67 |
| 5.1.2 Background | 69 |
| 5.1.3 Methodology | 71 |
| 5.1.4 Results..... | 81 |

| | | |
|---|--|-----|
| 5.2 | Experimental study | 96 |
| 5.2.1 | Introduction..... | 96 |
| 5.2.2 | Results..... | 96 |
| 5.3 | Conclusion | 101 |
| CHAPTER 6. Long-term reliability: Impacts of climate change on the assessment of long-term reliability | | 103 |
| 6.1 | Introduction..... | 103 |
| 6.2 | Background..... | 104 |
| 6.3 | Methodology | 107 |
| 6.3.1 | Modeling of structural resistance and loads..... | 107 |
| 6.3.2 | Reliability analysis..... | 110 |
| 6.3.3 | Climate change projections..... | 112 |
| 6.4 | Application and results..... | 112 |
| 6.5 | Conclusion | 123 |
| CHAPTER 7. Long-term reliability: A stochastic model for long-term structural degradation | | 125 |
| 7.1 | Introduction..... | 125 |
| 7.2 | Background..... | 125 |
| 7.3 | Methodology | 134 |
| 7.3.1 | Derivation of proposed model..... | 134 |
| 7.3.2 | Parameter estimation..... | 139 |
| 7.4 | Application on data | 141 |
| 7.5 | Results..... | 144 |
| 7.6 | Conclusions..... | 147 |
| CHAPTER 8. Long-term reliability: Estimation of reliability, quantification of resilience, and dynamic resource allocation for repair and maintenance | | 149 |
| 8.1 | Introduction..... | 149 |
| 8.2 | Background and related work | 150 |
| 8.3 | Methodology | 153 |
| 8.3.1 | Flowchart | 153 |
| 8.3.2 | Component reliability | 153 |
| 8.3.3 | Degradation function..... | 155 |
| 8.3.4 | Risk quantification | 156 |

| | | |
|-----------------------------|----------------------------------|-----|
| 8.3.5 | Repair cases | 157 |
| 8.3.6 | Resilience | 160 |
| 8.3.7 | Dynamic resource allocation..... | 161 |
| 8.4 | Application..... | 162 |
| 8.5 | Results..... | 163 |
| 8.6 | Conclusion | 174 |
| CHAPTER 9. Future Work..... | | 176 |
| References..... | | 178 |

LIST OF TABLES

| | |
|--|-----|
| Table 6-1 Performance of the methodology for several earthquakes | 95 |
| Table 6-2 Observed, analytical, and predicted maximum response for different scalings of Chi-Chi earthquake (* indicates LVDT saturation)..... | 98 |
| Table 8-1 Selected degradation modes for concrete, their effects, and estimator models | 129 |
| Table 8-2 Selected degradation modes for steel, their effects, and estimator models | 131 |
| Table 8-3 Selected degradation modes for wood, their effects, and estimator models | 132 |

LIST OF FIGURES

| | |
|--|----|
| Figure 5-1 DBN representation of system evolution | 31 |
| Figure 5-2 10-story shear-type structure..... | 37 |
| Figure 5-3 Sample bedrock excitation w vs. time, where w is normally distributed with time-dependent variance proportional to a gamma PDF..... | 40 |
| Figure 5-4 Interstory drift under input seismic motion for exact and Taylor expansion discretization solutions | 42 |
| Figure 5-5 Estimated interstory drift #5 using EKF vs. UKF..... | 43 |
| Figure 5-6 EKF and UKF estimates at the peak | 44 |
| Figure 5-7 MC realizations of interstory drift #5 compared to actual and UKF response at the peak | 45 |
| Figure 5-8 Analytical and MC distributions of maximum response with respect to various displacement thresholds | 46 |
| Figure 5-9 (a) RMS error and (b) maximum response as a function of increasing c.o.v.'s of structural and ground parameters..... | 48 |
| Figure 5-10 (a) RMS error and (b) estimated maximum response as a function of increasing c.o.v.'s of input motion parameters | 50 |

| | |
|--|----|
| Figure 5-11 RMS errors for varying sensor configurations in terms of number, placement, and precision | 51 |
| Figure 5-12 Experimental setup for the instrumented structure | 53 |
| Figure 5-13 Experimental test setup in the laboratory | 53 |
| Figure 5-14 Comparison of analytical, estimated, and observed interstory displacement for El Centro earthquake | 56 |
| Figure 5-15 Comparison of responses for El Centro earthquake zoomed at the peaks | 57 |
| Figure 5-16 Comparison of estimated and observed response for Kobe earthquake | 58 |
| Figure 5-17 Comparison of responses for Kobe earthquake zoomed at the peaks | 58 |
| Figure 5-18 Comparison of estimated and observed response for Miyagi earthquake..... | 59 |
| Figure 5-19 Comparison of responses for Miyagi earthquake zoomed at the peaks | 59 |
| Figure 5-20 Comparison of estimated and observed response for Chi-Chi earthquake scaled at 10% | 60 |
| Figure 5-21 Comparison of responses for Chi-Chi earthquake at 10% scaling, zoomed at the peaks | 61 |
| Figure 5-22 Comparison of estimated and observed response for a random input excitation..... | 62 |
| Figure 5-23 Comparison of responses for a random excitation zoomed at the peaks | 62 |
| Figure 5-24 RMS Error in response estimate with increasing c.o.v. for structural parameters | 64 |

| | |
|---|-----|
| Figure 5-25 Maximum response estimate with increasing c.o.v. for structural parameters | 65 |
| Figure 6-1 Flowchart of the methodology | 71 |
| Figure 6-2 Characteristics of motion for 3 directional components of ground motion and varying values of ζ_f | 82 |
| Figure 6-3 First 3 seconds of ground acceleration obtained from sensor measurements | 84 |
| Figure 6-4 One realization of simulated ground motion..... | 84 |
| Figure 6-5 Distribution of mean maximum response with varying number of simulations..... | 86 |
| Figure 6-6 RMS error and simulation time vs. number of simulations | 87 |
| Figure 6-7 Distribution of simulated maximum responses and fitted lognormal PDF..... | 89 |
| Figure 6-8 Cumulative probability of simulated maximum response and fitted lognormal CDF | 89 |
| Figure 6-9 Variation of mean maximum response with varying ground damping coefficient ζ_f | 90 |
| Figure 6-10 Variation of mean maximum response with varying m, k, and c | 92 |
| Figure 6-11 Computational time vs number of degrees of freedom of the structure..... | 93 |
| Figure 6-12 Comparison of error in prediction with respect to number of seconds of initial data used and number of ground motion simulations..... | 100 |
| Figure 6-13 Comparison of total computation time with respect to number of seconds of initial data used and number of ground motion simulations | 100 |

| | |
|---|-----|
| Figure 7-1 Probability of failure vs time, with changes in resistance due to environmental factors | 117 |
| Figure 7-2 Probability of failure of example (a) steel and (b) wood structures with change in resistance due to environmental factors | 119 |
| Figure 7-3 Probability of failure vs time, with increase in the extremes of loads, corresponding to an increase of 5%, 10%, and 15% increase in the mean in 100 years | 121 |
| Figure 7-4 Probability of failure vs time, where two different significant load events act on the structure..... | 122 |
| Figure 8-1 Data for strain (left axis) and temperature (right axis) for three years..... | 141 |
| Figure 8-2 Prestressing force over time | 142 |
| Figure 8-3 Results from varying degradation models for third-year testing data..... | 145 |
| Figure 8-4 Total degradation curves over 100 years for varying models | 146 |
| Figure 9-1 Flowchart for the methodology..... | 153 |
| Figure 9-2 Reliability of a component under different repair scenarios..... | 159 |
| Figure 9-3 Representative plan for the Highway Bridge, elevation and cross-sectional views, from [1]..... | 162 |
| Figure 9-4 1000 simulations of reliability for a single component over one year | 164 |
| Figure 9-5 Resilience curve for a single girder..... | 165 |

| | |
|--|-----|
| Figure 9-6 Resilience curves for different reliability thresholds | 166 |
| Figure 9-7 Cost curves for different reliability thresholds..... | 167 |
| Figure 9-8 Resilience distribution with mean and standard deviation for reliability threshold of 0.5 | 168 |
| Figure 9-9 Resilience distribution with mean and standard deviation for reliability threshold of 0.5, zoomed..... | 169 |
| Figure 9-10 Cost distribution for the reliability threshold of 0.5..... | 170 |
| Figure 9-11 Cost distribution for the reliability threshold of 0.5, zoomed..... | 170 |
| Figure 9-12 10 bridge network (a) on the grid, (b) as transportation network | 172 |
| Figure 9-13 Associated weights for the redistribution of load due to component number 3..... | 173 |
| Figure 9-14 Change in the resilience of the network over time due to the shut down of component number 3 for repair | 174 |

SUMMARY

The quantification of structural reliability is an important problem in civil engineering, affecting design decisions and decisions in maintenance, retrofit, and rehabilitation of structures. As structural monitoring data increases, there is the desire to use this data to better estimate and predict the performance of structures, both under extreme loadings such as earthquakes, and over longer time horizons. To facilitate this estimation and prediction, there is the need to create robust models to quantify and predict the reliability of structures. These models are generally stochastic because the physics of structural behavior is too complicated to account for every acting factor and many random external factors will affect the reliability.

The first part of this thesis concentrates on estimating and predicting the near-term reliability of structures under earthquake loading. We propose a methodology based on dynamic Bayesian networks and Kalman filter estimators to utilize building-mounted accelerometer data in real time to estimate the maximum nonlinear response of a structure. We quantify the reliability in terms of the distribution of the maximum response under the earthquake. We analyze the associated uncertainties with the estimation at various steps and the ability of the proposed methodology to perform accurate estimation under increasingly uncertain conditions.

We extend this methodology from real-time estimation to prediction to predict the maximum structural response of a structure for an impending earthquake. We use the data from accelerometers mounted on the structure and predict the amplitude parameters of the earthquake based on the first three seconds of the p-wave data of the impending earthquake. Based on these parameters, we develop a time-sensitive, computationally efficient, and sufficiently accurate

methodology to predict the maximum response of the structure. The methodology quantifies the risk based on allowable maximum response and the distribution of predicted response. We verify the methodologies for the estimation and prediction of maximum response based on experimental data from laboratory tests and show close correspondence between the experimental and theoretical results.

The second part of the study focuses on the quantification of long-term structural reliability. The modeling of lifetime reliability of a structure requires time-dependent modeling of structural resistance and structural loads. First, we focus on the modeling of structural resistance over time. We model the resistance at any time in terms of the degradation of initial resistance over time. We propose a stochastic degradation model as a weighted sum of a random number of different structural degradation modes acting at a time, where each degradation mode is represented by the closest stochastic estimation. We compare and verify the model based on data from a pedestrian bridge.

We then evaluate the effect of environmental and climate parameters to estimate the change in the rate of degradation and occurrence frequency and intensity of loadings. The aim is to quantify the impact of climate change on structural reliability through its effects on the resistance and loading parameters. Climate change affects the rate of degradation and we account for it through time-dependent degradation model parameters. The effect of climate change on the loading parameters is quantified based on regional and global projections. The results show the expected relative changes in structural reliability due to climate change.

The final part is to use the reliability projections to optimize the repair of a structure over its lifetime. We use the estimated reliability and repair projections to quantify the structural resilience

over longer time horizons. The projected resilience is used to analyze the performance of both an individual structure and a network of structures after a shock event. The reliability-based approach for decision-making can be used to optimize the allocation of resources across the infrastructure network to increase disaster preparedness and the reliability of structures across a community.

CHAPTER 1. INTRODUCTION

We rely on quantification and estimation of structural reliability to forecast structural risk over the lifetime of a structure. With the increasing focus on structural resilience, it becomes even more important to be able to accurately quantify the reliability at any instance of time. Quantification of structural reliability supports the optimization of repairs and maintenance of a structure, decision-making for the future, and assessment of structural behavior under risk conditions. Due to the numerous sources of uncertainty in factors affecting structural reliability, stochastic approaches for quantifying structural reliability are needed. We classify structural reliability as near-term and long-term reliability, and propose approaches to quantify structural reliability in both cases. Near-term reliability assesses the state of a structure at a given time, including analyzing the structural performance under a given risk condition. It facilitates drawing inferences on the condition of a structure at a particular instance of time. In comparison, long-term reliability evaluates structural behavior over the lifetime of a structure. It reflects behavior and maintenance demands over longer time horizons to support policy and financial investment decisions. Structural health monitoring data from various sources can be used within the stochastic frameworks to provide a way to utilize the data in the quantification of structural reliability.

There are various ways to quantify the reliability of a structure in both the near-term and long-term. A number of metrics have been proposed depending on the structural system, hazard, data availability, and post-analysis decision-making process. The uncertainty in the structure, hazard exposure, structural response, degradation process, future conditions, and temporal open-endedness make quantification of structural reliability a complex problem. We approach this problem by advancing reliability analysis for both near-term and long-term scenarios. In the near-

term, we quantify the reliability of the structure under seismic loads in terms of the estimated and predicted maximum response of the structure under the load. In the long-term, we evaluate the structural resistance compared to the loading to project reliability over the structural lifetime. Our goal is to define reliability in such a way that it is applicable to any structure and is scalable over structural systems.

As an introduction to the rest of this thesis, our work in near-term reliability is based on using accelerometer data to estimate nonlinear structural response. The estimation procedure is then extended to predict seismic risk for a structure under an impending earthquake based on limited initial information. Inferring the response of a structure is an important task in structural health monitoring, and it is beneficial to be able to do so based on information from simple, non-invasive sensor measurements, e.g., from accelerometers placed sparsely on the structure. With the growing inclusion of nonlinear behavior of a structure in design and analysis, the ability to assess nonlinear structural response is becoming increasingly valuable. A probabilistic approach is required due to uncertainties in both sensor measurements, e.g., with noisy data, and inputs, e.g., under stochastic loadings. We analyze the accelerometer data using an Unscented Kalman Filter (UKF) framework to estimate the structural response in the form of displacement-based responses and interstory drift, without any prior knowledge of the excitation, e.g., an earthquake ground motion. We compare the UKF based formulation with Extended Kalman Filter (EKF) framework and Monte Carlo simulations. We also study the robustness of the methodology under uncertainties in structural parameters. The methodology provides estimates of the maximum structural response using only the accelerometer data, where the distribution of the maximum response can then be used to draw inferences to quantify the reliability of the structure under the seismic excitation.

This methodology to estimate the nonlinear structural response is tested using experimental data from a two-story structure, where we place accelerometers on the structure under excitations from different historical earthquakes. We estimate the structural response using the accelerometer data and the proposed methodology and compare it with the actual structural response. This estimation methodology provides the foundation for the next part of the thesis, which focuses on predicting the maximum structural response under an impending earthquake to quantify structural seismic risk in terms of the maximum predicted response.

The complexity in the nucleation and growth of an earthquake makes it difficult to accurately predict seismic events. We propose an early warning system that goes beyond ground motion prediction to consider the response of the structure itself. The objective is to create a methodology that provides an earthquake early warning based on the anticipated structural response, which is predicted from information from sparsely instrumented buildings rather than relying on extensive seismological data. The proposed localized and structure-specific approach uses collected data to run simulations and create a suite of synthetic accelerograms. These accelerograms are then used to estimate structural responses, with warnings based on predicted maximum responses. Specifically, the methodology first takes the data from an accelerometer placed on the structure and separates the ground motion and structural response in real time. The initial three seconds of p-wave data is used to estimate the characteristics of the earthquake, including moment magnitude, Arias intensity, and hypocentral distance from the structure. A number of ground motions are then simulated based on these parameters. From these, we find the structural response for each simulated ground motion and infer the maximum structural response due to the upcoming earthquake. The future structural response is predicted as the average of the responses to the set of predictive simulated ground motions. The proposed method does not require extensive knowledge

of the regional seismic history, local ground characteristics, or information from additional seismograph stations.

The methodology is experimentally tested using ground motions from historical earthquakes. The prediction of the maximum structural response is based on p-wave data used independently from the experimental excitations of the structure. The predicted maximum response is compared to the experimentally observed response to test the accuracy of the method. We also test the efficacy of the method based on computational time and errors in prediction. The method provides a framework for a structure-specific earthquake early warning system, where the reliability of the structure under an impending earthquake is analyzed in real-time to issue warnings or to support use of active or semi-active control systems.

The next half of the thesis focuses on quantification of the long-term structural reliability. First, we analyze the impact of climate change on structural reliability. Civil engineering infrastructure is required to withstand and resist any weather-based environmental activity. Further, civil engineering infrastructure is designed to function over many decades, where loadings may change over time. As we look over these longer time horizons, it becomes necessary to study the effects of climate change on long-term structural reliability. We study the impacts of climate change by quantifying the individual effects of changes in different environmental factors on the resistance and loading of a structure. The probabilistic assessment of individual variation in both the resistance and load functions at an instant of time allows for the approximation of structural reliability at that time. Performing similar calculations over longer time scales enables estimation of the time-dependent variation of reliability over a duration of time. As infrastructure components are expected to function over long service lifetimes, it becomes important to assess the change in

reliability over the duration of the design life, while simultaneously accounting for the changes in the surroundings and environmental conditions during the time period.

Considering long-term structural reliability, modeling structural degradation becomes an important component of accurately quantifying changes in reliability over time. Most models to estimate structural reliability are based on evaluating a probability of failure. The probability of failure is generally defined as the probability of structural loading exceeding structural strength. Modeling structural strength can be difficult due to the complexity of the processes, mechanisms, and variables affecting structural aging and degradation. We propose a generalized model for the degradation of a structural component. The proposed model is a weighted sum of a random number of degradation modes, where individual degradation modes are estimated as stochastic functions based on their mechanical properties. We also include the terms for the effect of a degradation mode on the rate of another individual degradation mode. Some individual modes are modeled as Poisson arrival processes to reflect those modes that do not affect the structure throughout its lifetime but start acting at a particular time after initial construction. Each individual degradation mode is multiplied by a corresponding weight with simplifications resulting in a proposed degradation model comprising a random sum of a random number of degradation modes. The model parameters can account for the effect of climate change on the structural properties and be learned from structural health monitoring data to project the long-term structural resistance over time.

Moving from reliability to resilience, we then use these proposed long-term structural reliability quantification methodologies to define the resilience of the structure as a function of reliability and repair. We propose a reliability-based approach to quantify the resilience of the structure, introduce repair strategies, and choose the most optimal strategy to maximize resilience and

minimize costs. We simulate structural degradation and live loads to generate individual component reliabilities. We represent the system as a series-parallel combination of individual components to obtain a value of system reliability. We use the estimated system reliability to quantify resilience and predict repair costs over the structural lifetime. We model structural degradation over time and simulate structural live loads to estimate reliability for each component in terms of probability of failure. We then use a system reliability approach to model overall reliability of the structural system based on the individual component reliabilities. We introduce repair criteria and repair cases and estimate structural resilience over time. The end result is a set of cost curves corresponding to different resilience levels of the structure over its lifetime. These curves can be used for decision-making showing the tradeoff between maintenance cost and performance level to achieve optimal repair and maintenance strategies.

Lastly, we extend the approach for structural resilience from an individual structure level to an infrastructure network. The goal is to assess the resilience of the entire network to optimize resource allocation in the near-term in the aftermath of a shock event or in the long-term to optimize network maintenance and expected performance over longer time horizons. The methodology enables prediction of the behavior of network components under different shock events and the prioritization and allocation of resources across the network along with the estimation of cost. It quantifies the resilience of the entire network, while accounting for the effect of repair and maintenance of individual components on the rest of the system. The approach is illustrated using an example bridge network, where we study the performance of the network under shock loading events and assess the performance of the network including flow redistribution due to the downtime of individual network components.

Overall, this project proposes a set of stochastic methodologies for the quantification of near- and long-term structural reliability. Near-term reliability focuses on seismic loads using building-mounted accelerometer data and proposes a structure-specific earthquake early warning system. In the long-term, we introduce a comprehensive methodology to project structural reliability and resilience, which includes the analysis of the effect of climate change on structural reliability, a stochastic degradation function that informs the modeling of structural resistance, quantification of system reliability, and quantification of resilience to optimize repair strategies using projected costs. We finally extend it from a single structure to a network level to quantify network resilience.

CHAPTER 2. MOTIVATION

Aging infrastructure, availability of limited funds, and rapid growth have made it important to assess the near- and long-term behavior of structures. The inferences on structural health are essential in understanding the serviceability of different structural and infrastructure components. There is increasing research focusing on structural health monitoring to address this need. Structural sensors of various kinds have played a vital role in such studies, with growing usage of structural sensors to monitor real-world infrastructure. Different sensors measure different structural or response parameters. The post-processing of the sensor data offers an opportunity to quantify structural risk. In this study, our focus is on using sensor data from different sources to quantify structural reliability. We propose accurate, scalable, and universal methodologies for the post-processing of the data and quantification and assessment of structural reliability.

The methodologies are broadly separated in two categories: 1) the analysis of near-term reliability in real time under seismic loads, and 2) the quantification of long-term reliability and resilience. The first half focuses on estimating structural reliability under stochastic loadings that a structure may experience over its lifetime, primarily earthquakes. We use the data from accelerometers mounted on a structure in real time for the analyses. The analyses in this part use only output data from the accelerometers without any knowledge of the input excitation. This data is used to estimate maximum structural displacement responses based only on the accelerometer measurements. When we have a structure instrumented with accelerometers to record the response under stochastic loads, the post-processing of the data becomes difficult as, unlike laboratory experiments, we generally do not have knowledge of the loading history. The sensors record the total response, which for example in the case of earthquakes, is the earthquake acceleration plus

the structural response acceleration. Structural reliability applications, however, require the relative structural acceleration. In addition, the structural parameters may be uncertain. Our methodology separates the relative structural response and loading history and is able to estimate displacement-based response measures such as interstory drift from accelerometer measurements, including under uncertainty in the structural parameters. The estimation of the structural response is used to quantify the reliability of the structure. It is a robust methodology that processes the sensor data in real-time to estimate maximum nonlinear structural response without any knowledge of the stochastic loading history. A discretization solution for the nonlinear dynamic equation of motion is also derived. From this study, the real-time knowledge of maximum nonlinear response can be used for various inferences on near-term structural reliability as a measure in understanding structural performance under stochastic loadings.

Building on the methodology to estimate structural response using only the accelerometer observations, the next part of this thesis proposes a method to predict localized seismic risk for a structure under an earthquake. The stochastic formulation uses the initial three seconds of p-wave data of an earthquake to infer characteristics of the impending loading event and predict the maximum structural response under the full loading. Based on the prediction maximum, a real-time structure-specific warning can be issued. The overall approach is that an accelerometer placed on the structure records the first three seconds of data, which is then separated into ground acceleration and relative structural acceleration. This data is then used to predict the parameters of the impending earthquake and through a simulation procedure, the maximum structural response is estimated in real-time. Based on the structure and the prediction of the response under the event, a risk-based warning can be issued for the structure. Compared to previous regional ground motion

predictions or earthquake early warning systems, the proposed approach provides a localized structure-specific response prediction based on sparse building-mounted accelerometer data.

The next half of this thesis attempts to understand the long-term behavior of a structure and provide accurate and robust approaches to assess levels of serviceability at a given time. The amount and type of investment needed to achieve an expected target serviceability over the lifetime can then be optimized based on the performance estimates of the structure at any instant. Here, the serviceability of the structure over time is calculated in terms of the structural reliability. The aim of the proposed study is to create a general methodology to estimate long-term structural reliability and use it to optimize the maintenance and investment recommended to increase structural performance and resilience over the service life of the structure. For this case, we propose a general methodology to quantify long-term structural reliability, which incorporates sensor data at different stages to update the reliability estimates throughout the lifetime of the structure. The availability of data about the structure and loadings over its lifetime can be used to update parameters in the structural assessment and improve the accuracy of the methodology over time. However, few, if any, structures provide reliable data over full structural lifetimes. Additionally, the life of a structure spans over several decades. Therefore, a robust general stochastic formulation is required to estimate the reliability and quantify the resilience. In the proposed methodology, the sensor data is used to update the parameters of the stochastic model. Estimation of the system state from the sensor data at different levels of service is integrated with a time-dependent estimation of the structure to predict its long-term behavior and performance.

Traditionally, the resistance of a structure has been estimated independent of the loadings it experiences over its lifetime. The prior loadings, however, will affect the structural strength and performance of the structure under future loads. This research estimates the long-term structural

behavior and reliability accounting for the dependency of structural resistance on loading. To achieve this, we propose a model for structural degradation, where the structural resistance over time is quantified as a function of structural degradation. The parameters of the degradation model are estimated using sensor data. The methodology can use data from simple sensors such as strain gauges or more complex networks of accelerometers mounted on a structure. The parameters of the model are estimated based on structural health monitoring observations from different sensors and updated throughout the lifetime of the structure.

In addition, in assessing reliability over structural lifetimes, the effect of non-stationary environmental conditions is considered. This includes the effect of climate change on both loading and strength in the long term, and combining these effects in the assessment of structural reliability. Climate change affects various environmental parameters, including temperature, carbon dioxide, moisture, etc. The methodology updates the parameters for structural degradation based on periodic sensor observations. In the absence of sensor observations for the structure, the methodology uses regional environmental parameters to quantify the change in environmental loads on the structure. The study also accounts for changing rates and intensities of hazard loadings due to climate change based on regional environmental observations.

The culmination of the research is a comprehensive methodology for the estimation of reliability and resilience for an individual structure and then an infrastructure network. The long-term structural health monitoring observations are used for the quantification of structural degradation, while regional environmental observations help in the quantification of varying structural loads. In addition, the work on real-time structural reliability quantification provides a foundation for the assessment of the impact of shock loads on the long-term reliability of the structure. The methodology for using the sensor observations under seismic loads enables the quantification of

structural resistance in the aftermath of an actual or projected shock event during the lifetime of a structure, so that the parameters and according reliability projections can be updated in real time.

CHAPTER 3. BACKGROUND

This chapter offers the background studies that provide an essential foundation to the methods we propose in later chapters. More detailed background for each of the proposed approaches is provided in their respective sections.

The first part of this thesis focuses on the estimation of near-term reliability and real-time structural response under dynamic loads. It uses the data from accelerometers mounted on the structure. Previously, Tien, Pozzi, and Der Kiureghian [1] proposed a probabilistic framework to infer structural response in the linear range based on accelerometer data. The methodology is based on a dynamic Bayesian network (DBN) framework that models the evolution of structural response under a dynamic excitation over time. The evolution of states within the DBN is estimated using Kalman filters. The study estimates linear structural response under an excitation, without prior knowledge of the excitation, based on the data measured from accelerometers placed on the structure. The accelerometers measure the total acceleration, which is a sum of the excitation and resulting structural acceleration. The methodology is shown to be robust to various uncertainties. However, the methodology changes considerably for a nonlinear structure. Hence, we focus on a nonlinear structure resulting in a generalized method for response estimation.

First we provide an exact discretization solution for the nonlinear equation of motion. The proposed discretization solution draws on the method proposed by Sakamoto, Hori, and Ochi [2]. First, we rearrange the structural equation of motion as a first order differential equation in state-space form. This equation is linearized for each entry of the state vector because it satisfies the partial differential equation condition from [2]. The differential equation is solved using Lagrange characteristic equations.

The study uses an observation matrix of structural accelerations from a random earthquake input including terms for measurement error and ambient noise. Using Kalman estimation methods, the output of the DBN is inference on the mean displacements and velocities at each time step of the data recording and the time-evolving joint probability distribution of the displacement and velocity responses. The extended Kalman filter (EKF) and unscented Kalman filter (UKF) are used. EKF and UKF have been developed to estimate the system state for a dynamically evolving nonlinear system. These two methods can be used to perform computations over the DBN to obtain the marginal system state at every time step and project the trajectory of the evolving system. Kalman [3-4] details the descriptions of the EKF and UKF models. The EKF and UKF have been used in dynamical structural engineering applications in Mariani and Ghisi [5] and other references as indicated in the nonlinear estimation chapter of this thesis.

The estimate for the stochastic distribution of the maximum response is used as the metric to quantify the reliability under the excitation. The probabilistic distribution of the maximum response is obtained as the probability of up-crossings of a non-stationary process as initially formulated by Rice [6] and subsequently derived for non-zero-mean processes in [1]. This employs an approximation of the crossings of the maximum structural response over a safe threshold as Poisson events.

Next, we focus on creating an approach that will provide a structure-specific earthquake early warning based on the predicted maximum response of the structure under an impending earthquake. The development of earthquake early warning systems using real-time seismology dates back to Nakamura's introduction to the concept of using frequency content of p-waves for inferences on the characteristics of an earthquake [6]. The frequency content in the initial few seconds of the p-wave can be analyzed either as the time period of a monochromatic wave (τ_c) or

as the maximum time period (τ_p^{max}). Kanamori [7] extended Nakamura's work to use in practical real-time seismology. Studies by Wu and Kanamori [8-11] show a strong correlation between τ_c and moment magnitude M_w . They developed an early warning system based on the initial three seconds of the p-wave by observing τ_c and the maximum ground displacement P_d . Through the τ_c - P_d method, P_d was found to have a good correlation with the peak ground velocity (PGV) of the approaching earthquake. Allen and Kanamori [12] and Olson and Allen [13] used τ_p^{max} to develop a similar methodology. Through the τ_p^{max} - P_d method, their work shows a strong relationship between τ_p^{max} and M_w . We use the first three seconds of the p-wave data from the accelerometer observations to estimate the characteristics of the earthquake as introduced in these studies. The p-wave ground acceleration is deduced from the accelerometer data by modifying the methodology introduced in the previous section.

Next, we simulate synthetic ground motions using the predicted earthquake parameters. This is done by modulating a normalized white noise process in time as in Rezaeian and Der Kiureghian [14]. We choose a gamma modulating function and estimate the shape parameters based on the intensity, shape, and duration of the motion. Finally, we use the discretization methodology introduced in the previous section to predict maximum structural response corresponding to each realization of simulated synthetic ground motion and predict the expected value of the maximum response under the impending earthquake along with the distribution of the maximum response.

We verify the methodology using experimental data from a shake table test using different excitations for both the estimation and prediction sections. A structure is mounted on a shake table and instrumented with accelerometers to measure the excitation acceleration and the total structural acceleration. LVDTs are also placed at the structure to measure the interstory

displacement. We compare the observed displacement with the estimated displacement based on our formulation using the data collected from accelerometers placed on the structure. The results are also compared with analytical displacements calculated using the discretized equation of motion under the input acceleration.

The second part of this thesis focuses on providing a comprehensive stochastic formulation to quantify long-term structural reliability and the introduction of a resilience metric. We first analyze the effect of climate change on the reliability of structures. There are several extensive climate change models in the literature. The Intergovernmental Panel on Climate Change (IPCC) reports provide the most widely accepted projections of long-term climate patterns. This study uses the mean global climate projections from the IPCC fourth assessment report [15]. These models estimate the change of a quantity projected over a certain number of years. In this study, we assume that the change occurs linearly within the time period of interest. This is in accordance with the fact that the global carbon dioxide level has historically increased approximately linearly. While temperature changes appear to be correlated logarithmically to the carbon dioxide level, the difference between a linear or logarithmic assumption is negligibly small for a change of a few degrees in temperature over several years.

We are interested in quantifying changes in structural reliability over time. Previous studies on time-dependent structural reliability include Li, Wang, and Ellingwood [16] who studied structural reliability under non-stationary loads. They proposed a methodology to model the time-dependent resistance function, subtracting the dead loads to obtain the resultant available resistance, and finding the probability of non-stationary loads exceeding the resistance at any time instant. The time-dependent probability of failure of the structure can be estimated using the distribution of extremes of the expected live loads or environmental loads. While the effect of non-stationary

environmental loads and aging are analyzed in that study, here, we aim to specifically investigate the impact of climate change variables on long-term structural reliability by quantifying the effect on both the resistance and the loading variables.

The modeling of time-dependent structural reliability in [16] under non-stationary loads provides a comparison of different stochastic models for structural degradation. The structural resistance is normalized relative to the initial structural strength and different models for long-term structural degradation are used and compared. We introduce a new stochastic degradation function as a random sum of multiple individual degradation modes, represented by their best estimators from the literature. The parameters of this model are estimated using structural health monitoring data from a pedestrian bridge as an example.

Finally, the last part of this thesis focuses on the long-term projections of structural reliability for an individual structure then expanded to an infrastructure network. The aim is to introduce a reliability-based approach to quantify the resilience of the structure, introduce repair strategies, and choose the optimal strategy to maximize resilience and minimize costs. Reliabilities at the component level for a structure are based on structural resistance and loading as in [16]. Estes and Frangopol [17] proposed a system reliability approach to visualize a bridge as a series-parallel combination of individual components, based on the failure modes and load propagation. Limit-state equations are developed for each failure mode and loads are modeled to calculate the reliability of the bridge system to assess costs for varying rehabilitation approaches. Such an approach is specific to a structure and requires an analyst to identify all the failure modes at the component level. Here, we use a hybrid approach to visualize the system as a series-parallel combination of its components.

Various studies have defined structural resilience in different terms and used different metrics or a combination of multiple metrics to quantify it. An annual resilience metric is proposed by Ouyang, Dueñas-Osorio, and Min [18], which measures actual annual reliability with respect to the target reliability. We look at expected annual resilience while also accounting for repair time in the reliability estimates to quantify resilience. The results provide a set of resilience-cost outcomes and tradeoffs for different levels of desired structural performance over time, and supports selection of an optimal repair and maintenance strategy based on a chosen performance level. The approach is then extended to an infrastructure network to optimize the allocation of resources for the network over time.

CHAPTER 4. NEAR-TERM RELIABILITY: ASSESSMENT OF NONLINEAR STRUCTURAL RESPONSE BASED ON SENSOR MEASUREMENTS

4.1 Theoretical study

4.1.1 Introduction

Inferring the response of a structure is an important task in structural reliability assessment and structural health monitoring, and it is beneficial to be able to do so based on information from simple, non-invasive sensor measurements, e.g., from accelerometers placed sparsely on the structure. With the growing inclusion of nonlinear behavior of a structure in design and analysis, the ability to assess nonlinear structural response is becoming increasingly valuable. A probabilistic approach is required due to uncertainties in both sensor measurements, e.g., with noisy data, and inputs, e.g., under stochastic loadings. Such systems, which are also evolving with time, are effectively visualized as a dynamic Bayesian network (DBN) with states estimated using Kalman-based approaches. In this study, the focus is on real-time processing of the data from accelerometers mounted on the structure to infer the maximum structural response, including maximum interstory drift, when the structure is subjected to unknown stochastic excitations.

Previously, Tien et al 2016 [1] proposed a probabilistic framework to infer structural response in the linear range based on accelerometer data. The methodology, however, changes considerably for nonlinear behavior. The dynamic data in such nonlinear systems can be processed using frameworks such as the extended Kalman filter (EKF) and unscented Kalman filter (UKF). EKF and UKF are able to use the data measured by accelerometers to estimate the structural response,

including displacement-based responses, without any prior knowledge of the excitation, e.g., an earthquake ground motion. This also requires a discretization solution for the continuous system.

The study begins with an observation matrix of structural accelerations due to a random earthquake input, including terms for measurement error and ambient noise. Using Kalman estimation methods, the output of the DBN is inference on the mean displacements and velocities at each time step of the data recording and the time-evolving joint probability distribution of the displacement and velocity responses. This is used in estimating a stochastic distribution of the maximum response. The study demonstrates the ability of the methodology in the nonlinear case to estimate the displacement response from accelerometer measurements and obtain analytical probabilistic distributions of the maximum response exceeding desired response levels for high thresholds. This estimation is shown to be robust to various system uncertainties.

The following section provides background on related work in this area. Next, the proposed framework is described. This includes descriptions of the structural and ground dynamical subsystems, and the derived discretization solution for the continuous system. The methodology for estimating the system state and the distribution of the maximum response is described. The proposed method is then applied to the case of a multi-story shear-type building model under seismic excitation to conduct a theoretical study on the efficacy of the method. Several inference results from this example case are presented, including: comparisons of the two formulations, EKF and UKF; stochastic distributions of interstory drifts; distributions of the maximum structural response; and the effects of parameter uncertainties and varying measurement characteristics on the estimation results. Finally, the results from an experimental study are presented as a verification of the proposed method. The proposed framework supports structural reliability assessment and decision making for structural health monitoring applications, including the design

of effective instrumentation strategies. It provides a basis for the use of accelerometer readings even under conditions of uncertainty to estimate nonlinear structural response.

4.1.2 Background and Related Work

The dynamic Bayesian network (DBN) is a probabilistic framework that models the evolution of a system over time. It is comprised of a sequence of Bayesian networks (BNs) connected by direct links to advance the system at each time step based on the prior information. The reader is referred to literature in [18-20] for an overview of DBNs. Bayesian models have previously been used in various civil and structural engineering applications. This includes work in structural health monitoring to probabilistically measure damage as in [21-22]; for structural model updating as in [23-25]; and for system-level reliability assessment as in [26-27]. In contrast to these previous studies, the goal of this study is to estimate the nonlinear structural response, including displacement-based interstory drifts, based solely on sensor measurements without knowledge of the excitation time history.

To do this, the extended Kalman filter (EKF) and unscented Kalman filter (UKF) are used. EKF and UKF have been developed to estimate the system state for a dynamically evolving nonlinear system. These two methods can be used to perform computations over the DBN to obtain the marginal system state at every time step and project the trajectory of the evolving system. The reader is referred to texts introduced by Kalman in [3] for detailed descriptions of the Kalman, EKF, and UKF models. In the past, EKF and UKF have been used most widely in nonlinear analysis for system identification as in [28-31]; and to identify structural damage through structural parameter approximation as in [32-33]. The UKF has been used in dynamical structural

engineering applications in [5] and for real-time nonlinear structural system identification in [34-36].

In these studies, known excitations are used to identify or update the structural parameters. In this study, however, the excitation is unknown and structural system parameters are assumed to be estimated beforehand. Without knowledge of the ground motion time history, e.g., the accelerogram of the earthquake, the goal is to use only the sensor observations, e.g., from structure-mounted accelerometers, to estimate the system state in real time. The effect of uncertainty or errors in the initial estimation of the structural parameters is investigated later in the study.

In addition, the methodology presented in this paper requires discretization of the continuous dynamical equation of motion, which may not be readily integrable. An exact discretization solution is derived for the equation of motion satisfying a Lagrange PDE condition. Lagrange methods for discretization of nonlinear engineering problems have previously been used in control systems as in [37-38]; mathematical applications such as [39]; and systems with exact discretization solutions such as [2]. The solution described in this paper is specifically for structural response evolution. The exact solution is compared to a second discretization solution derived based on the Taylor expansion. This method of discretization of nonlinear systems has been used for approximate solutions in engineering applications.

To describe the system nonlinearity, the Bouc-Wen model proposed in Bouc 1967 and Wen 1976 [40-41] is used in this study. This model has been widely used in nonlinear structural analysis. In addition to real-time estimation of the structural response, this study is also interested in a probabilistic distribution of the maximum response. To obtain this, the probability of up-crossings of a non-stationary process as initially formulated by Rice 1944 [42] and subsequently derived for

non-zero-mean processes in [1] is used. This employs an approximation of the crossings of the maximum structural response over a safe threshold as Poisson events. Finally, while the methodology is applicable to any stochastic excitation, this study assesses the response of the structure to a seismic excitation in particular. To do this, accelerometer observations under a random earthquake are simulated. The simulation of ground motion is performed as in Rezaeian and Der Kiureghian 2010 [14]. The choice of parameters in the model of the ground excitation is described in the application section of this paper.

The section on experimental verification presents results to verify the methodology using lab data. Previous verification studies using experimental test data focus on analyzing the dynamic characteristics of the structures, seismic performance, and developing performance-based seismic design procedures. For example, full-scale experimental tests have been used to monitor the dynamic response of tall buildings [43], assess the seismic performance of wooden structures under different ground motions [44], and verify the design specifications and understand the seismic behavior of mid-rise structures [45]. Such studies use a known earthquake input and analyze the seismic response of the structure. In contrast, this study assumes no knowledge of the excitation and uses the measurements from accelerometers mounted on the structure to estimate the structural response in real time.

4.1.3 Methodology

The proposed framework consists of two major sections: discretization solution and state estimation. The equation of motion is a second order differential equation while the recorded sensor data is discretized. Therefore, a discretization solution is needed to process the data.

4.1.3.1 Discretization

The dynamical system is modeled as a cascade of two dynamical subsystems. First, the ground dynamical subsystem takes white noise at the bedrock as input and produces an acceleration at the surface. Second, the structural subsystem takes the input ground surface acceleration and produces the output structural response. In this formulation, a capital bold letter (e.g., \mathbf{M}) represents a matrix, a small bold letter (e.g., \mathbf{u}_s) represents a vector and a small italic letter (e.g., a_g) represents a scalar quantity. \mathbf{u} represents displacement while a represents acceleration, and subscripts s and g indicate variables for the structure and ground, respectively.

4.1.3.2 Structural Dynamical Subsystem

In the structural subsystem, nonlinearity may be caused by nonlinear stiffness or damping. The earthquake-induced forces also cause nonlinearity due to P- δ and P- Δ effects. In this study, approximate amplification factor B_2 is used for force nonlinearity, as specified per Appendix 8 of the AISC Steel Construction Manual and calculated using approximate second-order analysis. Nonlinear behavior of a steel structure is considered for this study. However, the methodology may be used for nonlinearity of any structural material.

The equation of motion for the structure subjected to base motion is given by

$$\mathbf{M}\ddot{\mathbf{u}}_s + \mathbf{C}\dot{\mathbf{u}}_s + \mathbf{F}(\mathbf{u}_s) = -B_2\mathbf{M}\mathbf{1}a_g + \mathbf{f} \quad (1)$$

where \mathbf{M} , \mathbf{C} and \mathbf{F} represent the mass, damping and spring force matrices, respectively. \mathbf{f} represents ambient vibrations and additional uncertainty in the external force during the seismic event.

Defining $\mathbf{z}_s^T := [\mathbf{u}_s^T \quad \dot{\mathbf{u}}_s^T]$ in first-order form, the equation of motion is

$$\dot{\mathbf{z}}_s = \begin{bmatrix} \mathbf{0} & \mathbf{I} \\ \mathbf{0} & -\mathbf{M}^{-1}\mathbf{C} \end{bmatrix} \mathbf{z}_s + \begin{bmatrix} \mathbf{0} \\ -\mathbf{M}^{-1}\mathbf{F}(\mathbf{z}_s) \end{bmatrix} + \begin{bmatrix} \mathbf{0} \\ -\mathbf{1} \end{bmatrix} B_2 a_g + \begin{bmatrix} \mathbf{0} \\ \mathbf{M}^{-1} \end{bmatrix} \mathbf{f} \quad (2)$$

where B_2 is defined from AISC specification Appendix 8 as

$$B_2 := \frac{1}{1 - \frac{P_{story}}{P_{estory}}} \quad (3)$$

$$P_{estory} := 0.85 \frac{HL}{\Delta h} \quad (4)$$

H is the total horizontal force at the degree of freedom, L the height of the story, P_{story} the total vertical load supported by the story, and Δh the first order deflection due to H and L .

4.1.3.3 Ground Dynamical Subsystem

The equation of motion for the ground surface with respect to the bedrock-modulated white noise w is given by

$$\ddot{u}_g + 2\xi_g \omega_g \dot{u}_g + \omega_g^2 u_g = -w \quad (5)$$

where the frequency and damping ratio of the ground filter are represented by ω_g and ξ_g , respectively. Defining $\mathbf{z}_g := [u_g \quad \dot{u}_g]^T$, the equation of motion in first-order form is

$$\dot{\mathbf{z}}_g = \begin{bmatrix} 0 & 1 \\ -\omega_g^2 & -2\xi_g \omega_g \end{bmatrix} \mathbf{z}_g + \begin{bmatrix} 0 \\ -1 \end{bmatrix} w \quad (6)$$

The total acceleration at the surface of ground, a_g , is given as

$$a_g = \ddot{u}_g + w = \begin{bmatrix} -\omega_g^2 & -2\xi_g \omega_g \end{bmatrix} \mathbf{z}_g \quad (7)$$

4.1.3.4 State Space Representation

Combining the two subsystems in first-order form and defining $\mathbf{z}^T := [\mathbf{z}_g^T \quad \mathbf{z}_s^T]$ yields the state space representation of the dynamic system as

$$\dot{\mathbf{z}} = \begin{bmatrix} 0 & 1 & \mathbf{0} & \mathbf{0} \\ -\omega_g^2 & -2\xi_g\omega_g & \mathbf{0} & \mathbf{0} \\ \mathbf{0} & \mathbf{0} & \mathbf{0} & \mathbf{I} \\ \mathbf{1}B_2\omega_g^2 & \mathbf{1}2B_2\xi_g\omega_g & \mathbf{0} & -\mathbf{M}^{-1}\mathbf{C} \end{bmatrix} \mathbf{z} + \begin{bmatrix} 0 \\ 0 \\ \mathbf{0} \\ -\mathbf{M}^{-1}\mathbf{F}(\mathbf{z}_s) \end{bmatrix} + \begin{bmatrix} 0 \\ -1 \\ \mathbf{0} \\ \mathbf{0} \end{bmatrix} w + \begin{bmatrix} \mathbf{0} \\ \mathbf{0} \\ \mathbf{0} \\ \mathbf{M}^{-1} \end{bmatrix} \mathbf{f} \quad (8)$$

$$\dot{\mathbf{z}} = \mathbf{A}_c(\mathbf{z}) + \mathbf{b}_c w + \mathbf{B}_c \mathbf{f} \quad (9)$$

4.1.3.5 Discretization Solution: Exact

Next, the continuous system must be discretized in the time domain. A direct integration of the differential form given in Equation (10) cannot be used as the nonlinearity is due to one element of the vector \mathbf{z} and occurs non-uniformly in Equation (9)

$$\int_{\mathbf{z}_k}^{\mathbf{z}_{k+1}} \frac{d\mathbf{z}}{\mathbf{A}_c(\mathbf{z})\mathbf{z} + \mathbf{b}_c w + \mathbf{B}_c \mathbf{f}} = \int_t^{t+\Delta t} dt \quad (10)$$

Therefore, a discretization solution is derived. This exact solution is later verified using a Taylor expansion-based discretization. For the exact solution, the given system, $\dot{\mathbf{z}} = \mathbf{A}_c(\mathbf{z})\mathbf{z} + \mathbf{b}_c w + \mathbf{B}_c \mathbf{f}$, is transformed into a linear system, $\frac{d\mathbf{y}}{dt} = \mathbf{y}(t)$, using a transformation to the differential form $\mathbf{y} = \exp(\mathbf{V}(\mathbf{z})) \mathbf{1}$, where $\mathbf{V}(\mathbf{z})$ is a $n \times n$ matrix as in [2].

Defining $\mathbf{z} = [\mathbf{z}_1 \quad \mathbf{z}_2 \quad \mathbf{z}_3 \quad \mathbf{z}_4]$, linearization is possible if the following condition is satisfied:

$$\mathbf{f}_1(\mathbf{z}, t) \frac{\partial \mathbf{V}(\mathbf{z}, t)}{\partial z_1} + \dots + \mathbf{f}_4(\mathbf{z}, t) \frac{\partial \mathbf{V}(\mathbf{z}, t)}{\partial z_4} = \mathbf{I}_n \quad (11)$$

Here the four governing equations are

$$\dot{z}_1 = \mathbf{f}_1(\mathbf{z}, t) = z_2 \quad (12)$$

$$\dot{z}_2 = \mathbf{f}_2(\mathbf{z}, t) = -\omega_g^2 z_1 - 2\xi_g \omega_g z_2 - w \quad (13)$$

$$\dot{z}_3 = \mathbf{f}_3(\mathbf{z}, t) = z_4 \quad (14)$$

$$\dot{z}_4 = \mathbf{f}_4(\mathbf{z}, t) = \mathbf{1}B_2\omega_g^2 z_1 + \mathbf{1}2B_2\xi_g\omega_g z_2 - \mathbf{M}^{-1}\mathbf{F}(z_3) - \mathbf{M}^{-1}\mathbf{C}z_4 + \mathbf{M}^{-1}\mathbf{f} \quad (15)$$

Unless the damping is nonlinear, the partial differential equations above are linear with respect to their corresponding elements. The treatment for the case of nonlinear damping is described later in this section.

For linearized equations, Lagrange characteristic equations per Equation (11) can be written as

$$\mathbf{f}_j(\mathbf{z}, t) \frac{\partial \mathbf{V}(\mathbf{z}, t)}{\partial z_j} = \mathbf{I}_j \quad j \in [1, 4] \quad (16)$$

Solution of the characteristic equations results in the values of the elements of \mathbf{V} .

Given $\int \frac{dy}{y(t)} = \int dt$ and the transformation for \mathbf{y} , this yields $[\ln(\mathbf{y})]_k^{k+1} = \int dt$ and

$$[(\mathbf{V}(\mathbf{z})\mathbf{1})]_k^{k+1} = \mathbf{I} \int dt \quad (17)$$

Using Equations (12-15) and Equation (16) together, the authors obtain for the elements of \mathbf{V}

$$[\mathbf{V}_{11}]_k^{k+1} z_{2k} = \int_{z_{1k}}^{z_{1k+1}} dz_1 = z_{1k+1} - z_{1k} \quad (18)$$

$$[\mathbf{V}_{22}]_k^{k+1} = \frac{\ln(-\omega_g^2 z_{1k} - 2\xi_g \omega_g z_{2k+1} - w_k) - \ln(-\omega_g^2 z_{1k} - 2\xi_g \omega_g z_{2k} - w_k)}{-2\xi_g \omega_g} \quad (19)$$

$$[\mathbf{V}_{33}]_k^{k+1} = \frac{z_{3_{k+1}} - z_{3_k}}{z_{4_k}} \quad (20)$$

$$[\mathbf{V}_{44}]_k^{k+1} = \text{inv}(-\mathbf{M}^{-1}\mathbf{C}) \left(\ln(\mathbf{1}B_2\omega_g^2 z_{1k} + \mathbf{1}2B_2\xi_g\omega_g z_{2k} - \mathbf{M}^{-1}\mathbf{F}(z_{3_k}) - \mathbf{M}^{-1}\mathbf{C}z_{4_{k+1}} - \mathbf{M}^{-1}\mathbf{f}_k) - \ln(\mathbf{1}B_2\omega_g^2 z_{1k} + \mathbf{1}2B_2\xi_g\omega_g z_{2k} - \mathbf{M}^{-1}\mathbf{F}(z_{3_k}) - \mathbf{M}^{-1}\mathbf{C}z_{4_k} - \mathbf{M}^{-1}\mathbf{f}_k) \right) \quad (21)$$

While nonlinear stiffness is treated here, if damping coefficient C is nonlinear, it can be integrated into Equation (15) according to the nonlinear function. For this study, using Equation (17) and (18-21) together, the following system evolution equations are obtained in discrete time with Δt indicating the discretization time step

$$z_{1_{k+1}} = z_{1_k} + z_{2_k} \Delta t \quad (22)$$

$$z_{2_{k+1}} = \frac{\left[(-\omega_g^2 z_{1_k} - 2\xi_g \omega_g z_{2_k} - w_k) \exp(-2\xi_g \omega_g \Delta t) \right] + w_k + \omega_g^2 z_{1_k}}{-2\xi_g \omega_g} \quad (23)$$

$$\mathbf{z}_{3_{k+1}} = \mathbf{z}_{3_k} + \mathbf{z}_{4_k} \Delta t \quad (24)$$

$$\mathbf{z}_{4_{k+1}} = (-\mathbf{M}\mathbf{C}^{-1}) \left[\{ (\mathbf{1}B_2\omega_g^2 z_{1_k} + \mathbf{1}2B_2\xi_g\omega_g z_{2_k} - \mathbf{M}^{-1}\mathbf{F}(z_{3_k}) - \mathbf{M}^{-1}\mathbf{C}z_{4_k} - \mathbf{M}^{-1}\mathbf{f}_k) \exp(-\mathbf{M}^{-1}\mathbf{C}\Delta t) \} - (-\mathbf{1}B_2\omega_g^2 z_{1_k} - \mathbf{1}2B_2\xi_g\omega_g z_{2_k} + \mathbf{M}^{-1}\mathbf{F}(z_{3_k}) + \mathbf{M}^{-1}\mathbf{f}_k) \right] \quad (25)$$

In matrix form, this can be written as

$$\mathbf{z}_{k+1} = \mathbf{A}_1 \mathbf{z}_k + \mathbf{F}_1 + \mathbf{b}w_k + \mathbf{B}\mathbf{f}_k \quad (26)$$

where

$\mathbf{A}_1 =$

$$\begin{bmatrix} \frac{1}{-\omega_g^2(e^{-2\xi_g\omega_g\Delta t}-1)} & \Delta t & 0 & 0 \\ -2\xi_g\omega_g & e^{-2\xi_g\omega_g\Delta t} & 0 & 0 \\ \mathbf{0} & \mathbf{0} & \mathbf{I} & \mathbf{I}\Delta t \\ B_2\omega_g^2(-\mathbf{M}\mathbf{C}^{-1})(e^{-\mathbf{M}^{-1}\mathbf{C}\Delta t}-\mathbf{I}) & 2B_2\xi_g\omega_g(-\mathbf{M}\mathbf{C}^{-1})(e^{-\mathbf{M}^{-1}\mathbf{C}\Delta t}-\mathbf{I}) & \mathbf{0} & e^{-\mathbf{M}^{-1}\mathbf{C}\Delta t} \end{bmatrix} \quad (27)$$

$$\mathbf{F}_1 = \begin{bmatrix} 0 \\ 0 \\ 0 \\ \mathbf{C}^{-1}(e^{-\mathbf{M}^{-1}\mathbf{C}\Delta t}-\mathbf{I})\mathbf{F}(\mathbf{z}_s) \end{bmatrix} \quad (28)$$

$$\mathbf{b} = \frac{\mathbf{b}_c(e^{-2\xi_g\omega_g\Delta t}-1)}{-2\xi_g\omega_g} \quad (29)$$

$$\mathbf{B} = (-\mathbf{M}\mathbf{C}^{-1})(e^{-\mathbf{M}^{-1}\mathbf{C}\Delta t}-\mathbf{I})\mathbf{B}_c \quad (30)$$

This process yields the exact discretization result for the nonlinear equations modeling the structural response. The accuracy of this solution is only dependent on the discretization step, i.e., the sampling period of the sensor. The method is exact for all other parameters.

4.1.3.6 Discretization Solution: Taylor Expansion

A discretization solution based on an infinite Taylor series expansion of the equation is now provided. This is used to verify the exact solution presented in the previous section. Consider a nonlinear dynamic system with state space given as

$$\dot{\mathbf{z}} = f(\mathbf{z}) + pg(\mathbf{z}) \quad (31)$$

where \mathbf{z} is the state variable, p is the scalar input, and f and g are smooth functions of \mathbf{z} . For such a case, the Taylor method for discretization can be used to obtain an approximate solution. The solution begins with a uniformly convergent Taylor series with coefficients given as functions of successive partial derivatives such that

$$\mathbf{z}_{k+1} = \mathbf{z}_k + \sum_{l=1}^{\infty} \frac{T^l}{l!} \left. \frac{d^l \mathbf{z}}{dt^l} \right|_{t_k} \quad (32)$$

where $T = t_{k+1} - t_k$ is the sampling period and $\mathbf{z}(k)$ is the state space vector at time $t_k = kT$. Equation (32) can be written as

$$\mathbf{z}_{k+1} = \mathbf{z}_k + \sum_{l=1}^{\infty} A^{[l]}(\mathbf{z}_k, p_k) \frac{T^l}{l!} \quad (33)$$

where $A^{[1]}(\mathbf{z}, w) = f(\mathbf{z}) + pg(\mathbf{z})$ and $A^{[l+1]}(\mathbf{z}, w) = \frac{\partial A^{[l]}(\mathbf{z}, u)}{\partial \mathbf{z}} (f(\mathbf{z}) + pg(\mathbf{z})) \quad \forall l \in N$ (*natural*)

As an example, the second order approximation deduced from this result is given as

$$\begin{aligned} \mathbf{z}_{k+1} = \mathbf{z}_k + \{f(\mathbf{z}_k) + p_k g(\mathbf{z}_k)\}T + \left[\frac{\partial f}{\partial \mathbf{z}}(\mathbf{z}_k) f(\mathbf{z}_k) + p_k \left\{ \frac{\partial g}{\partial \mathbf{z}}(\mathbf{z}) f(\mathbf{z}_k) + \frac{\partial f}{\partial \mathbf{z}}(\mathbf{z}_k) g(\mathbf{z}_k) \right\} + \right. \\ \left. p_k^2 \left\{ \frac{\partial g}{\partial \mathbf{z}}(\mathbf{z}) g(\mathbf{z}_k) \right\} \right] \quad (34) \end{aligned}$$

Depending on the type and behavior of the nonlinearity, more terms may be added to obtain a more accurate approximate solution. If the nonlinear function is not differentiable at a given step, however, then this method cannot be used. For example, if the nonlinearity is modeled as bilinear and not differentiable at a specific point, then this method will result in a non-reliable solution. For the nonlinearity used in this study the Taylor expansion solution is applicable. The outcomes from the two discretization solutions are presented in the results section.

4.1.3.7 Estimation

Now, we provide the methodology for estimating the system state as it evolves over time. With the formulation and variables as defined in the previous sections, the graphical dynamic Bayesian network (DBN) representation of the system evolution is shown in Figure (5-1). In sequential BN slices, the system state \mathbf{z} evolves with time based on the input random variables w and \mathbf{f} and the system state at the previous time step. Observations \mathbf{y} (shaded nodes in the DBN) at each time slice are made with some measurement noise \mathbf{v} and conditioned on the system state. The system is visualized to be Bayesian because the state at a time step is estimated from the previous step and then conditioned using the sensor observation at the given step. Kalman filter frameworks are used to perform the updating.

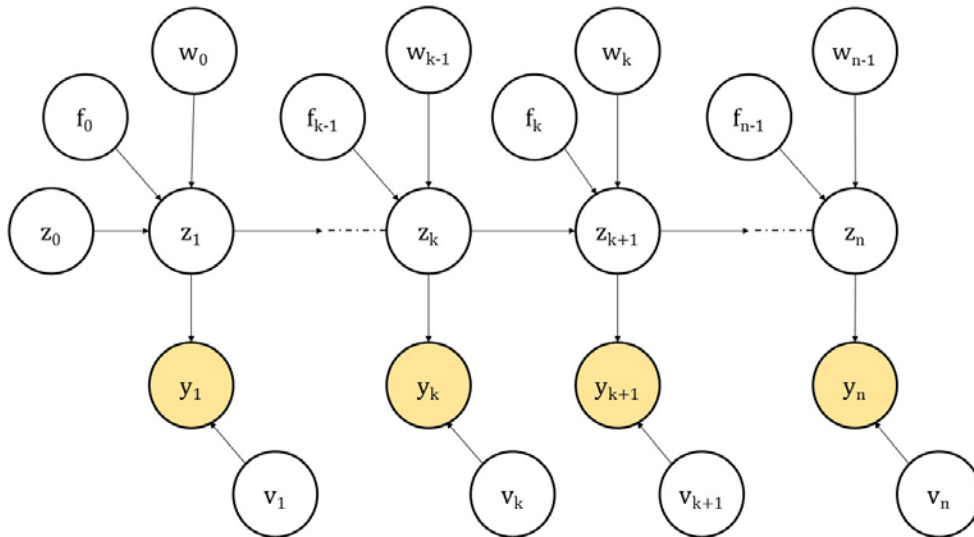


Figure 4-1 DBN representation of system evolution

4.1.3.8 Observation Equation

Observations used to estimate the maximum response are from structure-mounted accelerometers.

The sensors measure the total acceleration of the structure

$$\mathbf{a}_t = \ddot{\mathbf{u}}_s + \mathbf{1}a_g \quad (35)$$

Combining with the equation of motion (1), this can be written as

$$\mathbf{a}_t = -\mathbf{M}^{-1}\mathbf{F}(\mathbf{u}_s) - \mathbf{M}^{-1}\mathbf{C}\dot{\mathbf{u}}_s + \mathbf{M}^{-1}\mathbf{f} \quad (36)$$

Let \mathbf{S} define the matrix that selects the degrees of freedom where accelerometers are placed. The observation equation is then given as

$$\mathbf{y}_k = \mathbf{D}(\mathbf{z}_k) + \mathbf{v}_k + \mathbf{S}\mathbf{M}^{-1}\mathbf{f}_k \quad (37)$$

$$\text{where } \mathbf{D} = -\mathbf{S}\mathbf{M}^{-1}[\mathbf{0} \quad \mathbf{0} \quad \mathbf{0} \quad \mathbf{C}] - \mathbf{S}\mathbf{M}^{-1}\mathbf{F}(\mathbf{u}_s) \quad (38)$$

and v_k is the measurement error, which is taken to be normally distributed with zero mean and time-independent variance σ_v^2 . The effect of the uncertainty in the sensor measurements on the accuracy of the estimation is investigated in the results section. The random noise \mathbf{f} is modeled as a normally distributed zero-mean process with statistically independent variances for each time step and degree of freedom such that the covariance matrix is given by $\sigma_f^2\mathbf{I}$. This random term accounts for ambient noise and additional environmental uncertainties.

4.1.3.9 Extended Kalman Filter (EKF)

Based on the sensor measurements \mathbf{y} , the EKF can be used to estimate the evolution of the nonlinear system state \mathbf{z} . Here, an overview of EKF is presented. The EKF propagates the state

space vector by linearizing all nonlinear mappings about the mean of the previous time step. It is then updated using approximate correctors based on the gradients or Jacobians of the mappings. The framework gives the mean vector and covariance matrix for the system state at every time step.

Consider a system with evolution equation

$$\mathbf{z}_{k+1} = f_k(\mathbf{z}_k) + w_k \quad (39)$$

and observation equation

$$\mathbf{y}_{k+1} = h_{k+1}(\mathbf{z}_{k+1}) + v_{k+1} \quad (40)$$

where $f_k(\mathbf{z}_k)$ represents the system evolution as in Equation (26) and $h_{k+1}(\mathbf{z}_{k+1})$ the sensor observation as in Equation (37). First, the state is predicted based on the expected value of the evolution equation about the mean at the previous time step.

$$\mathbf{z}_{k+1}^p = f(\mathbf{z}_k^F) \quad (41)$$

$$\mathbf{V}_{k+1}^p = Q_k + \nabla f_{k|\mathbf{z}_k^F} V_k^F \nabla f_{k|\mathbf{z}_k^F}^T \quad (42)$$

\mathbf{z} and \mathbf{V} represent, respectively, the mean and variance of a state variable. The superscript p represents values in the predictor phase while F represents final estimated values. Q_k is the variance of input parameter w at time slice t_k .

Next, the estimated value from the predictor phase is corrected through conditioning on the observation matrix. Correction based on the error in the observed value of \mathbf{y} compared to the projected value of \mathbf{y} using the estimated state results in the final estimated mean and variance

$$\mathbf{z}_{k+1}^F = \mathbf{z}_{k+1}^p + \mathbf{V}_{k+1}^p \nabla h_{k+1}^T (\nabla h_{k+1} \mathbf{V}_{k+1}^p \nabla h_{k+1}^T + R_{k+1})^{-1} (\mathbf{y}_{k+1} - h_{k+1}(\mathbf{z}_{k+1}^p)) \quad (43)$$

$$\mathbf{V}_{k+1}^F = \mathbf{V}_{k+1}^p - \mathbf{V}_{k+1}^p \nabla h_{k+1}^T (R_{k+1} + \nabla h_{k+1} \mathbf{V}_{k+1}^p \nabla h_{k+1}^T)^{-1} \nabla h_{k+1} \mathbf{V}_{k+1}^p \quad (44)$$

where R is the variance with respect to v .

4.1.3.10 Unscented Kalman Filter (UKF)

The UKF can also be used to infer the state space vector from observations. Theoretically, it results in more accurate estimates than the EKF for nonlinear problems. The UKF distributes a set of stochastic sigma points for the state vector at each time step and propagates them through the actual nonlinear mapping. The order of accuracy for the mean and covariance obtained through this process depends on the number of sigma points. Sigma points are scattered about the mean of the previous time step and are $2n + 1$ in number, where n is the length of state space vector. The sigma points are weighted such that $\sum_{i=0}^{2n} W = 1$, where W is the weight associated with the i^{th} sigma point.

Values of the sigma points are chosen such that

$$\mathbf{z}_{k-1}^0 = \mathbf{z}_{k-1}^F \quad (45-a)$$

$$\mathbf{z}_{k-1}^j = \mathbf{z}_{k-1}^F + \left(\sqrt{(\psi^2 n) \mathbf{V}_{k-1}^F} \right)_j \quad j \in [1, n] \quad (45-b)$$

$$\mathbf{z}_{k-1}^{j+n} = \mathbf{z}_{k-1}^F - \left(\sqrt{(\psi^2 n) \mathbf{V}_{k-1}^F} \right)_j \quad j \in [1, n] \quad (45-c)$$

where the first sigma point is chosen at \mathbf{z}_{k-1}^F , the mean of the state vector at the previous time step, \mathbf{V}_{k-1}^F is the variance, and ψ^2 is a constant defining the distance of a sigma point from the previous mean.

The weight attached to the mean of each sigma point is given as $W_i^m = \begin{cases} \frac{\psi^2-1}{\psi^2} & i = 0 \\ \frac{1}{2\psi^{2n}} & \text{otherwise} \end{cases}$

(46)

The weight attached to the variance of each sigma point is $W_i^c = \begin{cases} \frac{\psi^2-1}{\psi^2} + 3 - \psi^2 & i = 0 \\ \frac{1}{2\psi^{2n}} & \text{otherwise} \end{cases}$

(47)

In the predictor phase, every sigma point is propagated through the discretization function and the mean and variance of the prediction is calculated using the weights defined in Equations (46) and (47). Estimates of the mean and variance in the predictor phase are given as

$$\mathbf{z}_k^{p,i} = f(\mathbf{z}_{k-1}^i) \quad (48)$$

$$\mathbf{z}_k^p = \sum_{i=0}^{2n} W_i^m \mathbf{z}_k^{p,i} \quad (49)$$

$$\mathbf{V}_k^p = \sum_{i=0}^{2n} W_i^c (\mathbf{z}_k^{p,i} - \mathbf{z}_k^p)(\mathbf{z}_k^{p,i} - \mathbf{z}_k^p)^T + Q_{k-1} \quad (50)$$

where Q_{k-1} is the variance of input parameter w at time slice t_{k-1} .

The predicted values of the mean and variance of the system state are again conditioned using the observation matrix in the corrector phase to produce the final estimated values

$$\mathbf{z}_k^F = \mathbf{z}_k^p + \mathbf{V}_k^p \nabla h_k^T (\nabla h_k \mathbf{V}_k^p \nabla h_k^T + R_k)^{-1} (\mathbf{y}_k - h(\mathbf{x}_k^p)) \quad (51)$$

$$\mathbf{V}_k^F = \mathbf{V}_k^p - \mathbf{V}_k^p \nabla h_k^T (\nabla h_k \mathbf{V}_k^p \nabla h_k^T + R_k)^{-1} \nabla h_{k+1} \mathbf{V}_k^p \quad (52)$$

where R is the variance with respect to v . Estimation accuracy using EKF compared to UKF is given in results section.

4.1.3.11 Distribution of the Maximum Response

The EKF and UKF produce time history estimates of the system state. For reliability problems, the maximum response is of particular interest. To obtain the distribution of the maximum response, the authors use the analytical solution for extreme values of the inferred structural response derived in Tien et al 2016. This is based on an assumption of exceedances of extreme values over safe thresholds as Poisson events, which holds for high thresholds and low-probability events. Thus, the probability of the response in an interval $[0, T]$ exceeding a given threshold value ζ can be approximated by

$$P(Z_{max} > \zeta) = 1 - P(Z_{max} \leq \zeta) \approx 1 - \exp \left[- \int_0^T v(\zeta^+, t) dt \right] \quad (53)$$

where $Z_{max} = \max_t(Z(t))$ is the extreme value for the non-stationary process $Z(t)$, which is a function of the system state \mathbf{z}_s . T is the duration of the response and $v(\zeta^+, t)$ the mean ζ -level up-crossing rate.

To obtain an expression for $v(\zeta^+, t)$, a new process $X(t) = z(t) - \mu_z(t)$ with zero mean and standard deviation $\sigma_X(t) = \sigma_z(t)$ is defined with an updated threshold for the new process, $\eta(t) = \zeta - |\mu_z(t)|$. In this case, the crossing rate becomes

$$v(\zeta^+, t) = v_X(\eta(t)^+, t) = \frac{\exp\left(\frac{-1}{2} \frac{\eta^2}{\sigma_X^2}\right)}{2\pi\sigma_X\sigma_{\dot{X}}\sqrt{1-\rho^2}} \left[\sigma_{\dot{X}}^2(1-\rho^2) \exp\left(-\frac{r^2}{2\sigma_X^2(1-\rho^2)}\right) + \sqrt{2\pi(1-\rho^2)}\sigma_{\dot{X}} \left\{ 1 - \Phi\left(\frac{r}{\sigma_X\sqrt{1-\rho^2}}\right) \right\} \left(\frac{\sigma_X\rho\eta}{\sigma_X} - \dot{\eta}\right) \right] \quad (54)$$

where σ_X and $\sigma_{\dot{X}}$ are the standard deviations of the processes X and \dot{X} , respectively, $\rho = \rho_{X(t)\dot{X}(t)} = \frac{cov(X(t)\dot{X}(t))}{\sigma_X\sigma_{\dot{X}}}$ is the time-dependent correlation coefficient, $r = \dot{\eta} - \frac{\sigma_{\dot{X}}\rho\eta}{\sigma_X}$ and $\Phi(\cdot)$ denotes the normal cumulative distribution function (CDF).

The values in Equation (54) are obtained from the EKF and UKF inference results. The outcome is the CDF of the exceedance probability of the maximum response at high thresholds. This enables probabilistic assessment of the risk of the structural response exceeding a given threshold over the duration of the excitation, including for small exceedance probabilities that would be infeasible to obtain using alternative sampling-based methods.

4.1.4 Application

The proposed method is applied to a shear-type building of 10 stories as shown in Figure (5-2) to demonstrate its use. This model is chosen to be consistent with Tien et al 2016 and facilitate comparison of the results with the linear case. For application to real-world problems, a condensed structural parameter matrix can be used based on predicted eigenvalues of degrees of freedom with uncertainties added to reflect modeling errors.

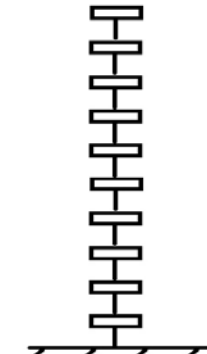


Figure 4-2 10-story shear-type structure

The robustness of the methodology to uncertainty in assumed parameters

is investigated later in the study. The stiffness for each story is assumed to follow the Bouc-Wen model, with the resistive force given as $F(t) = \alpha K_i u_s(t) + (1 - \alpha)DK_i\varphi(t)$. α is the ratio of final to initial stiffness K_i and $\varphi(t)$ is a hysteretic parameter given by $\dot{\varphi}(t) = A\dot{u}_s(t) - \beta|\dot{u}_s(t)||\varphi(t)|^{n-1}\varphi(t) - \gamma\dot{u}_s(t)|\varphi(t)|^n$.

For each story, the authors assume the mean values of mass m and stiffness parameter k_i to be unity and damping constant c to be 0.1 such that the coefficient of damping is 5% in the linear case. α , D , A , β , γ , and n are chosen to be 0.5, 1, 1, 0.5, -1.5, and 2, respectively as in Wen 1980. Initial results in the following section assume one known realization of values for the story parameters. To reflect the uncertainty in the ability to know the values of structural parameters exactly, these parameters are later randomized, distributing them with increasing coefficients of variation to investigate the performance of the methodology under increasing degrees of uncertainty.

The ambient noise and sensor measurement error are modeled as zero-mean Gaussian processes, with variances 0.5 m/s^2 and 0.25 m/s^2 , respectively, and assuming independence between sensors. One sensor is assumed to be placed on each story. The effect of varying the number, placement, and accuracy of the sensors on the estimation error is presented at the end of the results section. As previously described, the study uses a Bouc-wen model for the force nonlinearity. However, the results for a cubic or bilinear stiffness model have been found to be qualitatively consistent with the results presented in this study. Finally, it is noted that probabilistic inference on accelerations, velocities, and displacements at all stories can be obtained using the proposed methodology. The results shown are for the interstory drift between stories 4 and 5, called interstory drift #5, throughout this paper for consistency and to demonstrate the ability of the method to estimate interstory drift based on measured accelerations.

4.1.4.1 Modeling the Ground Excitation

To model the stochastic ground excitation, an earthquake is simulated as proposed in [14]. Acceleration at the bedrock w is modeled as a modulated, band-limited, normally distributed white

noise process with zero mean and time-varying variance. The time-dependent variance is treated as proportional to a gamma probability density function (PDF). A scaled gamma PDF is a reasonable representation of an earthquake as it is non-negative, starts at and tends to zero, and follows the shape of most earthquakes skewed with a longer right-side tail. The shape (k) and scale (θ) parameters for the gamma PDF are found based on the seismic variables as

$$k = \frac{t_{eq}^{max}}{\theta} + 1 \quad (55)$$

$$\theta = -\frac{1}{2}t_{eq}^{max} + \frac{1}{4}\sqrt{4t_{eq}^{max2} + D_{5-95}^2} \quad (56)$$

These parameters ensure that the mode of the PDF coincides with the time for the maximum intensity of the earthquake t_{eq}^{max} and the central 90% of the distribution corresponds with the total duration of the earthquake D_{5-95} , which is defined as the time between 5% and 95% Arias intensity values. A representative simulation of bedrock motion w is shown in Figure (5-3) with $t_{eq}^{max} = 20$ s, $D_{5-95} = 25$ s, and scaled by a factor of 70 with discretization time step = 0.01 s.

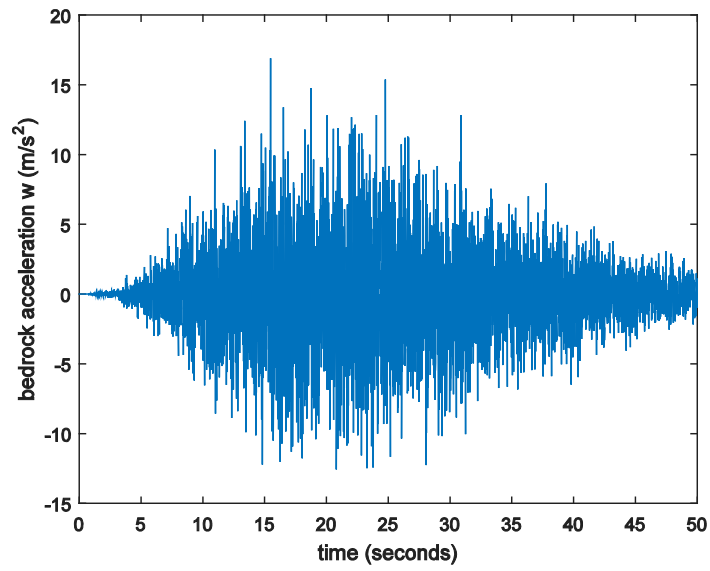


Figure 4-3 Sample bedrock excitation w vs. time, where w is normally distributed with time-dependent variance proportional to a gamma PDF

The parameters for the input motion are generally subject to high degrees of uncertainty. In the first part of this study, these values are assumed to be known at the site of interest. Later, the robustness of the proposed method to uncertainty in these input motion parameters is investigated and demonstrated. From the bedrock excitation w , the surface acceleration is calculated using ground filter parameters of $\frac{\omega_g}{2\pi} = 1.5$ and $\xi_g = 0.4$. The effect of uncertainty in ground parameter values is investigated as well.

The randomized earthquake is used to generate an observation matrix for the sensors placed on the structure. These observations are used to estimate the structural response under the excitation. At the same time, the simulation finds the actual response of the structure under the given ground motion. The estimated response using only the information from the sensor measurements is compared with the actual response to examine the accuracy of the method.

The process of investigation is as follows. The authors simulate the bedrock excitation, surface acceleration at the ground, and resulting structural response; this is called the actual response of the system. The structural responses are then used to simulate sensor observations, including measurement error. It is based on these observations that the study estimates the structural response using the DBN formulation and associated EKF and UKF. With the formulation described, the objective is to estimate system state \mathbf{z} , including displacement responses, based solely on the accelerometer measurements \mathbf{y} . The estimated results are compared with actual responses to assess the performance of the proposed methodology.

4.1.5 *Results*

The following results are presented: verification of the derived discretization solutions by comparing results using exact versus Taylor approximation methods; comparison of the estimation accuracies using EKF versus UKF; probabilistic inferences on the maximum response of the structure; robustness of the methodology to uncertainties in the structural, ground, and input motion parameters; and the effect of the number, placement, and accuracy of sensors on the ability to estimate the structural response.

4.1.5.1 Verification of Discretization Formulation

To verify the derivation of the discretization solution for nonlinear systems, the results obtained by the exact solution are compared to the Taylor approximation up to the second derivative term. The simulated ground motion is used as the direct input to compare the resulting responses. Figure (5-4) shows the results for the two discretization solutions for the interstory drift between stories 4 and 5. The figure shows a close correspondence between the exact and Taylor discretization solutions, including capturing of the peaks. Including more terms in the Taylor formulation will

decrease the error even further. However, it will increase the computational time and in some cases may not be feasible if the nonlinear function is non-differentiable. The approximate solution will also contain more error with increasing nonlinearity. The exact discretization formulation is therefore used in the remaining portions of this study.

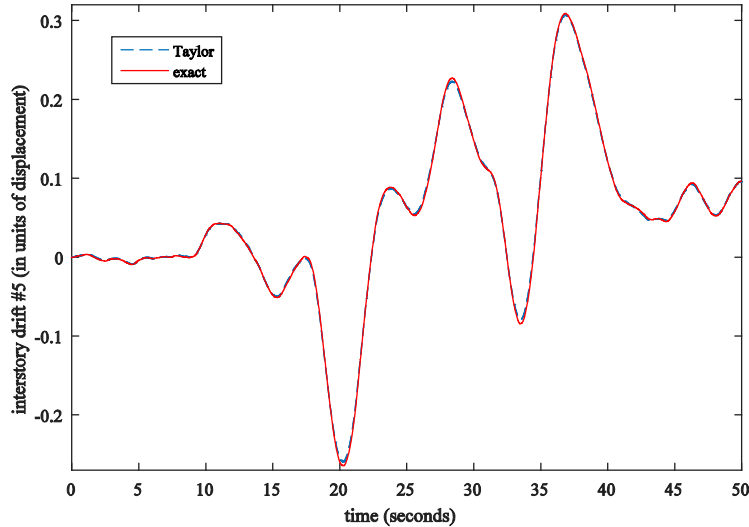


Figure 4-4 Interstory drift under input seismic motion for exact and Taylor expansion discretization solutions

4.1.5.2 EKF vs. UKF

Figure (5-5) shows the estimation results using UKF and EKF compared with the actual response from the simulation for the interstory drift between floors 4 and 5. To facilitate direct comparison between UKF and EKF, this analysis assumes data is available from accelerometers mounted at all 10 degrees of freedom. The results are shown more clearly in Figure (6), which focuses on the highest peak near 37 s to distinguish the plots. From Figure (5-6), using the UKF results in a smaller variance in the estimation compared to the EKF, with a narrower band in the UKF $\mu \pm 2\sigma$ estimates. Additionally, the UKF mean estimate corresponds more closely with the actual response. The total root mean square (RMS) error over the full time history with respect to the

actual simulation is 0.0073 (in units of displacement) for UKF compared to 0.0091 (in units of displacement) for EKF. Hence, UKF gives a more accurate estimation with lesser variance, and is the preferable framework for use in estimation for this application. Hereafter, estimation results presented are from the UKF.

It is noted that small deviations in the UKF estimates compared to the actual response can be seen in Figure (5-5) at the beginning of the time history. This is due to the assumption in the estimation of the variance of the displacement at the initial time step as 1 unit. However, as evident from Figure (5-5) and for the peak in Figure (5-6), the estimation variance as the excitation continues is on the order of 10^{-4} (in units of displacement-squared). Thus, while the UKF analysis fluctuates in the beginning of the time history, it quickly converges to the actual response. As the variance of the displacement would not be known beforehand, the initial assumption is not changed.

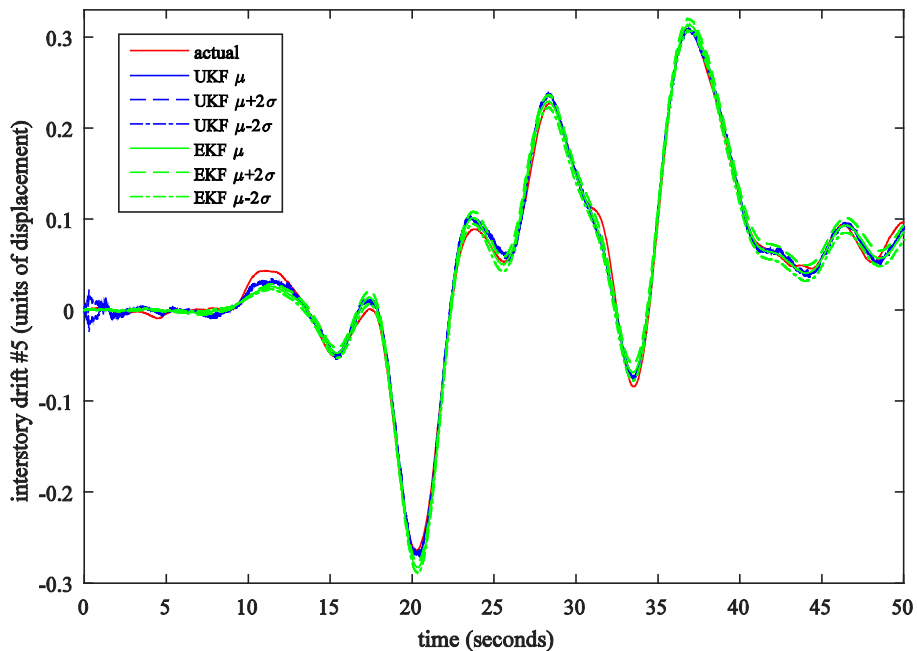


Figure 4-5 Estimated interstory drift #5 using EKF vs. UKF

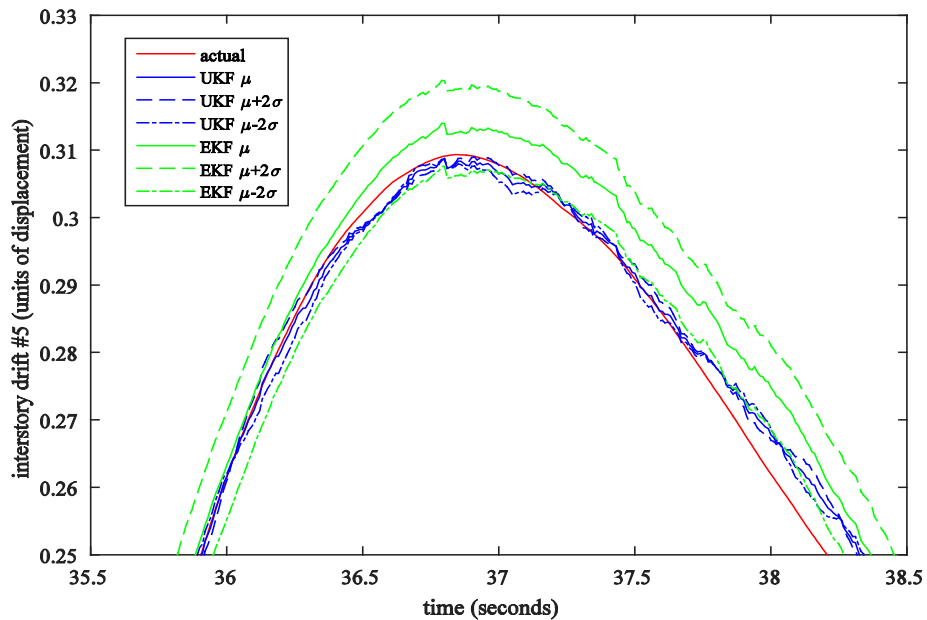


Figure 4-6 EKF and UKF estimates at the peak

4.1.5.3 Distribution of the Maximum Response

The ability to use the time history estimates as previously shown to perform probabilistic inference on the maximum response is now investigated. The results from the analytical formulation for probability of exceedance of the process above safe thresholds are compared with Monte Carlo (MC) simulations. 10,000 MC realizations are generated for the posterior process with randomly sampled priors. Figure (5-7) shows a close correspondence in the timing of the peak between the actual response, UKF estimation, and MC realizations. The magnitude of the peak is captured within 1.5% of the maximum response for the UKF estimate. Most of the MC realizations lie within two standard deviations on either side of the mean UKF estimate.

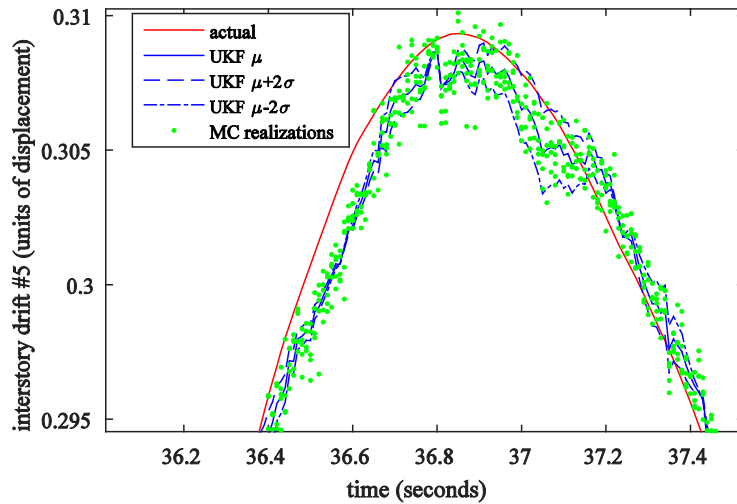


Figure 4-7 MC realizations of interstory drift #5 compared to actual and UKF response at the peak

Figure (5-8) shows the obtained stochastic distribution of the maximum response. It gives the complementary CDF of the maximum interstory drift of each story, i.e., the probability of the maximum response exceeding a threshold value of displacement. For each story, the analytical solutions, e.g., “id 1” for interstory drift at the first floor, are compared with MC realizations, e.g., “MC id 1”. The distribution for MC is the empirical complementary CDF obtained by counting the number of simulations where the absolute maxima exceeds a threshold out of the total 10,000 MC simulations.

In Figure (5-8), there is close correspondence between the analytical and MC results across the degrees of freedom. This shows the ability of the formulation to obtain stochastic distributions of the maximum response based on the sensor measurement data. The analytical solution plots, however, display some fluctuations at lower thresholds as can be seen in the plots for “id 1”, “id 2”, and “id 3” in Figure (5-8). This is in contrast to the expected monotonically decreasing complementary CDF. This is due to the assumption of Poisson crossings above the threshold of interest. At low thresholds, the assumption does not hold as, for example, clusters of crossings are

likely. Therefore, the analytical solution is suitable for use as a predictor at high thresholds and low probabilities of exceedance. These are the significant, high-impact events that are of interest, particularly when the structure is designed to withstand lower threshold displacements. The formulation presented enables risk analysis results for these extreme events, which may be infeasible to obtain using MC approaches.

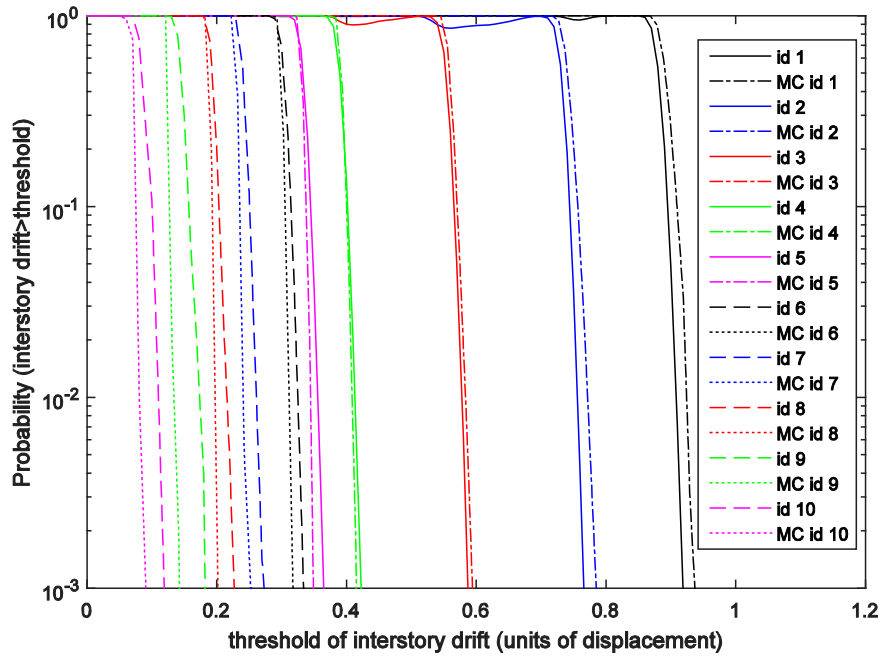


Figure 4-8 Analytical and MC distributions of maximum response with respect to various displacement thresholds

4.1.5.4 Robustness of Methodology to Uncertainty in Structural and Ground Parameters

The analyses up to this point have been based on the assumption that all system parameters are known. In general, these parameters are estimated and subject to varying degrees of uncertainty. Instead of the previously assumed single values for each parameter, in this section, they are randomized with increasing coefficients of variation. For structural parameters, damping is in general more difficult to estimate compared to mass and stiffness. Therefore, varying coefficients of variation (c.o.v.'s) of 0-20% from the nominal values for mass and stiffness and 0-40% for

damping are used. The values of these parameters are lognormally distributed at each level of c.o.v. Similarly, the ground parameters are also uncertain. The nominal values of ground parameters are set as assumed previously with $\frac{\omega_g}{2\pi} = 1.5$ and $\xi_g = 0.4$. These parameters are now varied by distributing them lognormally with c.o.v.'s ranging from 0-20%.

The combined effect of uncertainty in structural and ground parameters is analyzed. For consistency, the estimation result for the interstory drift between stories 4 and 5 is analyzed. Figure (5-9a) shows the RMS error of the estimated compared to the actual response with a point plotted for each value of c.o.v in increments of 1% (2% for damping). For Figure (5-9a), 20 samples are simulated for each c.o.v value and the mean and standard deviation of RMS error is calculated over all samples.

From Figure (5-9a), the mean RMS error remains nearly constant over the range of c.o.v.'s, while the standard deviation increases with increasing c.o.v.'s. Noting the ordinate scale, the maximum $\mu + 2\sigma$ value of RMS error is less than 5.5% of the maximum response, at 20% c.o.v. for mass, stiffness, ground parameters, and 40% c.o.v. for damping. Thus, the inference is robust to uncertainty in the structural and ground parameters even in the nonlinear case. This is because the UKF is able to use the information from sensor measurements to overcome the effect of the parameter uncertainty. It adapts to the discrepancies in the parameters through the changing observation matrix at each time step.

The variation of the estimate of the maximum structural response as a function of varying parameters is also of interest. Figure (5-9b) depicts the actual absolute maximum of the structural response with randomly distributed parameters compared to UKF estimates based on nominal

values of the parameters. C.o.v.'s are again increasing from 0-20% with c.o.v. of the damping coefficient being twice that of the other parameters.

From Figure (5-9b), the UKF-estimated mean maximum structural response stays within 0.003 units, or within less than 1%, of the actual maximum response even as c.o.v. increases from 0-20% for mass, stiffness, and ground parameters and 0-40% for damping. In addition, the variation of the estimate over 20 samples remains consistent with the variation of the actual response as c.o.v. increases. Results were similar in looking at structural and ground parameters separately. Thus, the estimate of the maximum is robust to uncertainty in the assumed parameters for the methodology.

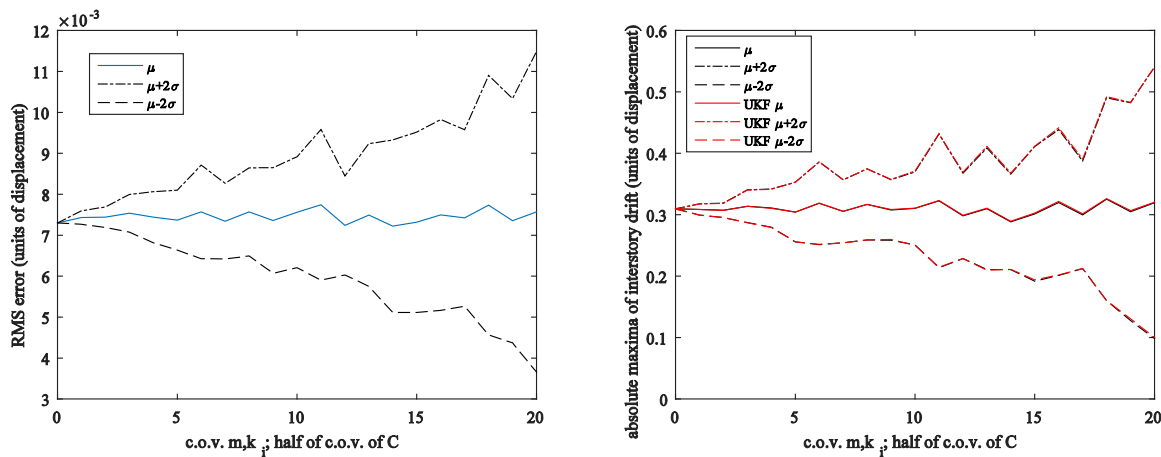


Figure 4-9 (a) RMS error and (b) maximum response as a function of increasing c.o.v.'s of structural and ground parameters

4.1.5.5 Robustness of Methodology to Uncertainty in Input Motion Parameters

The input motion parameters to describe an earthquake excitation are highly variable and generally unknown. The input motions are recorded and the parameters later investigated. However, this study uses a simulated ground motion and hence it is possible to analyze the robustness of the methodology to varying input motion parameters. It is noted that input motion uncertainty is

analyzed separately because while variations in structural and ground parameters reflect uncertainty in assumptions for the analysis, variations in input parameters reflect performance of the methodology under different earthquake events.

In the stochastic ground motion model, two parameters are used to define the earthquake: time of maximum intensity t_{eq}^{max} and effective duration of the earthquake between 5% and 95% of the Arias intensity values D_{5-95} . Here, these parameters are varied normally with c.o.v.'s ranging between 0-20% to reflect variability across earthquake motions. Figure (5-10a) shows the performance of the method for c.o.v.'s varying in increments of 1%, with the RMS error again calculated as the mean of 20 simulations at every value of c.o.v.

From Figure (5-10a), the RMS error with varying input parameters remains nearly constant for all simulations, both in terms of the mean and standard deviation. This is because the evolution of the system per the UKF formulation in Equation (51) depends only on the structural and ground parameters, without input parameters.

Figure (5-10b) shows the behavior of the maximum response with increasing variation in input motion parameters. In all cases, the estimated response, both in terms of mean and standard deviation, follows closely the actual maximum response. This demonstrates the estimation methodology to be robust to uncertainty in the input motion.

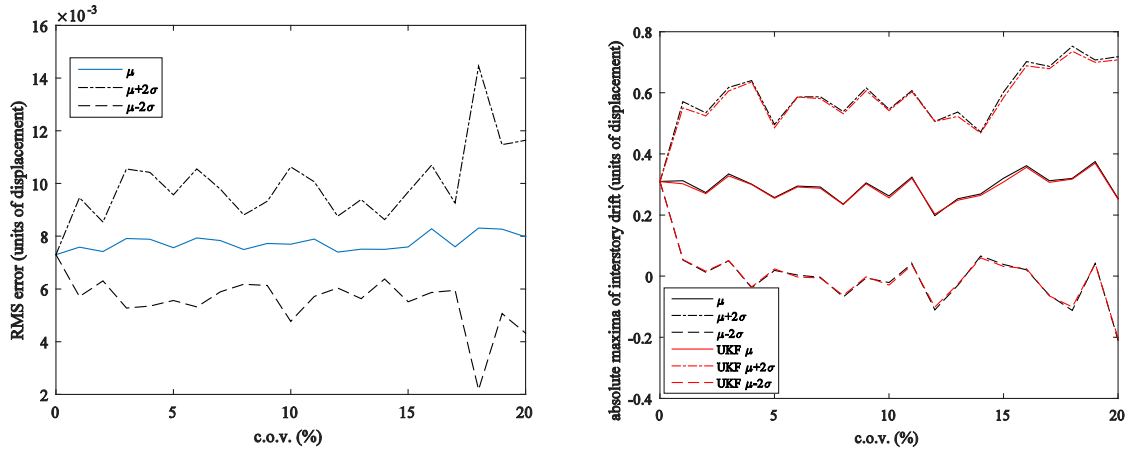


Figure 4-10 (a) RMS error and (b) estimated maximum response as a function of increasing c.o.v.'s of input motion parameters

4.1.5.6 Varying Measurement Characteristics

Finally, the effect of the number, placement positions, and measurement errors of the sensors is investigated. Figure (5-11) shows RMS error results for three different sensor configurations. First, when one sensor is placed at the bottom floor; second, when one sensor is placed at the top floor; and third, when four sensors are placed throughout the structure on floors 1, 4, 7, and 10. The sensor measurement error is also varied as 0.5, 1, and 2 m/s^2 . From Figure (5-11), as expected, the RMS error is the lowest when more sensors are used because more information is available on which to condition the estimation. The RMS error is the highest when only one sensor is placed at the bottom floor because this captures the smallest response, thereby providing the least amount of information. Consistent with previous results in Tien et al 2013 and Tien et al 2016, when only one sensor is placed on the structure, it is advantageous to mount it on the top floor compared to the bottom floor.

Looking at sensor noise, as expected, the error in the estimates increases with increasing uncertainty in the sensor measurements. From Figure (5-11), a tradeoff between the number of

sensors and the measurement error is observed. For comparable estimation accuracy, more sensors should be used if the sensor measurement error is higher, but with better precision sensors, fewer sensors can be used. The difference between placing a sensor at the top compared to the bottom of the structure, however, is most significant. These results can be applied to structural health monitoring systems, in designing effective instrumentation configurations to best support the estimation of structural response.

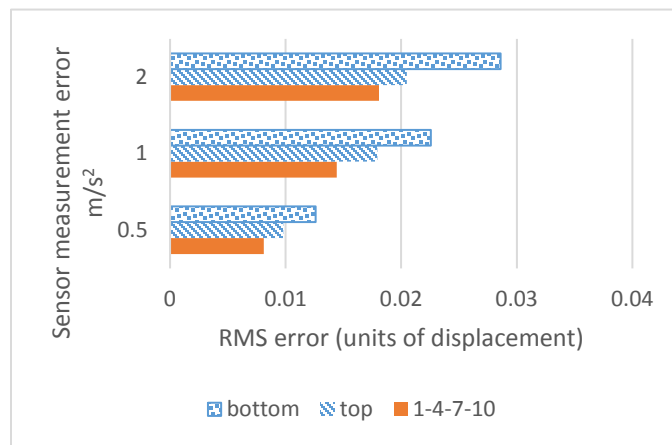


Figure 4-11 RMS errors for varying sensor configurations in terms of number, placement, and precision

4.2 Experimental study

4.2.1 Introduction

The proposed approach in the previous section, which leverages the accelerometer monitoring data to estimate the structural response, is evaluated by comparing estimated responses with experimentally measured test data under different excitations. Data is collected from an instrumented two-story structure in the laboratory. Both random excitations and ground motions from historic earthquakes are used in the analysis. The objective is to evaluate the accuracy of

using sparsely instrumented building accelerometer data to estimate and structural displacement responses. As multiple sources of uncertainty are present in the problem, performance of the methods under uncertainty in the structural parameters and ground motions is also assessed. The resulting experimental verification of the approaches, including under uncertainty, is an important first step to move from numerical simulation results towards implementation of monitoring systems on a real structure. The structure for experimental verification does not have any material nonlinearity.

4.2.2 Experimental setup

The experimental verification results presented in this study are for both the estimation and prediction of the structural response under dynamic loadings. The methodology to predict the structural response is presented in the next chapter. First, the accuracy of the real-time estimation of the response based on the building accelerometer data is assessed. Second, the ability to predict the structural response based on a limited amount of initially collected data is evaluated. The same experimental setup and instrumentation is used for verification of both the estimation and prediction approaches. The lab-scale experimental setup is shown in Figure (5-12). The two-story steel structure has spring steel columns and a steel plate at each story. The story heights for each story are 0.520m and 0.555m, respectively; the corresponding mass for each story is 15.4 kg and 14 kg, respectively. The structure is instrumented with three accelerometers, a string pot, and two LVDTs. The accelerometers are mounted at the table and both of the stories. Accelerometer acc1 measures the input table acceleration, the accelerometer mounted at the first story acc2 measures the first story acceleration, and the last accelerometer mounted on the second story acc3 measures the second story acceleration. A string pot is placed at the table to measure the table displacement

relative to a fixed reference under the excitation, while LVDT1 and LVDT2 measure the first and second interstory displacements, respectively.

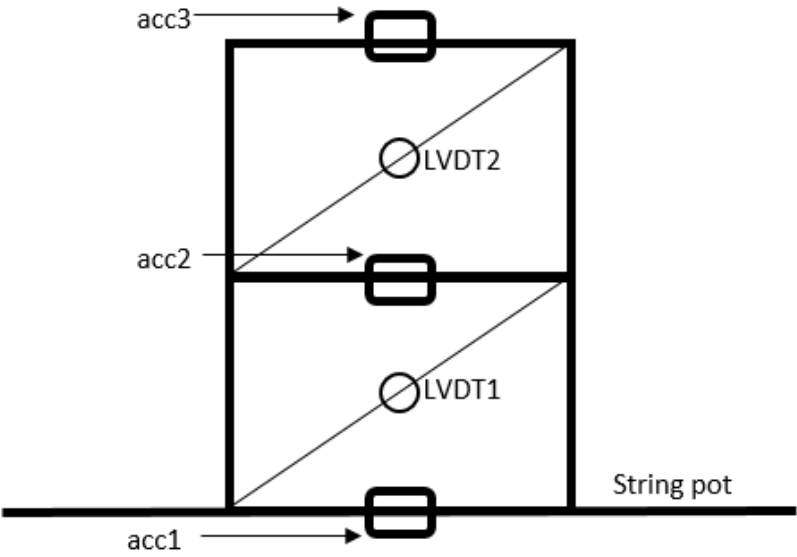


Figure 4-12 Experimental setup for the instrumented structure



Figure 4-13 Experimental test setup in the laboratory

Figure (5-13) shows the experimental setup with the image of the structural specimen used. The structure is analyzed as a lumped mass system at the two degrees of freedom. The sampling frequency for the accelerometers is 100Hz. The displacement is measured in inches and the acceleration is measured in the units of g . The natural frequencies of the structure are $f_1 = 0.75\text{Hz}$ and $f_2 = 1.75\text{Hz}$. The two damping ratios are $\zeta_1 = 3\%$ and $\zeta_2 = 5\%$. The LVDT range is ± 0.5 in.

The discretization methodology can be reformulated in terms of natural frequency and damping ratio. The state space matrices and vectors become

$$\mathbf{A}_1 = \begin{bmatrix} \mathbf{I} & \mathbf{I}\Delta t \\ \mathbf{0} & e^{-2\omega\zeta\Delta t} \end{bmatrix} \quad (1)$$

$$\mathbf{F}_1 = \begin{bmatrix} \mathbf{0} \\ -\omega^2(e^{-2\omega\zeta\Delta t} - \mathbf{I})(-2\omega\zeta)^{-1} \end{bmatrix} \mathbf{z}_k \quad (2)$$

$$\mathbf{b} = \mathbf{b}_c(2\omega\zeta)(e^{-2\omega\zeta\Delta t} - \mathbf{I}) \quad (3)$$

4.2.3 Evaluation

Experimental verification of the estimation and prediction approaches is performed by comparing the analytical, estimated, and observed response histories for each dynamic excitation. Results presented are for the interstory displacement between the first and second stories. Any other response of interest, including accelerations, velocities, and displacements at any degree of freedom can be similarly compared. The analytical response is calculated based on the known input acceleration using the discretization equation. The estimated response is calculated based on the data collected from the accelerometer mounted on the second story of the structure without any knowledge of the input excitation. The observed response is the response as experimentally

measured by the LVDTs. All three responses are shown for the first ground motion. Because the analytical and estimated results are close, only the estimated and experimentally observed responses are compared for the other excitations.

Accuracy of the methods are evaluated based on the root mean square error (RMSE) over the full time-history and based on the percentage error of the maximum response. RMSE is calculated as

$$\text{RMSE} = \sqrt{\left(\sum_1^N (Y_{oi} - Y_{ei})^2 / N\right)} \quad (4)$$

where Y_{oi} is the observed displacement at time step i and Y_{ei} is the estimated displacement at the same time step. N is the total number of time steps. The RMSE is also scaled by the maximum response d_{max} , giving a percentage error with respect to the absolute value of the maximum interstory displacement response as $\text{error}(\%) = \frac{\text{RMSE}}{|d_{max}|} \cdot 100$, referred to in this manuscript as the scaled error. Finally, the percentage error in the estimation of the maximum response is calculated as $\text{error}(\%) = \frac{|Estimated\ d_{max} - Observed\ d_{max}|}{Observed\ d_{max}} \cdot 100$. The RMSE provides a global measure of the accuracy of the estimation over the full time-history while the error in the maximum provides a localized measure of accuracy at the peak response of interest.

4.2.4 Results

A series of earthquake and random input excitations are run to assess the accuracy of the approach to estimate the structural displacement response based solely on the building accelerometer measurement data. The resulting estimated interstory displacement is compared to the experimentally observed LVDT measurements to evaluate performance across loadings of varying characteristics, including magnitudes and frequency content.

Figure (5-14) shows the comparison of the analytical, estimated, and observed interstory displacement between the first and second stories for an input excitation of the El Centro earthquake scaled to 10% of the actual ground excitation. The results show the three response histories to overlap closely. Figure (5-15) zooms in on the peaks of the responses to see their variations more clearly. From Figures (5-14) and (5-15), the estimated response is close to the actual observed response over the entire time history, including at the peaks. The analytical results confirm the discretization formulation and the comparison between the estimated and observed responses verifies the estimation approach. The RMSE over the full time-history between the estimated and observed responses is 0.0075in. The scaled error is 2.41% of the maximum response. It is noted that the scaled error in this case is amplified because the maximum response is small. The maximum response itself, which is generally of the greatest importance in reliability studies as a governing parameter of performance, is estimated accurately, with an error between the estimated and observed maximum responses of 4.79%.

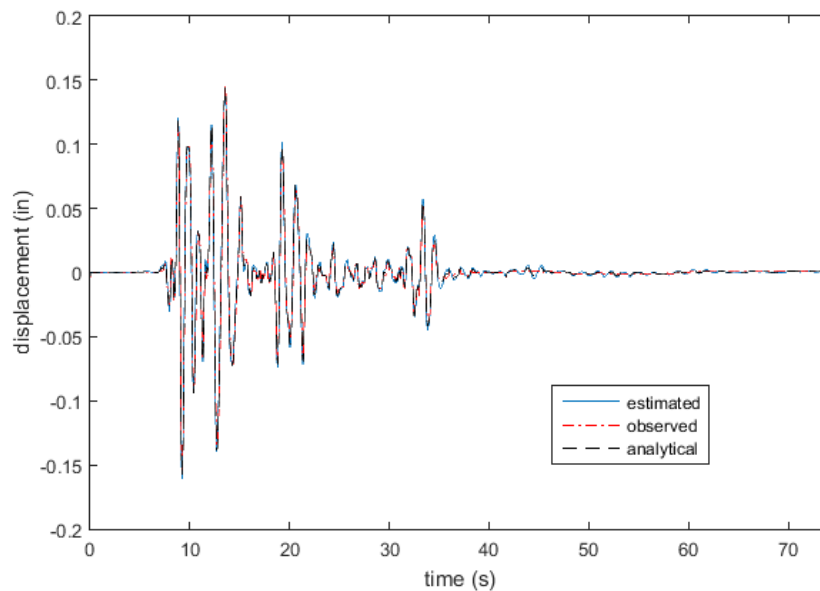


Figure 4-14 Comparison of analytical, estimated, and observed interstory displacement for El Centro earthquake

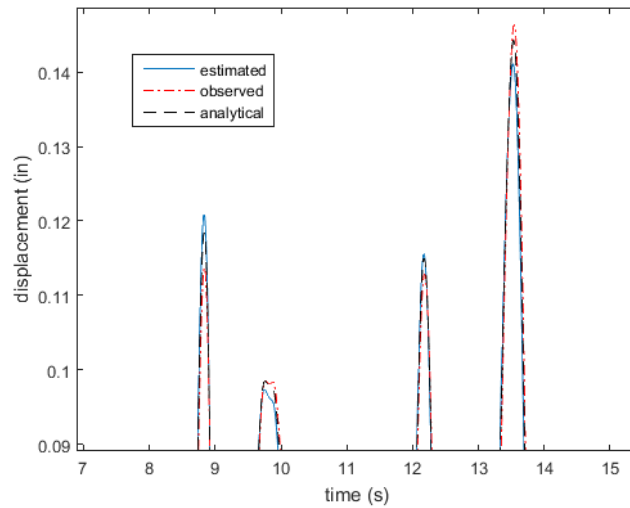


Figure 4-15 Comparison of responses for El Centro earthquake zoomed at the peaks

Figure (5-16) shows the comparison of the estimated and observed interstory displacement for a realization of the Kobe earthquake scaled to 5% of the actual ground acceleration. The results are presented for different earthquakes as the character and parameters for different earthquakes are quite different. As the method can theoretically have uncertainty at every time step from multiple sources, it is important to analyze the performance of the method against different characters of earthquake excitations. For clarity, only the estimated and observed responses are compared for all the cases from here onwards. For the estimation shown in Figure (5-16), the RMSE is 0.0083in. Figure (5-17) shows the comparison of the estimated and observed responses at the peaks for the scaled Kobe earthquake excitation. The estimated response history is similar to the experimentally observed response, including a close estimate of the peak response. The scaled error is 1.78%, which is lower than the previous El Centro case because of the larger magnitude of the maximum response, and the error in the estimation of the maximum response is 6.89%. This error is higher for Kobe than other earthquakes because the ground motion history has a sudden impulse in the beginning and the UKF takes time to stabilize over the time history.

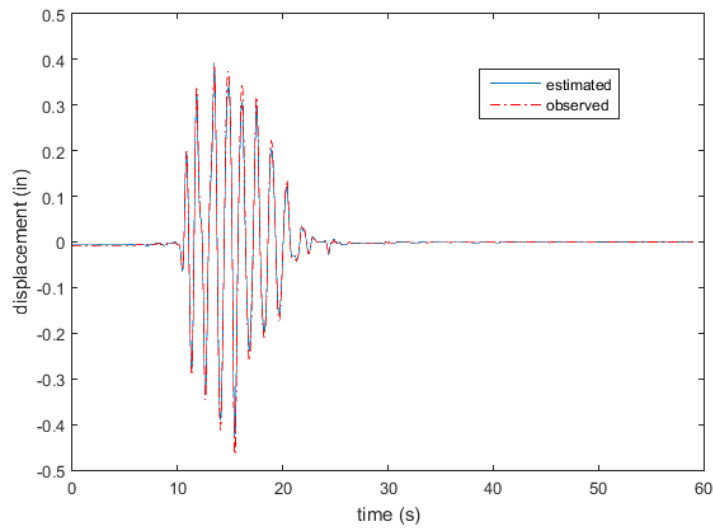


Figure 4-16 Comparison of estimated and observed response for Kobe earthquake

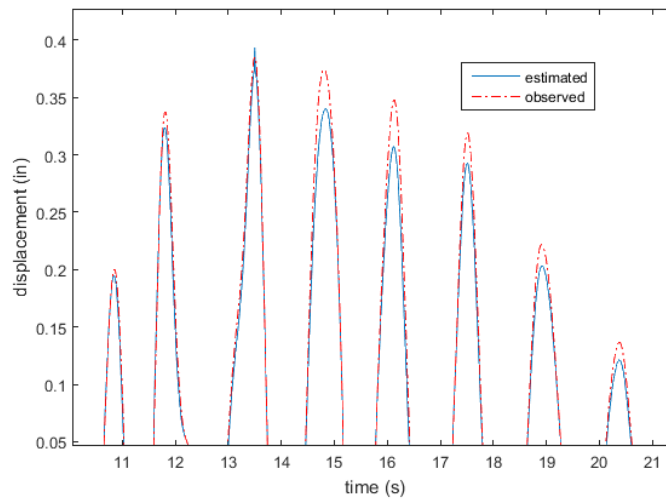


Figure 4-17 Comparison of responses for Kobe earthquake zoomed at the peaks

Figure (5-18) is the comparison of the estimated and observed response for a realization of the Miyagi earthquake scaled to 6% of the actual ground acceleration. For this record, the methodology provides accurate results across the full time history and for the maximum response in particular. The RMSE for this case is 0.0035in with a total error of 0.92%, and the error in the estimation of the maximum response is 2.45%. Figure (5-19) shows the comparison of the

responses when zoomed in at the peaks. The responses are consistently overlapping across the time history and at the peaks.

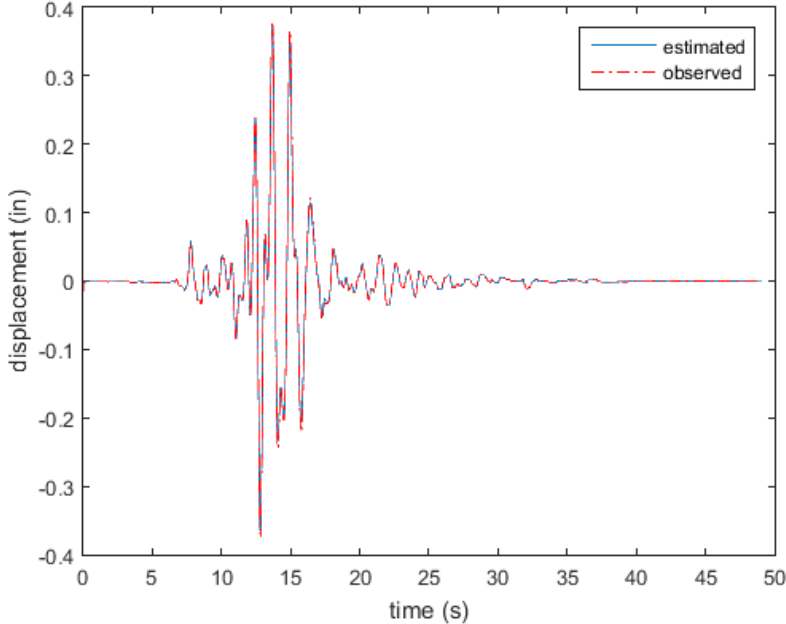


Figure 4-18 Comparison of estimated and observed response for Miyagi earthquake

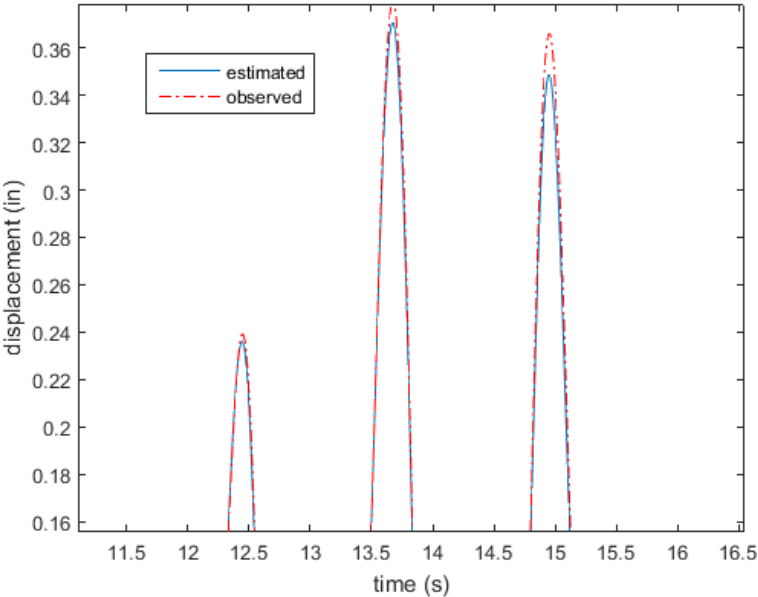


Figure 4-19 Comparison of responses for Miyagi earthquake zoomed at the peaks

Figures (5-20) and (5-21) show a comparison of the estimated and observed response for a realization of Chi-Chi earthquake scaled at 10% of the actual ground acceleration, over the entire time-history and at the peaks, respectively. The RMSE for this case is 0.0083in and the total error is 2.48%. The error in the estimation of maximum response is 3.32%. Figure (5-21) shows the differences between estimated and observed responses at local peaks. The differences are small and consistent with the quantified error.

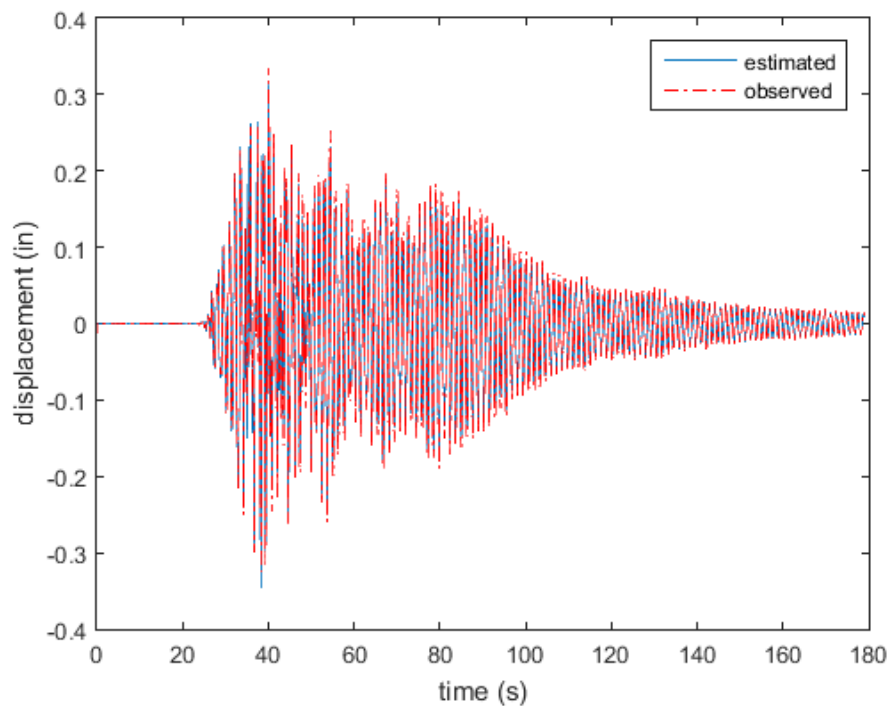


Figure 4-20 Comparison of estimated and observed response for Chi-Chi earthquake scaled at 10%

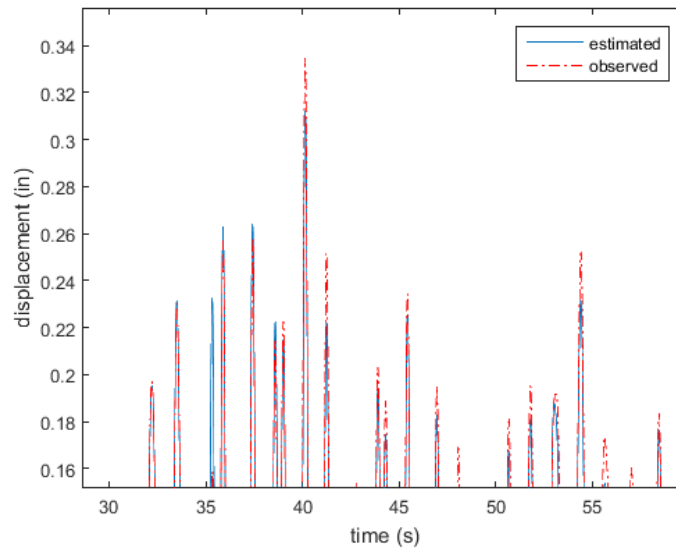


Figure 4-21 Comparison of responses for Chi-Chi earthquake at 10% scaling, zoomed at the peaks

In addition to the seismic response, we investigate the performance of the estimation methodology for a band-limited white noise excitation. The excitation is banded between 0.5 and 3 Hz to excite the first and second mode of the system. Figure (5-22) shows the comparison of the estimated and observed interstory displacement for the random input excitation over a time period of 150 seconds. Compared to the earthquake loadings, the excitation results in more localized peaks and sustained periods of higher magnitude responses. The RMSE over the full time history is 0.0104in and the total error is 2.88%. The multiple local peaks are well matched by the estimated response. The error in the estimation of maximum response is 1.62%. Figure (5-23) shows the comparison of the responses when zoomed in at the peaks. The responses are similar with small errors. The total error in this case is slightly higher than for the other earthquake loading cases because the random input is a band-limited white noise process without structure for the UKF to capture.

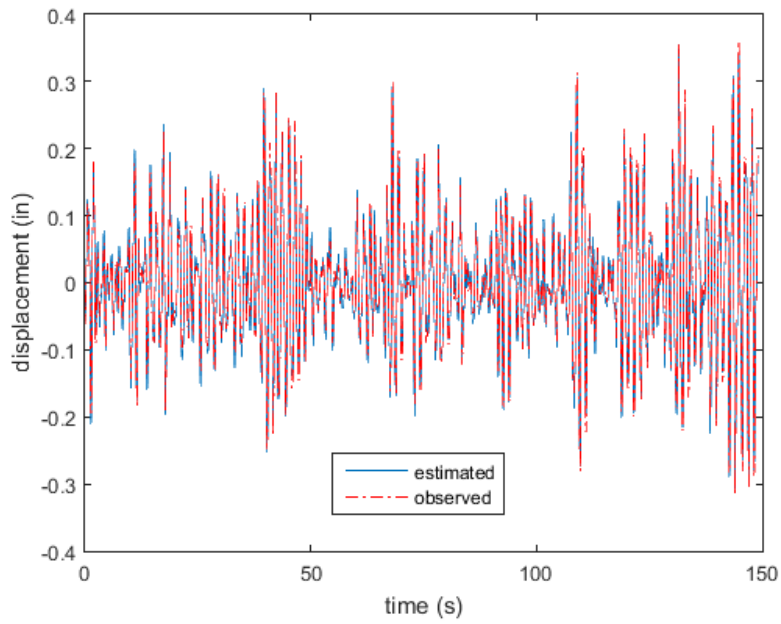


Figure 4-22 Comparison of estimated and observed response for a random input excitation

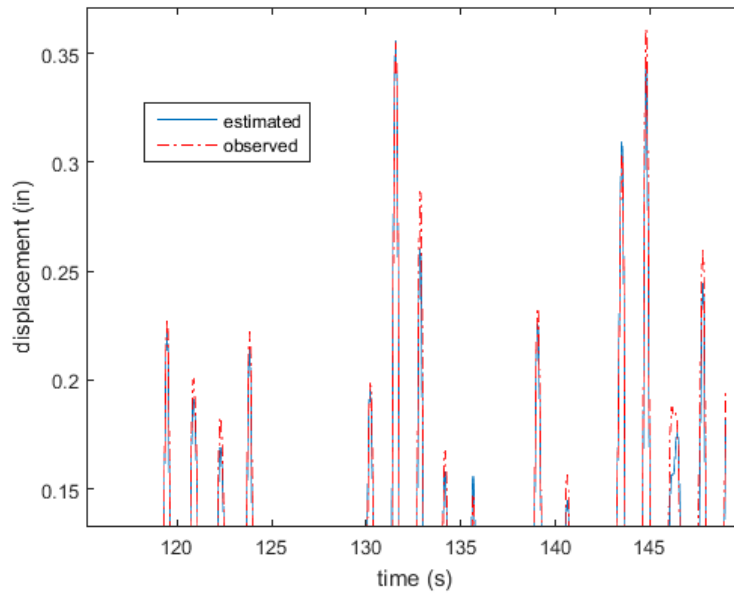


Figure 4-23 Comparison of responses for a random excitation zoomed at the peaks

4.2.4.1 Estimation under uncertainty

In any structural response estimation, the values of the structural parameters used influence the outcomes of the estimation. In practice, these parameters are estimated, for example, based on original structural designs. To assess the impact of uncertainty in these estimated parameters on the performance of the methodology compared to experimental results, the parameter values used in the response estimation are systematically varied. Figure (5-24) shows the error in the response between the estimated and experimentally observed values as the uncertainty in the frequencies and damping ratios increase. The error is calculated based on the RMSE as a percentage of the maximum response for the nominal case. The randomized structural parameters are taken to be normally distributed with the nominal values of the parameters assumed to be the means and with varying coefficients of variation (c.o.v.'s). The c.o.v. of the frequencies vary from 0 to 20% and the damping ratios from 0 to 40% to reflect the typically larger uncertainty in estimating damping. The uncertainty analysis is performed for the Chi-Chi ground motion input with 100 simulations run for each c.o.v. In Figure (5-24), the mean and standard deviation of the error are shown. While the mean and standard deviation in the error of the estimate increase with increasing c.o.v., as expected, the error increases to at most 4.73% for c.o.v. up to 20% for frequency and 40% for damping, representing high uncertainties in the structural parameters. The results show the estimation methodology to be robust to uncertainty in the structural parameters.

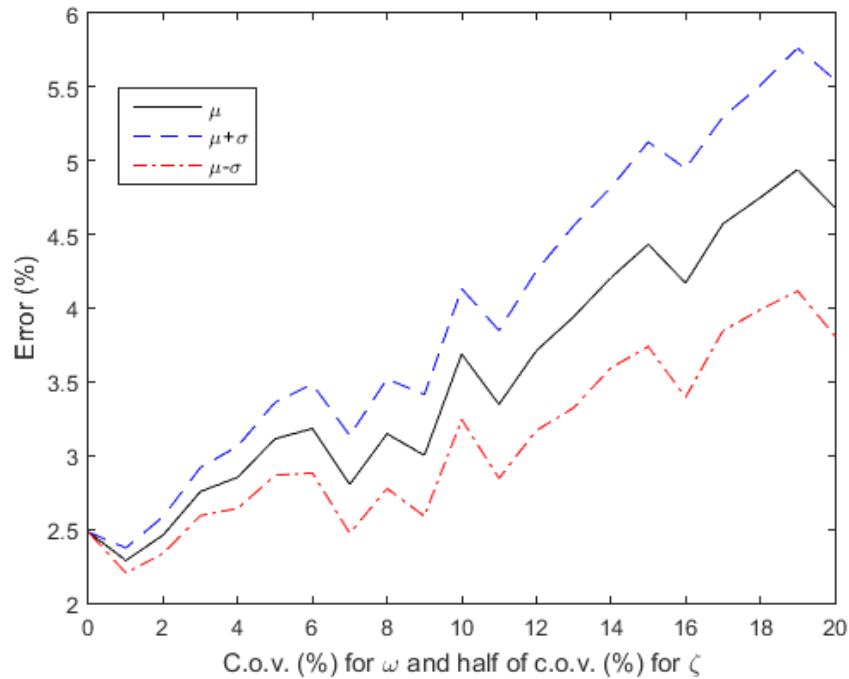


Figure 4-24 RMS Error in response estimate with increasing c.o.v. for structural parameters

To assess the impact of uncertainty in the structural parameters on the uncertainty of the maximum response estimation, Figure (5-25) shows the distribution of the estimated maximum interstory displacement response for increasing values of the c.o.v. As the c.o.v. increases, the standard deviation of the estimate increases; however, the magnitude of the increase is small. The mean estimate of the maximum structural response remains consistent even for high uncertainties in the structural parameters, with a mean value close to the actual maximum response. The results show that the methodology is robust even for high uncertainties in the structural parameters to estimate the maximum response as the variance in the prediction is low and the expected value of prediction is close to the measured value under high uncertainty cases.

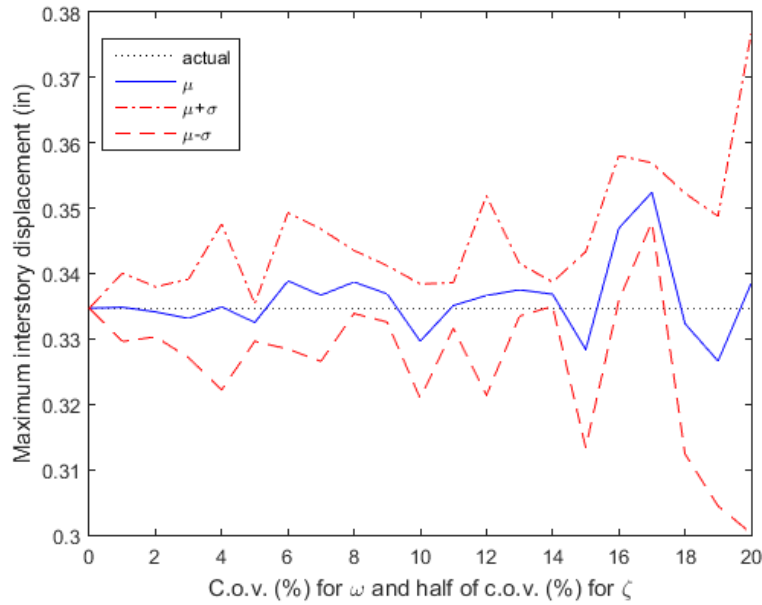


Figure 4-25 Maximum response estimate with increasing c.o.v. for structural parameters

4.3 Conclusion

The proposed methodology uses the Kalman-estimated system state to assess the nonlinear response of a structure under seismic load based on observations from accelerometers placed on the structure. The methodology includes an exact discretization solution derived for the nonlinear system and validated against a Taylor expansion-based discretization method. The estimation results show the UKF to provide the most accurate estimations of structural response, particularly at the peak. The methodology provides a probabilistic assessment of the distribution of the maximum response in particular, with the analytical results verified through comparison with MC simulations. Through analyses of the impact of variations in the system parameters on the results, the methodology is shown to be robust to inaccurate or uncertain assumptions for the structural and ground parameters, as well as across input motions. Additionally, inferences drawn support

decision making in structural health monitoring applications, including in the number, placement and accuracy of sensors required to assess structural response. The probabilistic formulation presented enables estimation of the stochastic distribution of the maximum nonlinear response, under conditions of uncertainty for the system, excitation, and measurement parameters.

The results of this study are experimentally verified using building accelerometer data. The observed response histories measured from the experimental tests are compared with the estimated responses for a number of input excitations, including scaled El Centro, Kobe, Miyagi, and Chi-Chi earthquake ground motions. The error in the estimation is quantified in terms of RMSE over the full time-history, with the estimation methodology achieving between 1% and 3% error relative to the maximum response using only the accelerometer measurement data without knowledge of the excitation. In terms of estimating the maximum response, of interest in many structural reliability calculations, the methodology is accurate within 3% to 7% of the experimentally observed maximum interstory displacement. The error is even lower for the random input excitation. The proposed estimation methodology works in real time and uses only the data from building-mounted accelerometers to provide an estimation for the structural response. Increasing uncertainty in the estimated values of the structural parameters, the method estimates the response with at most 4.73% error for coefficients of variation up to 20% for frequency and 40% for damping. The results show that the methodology can be used in real time to robustly estimate the structural response even under conditions of uncertainty.

CHAPTER 5. NEAR-TERM RELIABILITY: REAL TIME PREDICTION OF STRUCTURAL SEISMIC RISK AND A STRUCTURE-SPECIFIC EARTHQUAKE EARLY WARNING SYSTEM

5.1 Theoretical study

5.1.1 Introduction

Earthquakes are among the most significant natural hazards we face, causing an average of \$12 billion in economic damages and nearly 13,000 deaths annually across the globe [number]. The risk from any natural hazard depends on the occurrence and extent of the hazard, vulnerability of the infrastructure, and consequential effects on the population. With aging infrastructure, growing populations in earthquake-prone areas, and an increasing number of earthquakes including due to human activities such as fracking and saltwater disposal, global seismic risk is increasing. Effective earthquake early warning systems would enable protective measures to be taken and vulnerable populations to seek safety before the full extent of a seismic event occurs.

The complexity in the nucleation and growth of an earthquake, however, makes it difficult to accurately predict seismic events. Recently, several early warning systems have been developed, which use real-time seismology to issue an earthquake warning. These systems rely on the real-time recording and processing of earthquake data. Such models predict the extent of a regional earthquake threat based on the content of the seismic wave within the initial few seconds of a recorded event. We propose an early warning system that goes beyond ground motion prediction to consider the response of the structure itself. The objective is to create a methodology that provides an earthquake early warning based on the anticipated structural response, which is

predicted from information from sparsely instrumented buildings rather than relying on extensive seismological data. The proposed localized and structure-specific approach uses collected data to run simulations and create a suite of synthetic accelerograms. These accelerograms are then used to estimate structural responses, with warnings based on predicted maximum responses.

Specifically, the methodology first takes the data from an accelerometer placed on the structure and separates the ground motion and structural response in real time. The initial 3 seconds of p-wave data is used to estimate the characteristics of the earthquake, including moment magnitude, Arias intensity, and hypocentral distance from the structure. A number of ground motions are then simulated based on these parameters. From these, we find the structural response for each simulated ground motion and infer the maximum structural response due to the upcoming earthquake. The future structural response is predicted as the average of the responses to the set of predictive simulated ground motions. The proposed method does not require extensive knowledge of the regional seismic history, local ground characteristics, or information from additional seismograph stations. It is a minimalist approach, which can, however, be made more accurate if conditioned on additional known seismological information at the site under consideration.

The rest of the study is organized as follows: next section provides background on previous work on seismic risk and earthquake early warning systems, followed by a section that describes the proposed methodology, including separation of the ground motion and structural response, early prediction of earthquake parameters, and simulation of ground motions. The results of the methodology are presented later, with the distribution of predicted maximum responses and root mean square errors of the predictions presented for an example earthquake. Computational efficiency of the methodology is investigated, as well as robustness of the method to uncertainty in assumed system parameters. The methodology is applied to several earthquakes to investigate

the generalizability of the methodology across earthquake events. Finally, the method is investigated using experimental data based on the experimental setup from the previous chapter.

5.1.2 Background

Most of the previous work on structural seismic risk has focused on assessing risk to a building or region before or after an event has occurred. Pre-event analyses include recent work in response estimation and building portfolio reliability assessment to compute seismic loss probabilities [46-47]. Other work includes quantifying uncertainty in seismic risk assessment [48] and risk assessment for particular structures, such as reinforced-concrete frames [49-50], seismically isolated structures [51], and bridges [52]. Post-event analyses focus on damage mapping [53] and assessment [54] after the earthquake has occurred. In contrast to these studies, the methodology proposed here is for real-time prediction of seismic risk given the occurring ground motion. This is related to previous work in earthquake early warning with a focus on structural response in particular.

The development of earthquake early warning systems using real-time seismology dates back to Nakamura's introduction to the concept of using frequency content of p-waves for inferences on the characteristics of an earthquake [6]. The frequency content in the initial few seconds of the p-wave can be analyzed either as the time period of a monochromatic wave (τ_c) or as the maximum time period (τ_p^{max}). Kanamori [7] extended Nakamura's work to use in practical real-time seismology. Studies by Wu and Kanamori [8-11] show a strong correlation between τ_c and moment magnitude M_w . They developed an early warning system based on the initial 3 seconds of the p-wave by observing τ_c and the maximum ground displacement P_d . Through the τ_c - P_d method, P_d was found to have a good correlation with the peak ground velocity (PGV) of the

approaching earthquake. Allen and Kanamori [12] and Olson and Allen [13] used τ_p^{max} to develop a similar methodology. Through the $\tau_p^{max}-P_d$ method, their work shows a strong relationship between τ_p^{max} and M_w .

Wurman, Allen, and Lombard [55]; Allen [56]; and Allen et al. [57] proposed ElarmS, which uses a network-based approach. It extends the single station approach from previous studies to a network of stations, where the data from the entire network is processed simultaneously to issue a regional warning. Cua and Heaton [58] developed virtual seismologist (VS), using a Bayesian approach to predict the most probable magnitude and location of an earthquake given observations through conditioning on historical data. An extensive data history is required for the prior distributions and conditioning. Wu, Kanamori, Allen, and Hauksson, [59]; and Shieh, Wu, and Allen [60] found relationships between the initial ground motion parameters and earthquake characteristics, with these methods subsequently used for earthquake warning applications in Böse et al [61-62] and Cheng, Wu, Heaton, and Beck [63].

All of the described earthquake early warning systems predict the extent of an upcoming earthquake for a region. These methods do not account for the behavior of individual structures. Assessing the seismic risk for a particular building requires a combined analysis of the ground motion and structural behavior. Therefore, we move beyond regional earthquake warnings to create a structure-specific and localized earthquake early warning system. This study investigates our proposal that from the first 3 seconds of structural sensor data, we can obtain predictive characteristics of the earthquake. If we then simulate a number of ground motions, then the average structural response will conform to the actual response of the structure under the approaching earthquake, enabling an early warning to be issued.

5.1.3.2 Separation of ground motion and structural response

In this study, we assume a minimally instrumented building using low-cost accelerometers. The first step of the process is to use the data from the accelerometers placed on the structure to obtain the ground motion signal. If the accelerometer is placed on the ground at the structure, then it captures the ground motion directly, but if the same sensor is placed on any other part of the structure, then it records the sum of the ground motion and the structural response. Therefore, we need to separate these two elements from the accelerometer measurements [64]. To do this, the unscented Kalman filter (UKF) is used as in [65]. In addition, the sensor recordings contain ambient noise. As shown in [1], the error in the estimate due to ambient noise reduces significantly if the sensor is placed on the higher stories of a structure. Hence, if a structure is instrumented with a single accelerometer, as is assumed in this study, we recommend that the sensor be placed on the top story of the building for these applications.

To separate the ground motion from the structural response, we begin with the equation of motion for a structure subjected to ground acceleration

$$\mathbf{M}\ddot{\mathbf{u}}_s + \mathbf{C}\dot{\mathbf{u}}_s + \mathbf{F}(\mathbf{u}_s) = -\mathbf{M}\mathbf{1}a_g \quad (1)$$

where \mathbf{M} , \mathbf{C} and \mathbf{F} represent the mass, damping and spring force matrices, respectively. \mathbf{u}_s represents displacement of the structure and a_g acceleration of the ground. Defining $\mathbf{z}^T := [\mathbf{u}_s^T \quad \dot{\mathbf{u}}_s^T]$ in first-order form, the equation of motion is

$$\dot{\mathbf{z}} = \begin{bmatrix} \mathbf{0} & \mathbf{I} \\ \mathbf{0} & -\mathbf{M}^{-1}\mathbf{C} \end{bmatrix} \mathbf{z} + \begin{bmatrix} \mathbf{0} \\ -\mathbf{M}^{-1}\mathbf{F}(\mathbf{z}) \end{bmatrix} + \begin{bmatrix} \mathbf{0} \\ -\mathbf{1} \end{bmatrix} a_g \quad (2)$$

$$\dot{\mathbf{z}} = \mathbf{A}_c(\mathbf{z})\mathbf{z} + \mathbf{b}_c a_g \quad (3)$$

We discretize Equation (2) as in [65] to obtain the evolution of the system from time step k to $k + 1$

$$\mathbf{z}_{k+1} = \mathbf{A}_1 \mathbf{z}_k + \mathbf{F}_1 + \mathbf{b} a_g \quad (4)$$

where

$$\mathbf{A}_1 = \begin{bmatrix} \mathbf{I} & \mathbf{I} \Delta t \\ \mathbf{0} & e^{-\mathbf{M}^{-1} \mathbf{C} \Delta t} - \mathbf{1} + \mathbf{I} \end{bmatrix}$$

$$\mathbf{F}_1 = \begin{bmatrix} \mathbf{0} \\ -\frac{\mathbf{M}^{-1} \mathbf{F}(\mathbf{z}_s)(e^{-\mathbf{M}^{-1} \mathbf{C} \Delta t} - \mathbf{I})}{-\mathbf{M}^{-1} \mathbf{C}} \end{bmatrix}$$

$$\mathbf{b} = \frac{\mathbf{b}_c (e^{-2\xi_g \omega_g \Delta t} - 1)}{-2\xi_g \omega_g}$$

ξ_g and ω_g are the damping ratio and angular frequency of the ground, respectively, Δt is the discretization time step and \mathbf{b}_c is as defined in Equation (3). Equation (4) shows the propagation of the system state in time. Using the UKF framework enables us to estimate the relative structural response \mathbf{u}_s and $\dot{\mathbf{u}}_s$ at every time step. The time step used throughout is the sampling time of the accelerometer.

Now, we define the structural acceleration a_{snk}

$$a_{snk} = \frac{\dot{u}_{snk+1} - \dot{u}_{snk}}{\Delta t} \quad (5)$$

where subscript n represents the n^{th} level where the accelerometer is placed, and subscript k indicates the k^{th} time step. We use this structural acceleration to calculate the ground acceleration as

$$a_g = a_{tn} - a_{snk} \quad (6)$$

where a_{tn} is the total acceleration measured by the sensor placed at the n^{th} story. From Equation (6), the ground acceleration and relative structural acceleration are separated from the measured observations of the accelerometers.

As it is processed, the ground motion data is simultaneously passed through a 2-pole, 0.075 Hz Butterworth filter. The first 3 seconds of the filtered ground motion p-wave acceleration data is recorded for further analysis and inference. The data is also simultaneously integrated recursively to obtain the ground velocity and displacement response history.

5.1.3.3 Inferences from first 3 seconds of p-wave data

The processed data for the first 3 seconds of the earthquake contains significant information about the seismic event. The measure of the frequency content of the recorded data is closely related to the intensity of earthquake. The peak ground displacement combined with the frequency content provide a good estimate of the hypocentral distance of the earthquake from the place of interest. There are two parameters used to measure the frequency content of the earthquake: τ_c [13-16] and τ_{pmax} [17-21].

τ_c is a measure of the average period of ground motion or the period of the monochromatic wave.

We first compute the moment rate function given as

$$r = \frac{\int_0^{\tau_0} \dot{u}^2(t) dt}{\int_0^{\tau_0} u^2(t) dt} \quad (7)$$

where τ_0 is 3 seconds from the onset of p-wave arrival, $\dot{u}(t)$ is the ground motion velocity and $u(t)$ is ground motion displacement. Parseval's theorem suggests that

$$r = \frac{4\pi^2 \int_0^\infty f^2 |\hat{u}(f)|^2 df}{\int_0^\infty |\hat{u}(f)|^2 df} = 4\pi^2 \langle f^2 \rangle \quad (8)$$

where f is the frequency, $\hat{u}(f)$ is the frequency spectrum of $u(t)$ and $\langle f^2 \rangle$ is the average of f^2 weighted by $|\hat{u}(f)|^2$. Combining the moment rate function and Parseval's theorem gives

$$\tau_c = \frac{1}{\sqrt{\langle f^2 \rangle}} = \frac{2\pi}{\sqrt{r}} \quad (9)$$

τ_{pmax} , unlike τ_c , is not the average time period with respect to the frequency content of the wave. Rather, it is the dominant time period of the wave in the time period under consideration. τ_p is determined recursively as a time series from the waveform. It contains the information about the frequency content of the seismic waveform up to the time at which it is calculated. Therefore, we calculate τ_p at every time step and the maximum of τ_p during the 3 seconds is τ_{pmax} . τ_p is calculated as

$$\tau_{p_k} = 2\pi \sqrt{\frac{X_k}{D_k}} \quad (10)$$

where k corresponds to the k^{th} time step and

$$X_k = \alpha X_{k-1} + \dot{u}_k^2 \quad (11)$$

$$D_k = \alpha D_{k-1} + \left(\frac{d\dot{u}}{dt}\right)_k^2 \quad (12)$$

where \dot{u}_k is the velocity at the k^{th} time step and α is a smoothing constant taken to be 0.99. The calculations for τ_p are started at $t=0.05\text{s}$ rather than $t=0.00\text{s}$ to avoid any error due to noise before the arrival of the p-wave in the recursive formulation.

The peak ground displacement (PGD) in the first 3 seconds is an important parameter as it correlates with the final peak ground velocity and hypocentral distance. Hence, we also record the PGD P_d contained in the first 3 seconds of the p-wave calculated from the integration of the separated ground motion acceleration signal.

5.1.3.4 Early prediction of earthquake parameters

The measured frequency content of the first 3s of p-wave is correlated to the moment magnitude of the earthquake. Although no direct relationship has been established, several empirical studies relate moment magnitude to the parameters calculated above. We use the results of these studies together to estimate a nominal mean moment magnitude M_w for the earthquake. The following empirical relations are used:

$$M_w = (\tau_c + 7.76)/1.56 \quad [60] \quad (13)$$

$$M_w = (\log_{10} \tau_c + 1.462)/0.296 \quad [52] \quad (14)$$

$$M_w = 4.218 * \log_{10} \tau_c + 6.1666 \quad [59] \quad (15)$$

$$M_w = 6.3 * \log_{10} \tau_p^{max} + 7.1 \quad [56] \quad (16)$$

$$M_w = 7 * \log_{10} \tau_p^{max} + 5.9 \quad [54] \quad (17)$$

$$M_w = \{(0.36 * \log_{10} PGA - 0.93 * \log_{10} P_d) - 5.495\}/(-0.615) \quad [55] \quad (18)$$

where PGA and P_d are peak ground acceleration and displacement, respectively, for the initial p-wave data.

From the above relations, we calculate the mean and standard deviation of the estimated moment magnitude of the earthquake. Due to uncertainty in this estimation and differences among the empirical relations, we create an array of 100 realizations of the moment magnitude for this earthquake by drawing randomized normally distributed values about the mean with the calculated standard deviation.

The next step is to predict the earthquake parameters: hypocentral distance R , significant duration t_{5-95} , and Arias intensity I_a . We predict the hypocentral distance R (km) from the site of interest based on the frequency content of the seismic wave and the PGD during the recorded 3 seconds. The empirical relation relating the hypocentral distance to the PGD (cm) and moment magnitude is

$$\log_{10} R = \frac{M_w - 4.748 - 1.371 * \log_{10} P_d}{1.883} \quad [59] \quad (19)$$

Note that M_w is now an array of 100 realizations. Therefore, we obtain an array of 100 values for R corresponding to each realization of moment magnitude.

The significant time duration t_{5-95} , defined as the time occurring between 5% and 95% of Arias intensity, is related to the moment magnitude and hypocentral distance. There are three possible relations, given in Equations (20)-(22), which can be used to find t_{5-95} with respect to each moment magnitude realization

$$t_{5-95} = 0.02 \exp(0.74M_w) + 0.3R \quad [66] \quad (20)$$

$$t_{5-95} = 11.2M_w - 53 \quad [67] \quad (21)$$

$$\log_{10} t_{5-95} = -1.3877 + 0.2451 * M_w + 0.6280 * \log_{10} \sqrt{4.5^2 + R^2} \quad [68] \quad (22)$$

Equation (21) works well only for $M_w > 6$ [32]. As an objective of this study is to create an automated system for earthquake early warning that is applicable across magnitudes of earthquake events, this relation is not used. We have found Equations (20) and (22) to produce similar results. However, Equation (22) is more computationally expensive. Therefore, Equation (20) is used in this study. It is noted that unlike M_w , the precise value of t_{5-95} does not significantly affect the outcome of the simulated ground motion. Therefore, while all 6 empirical relations are used to estimate M_w , and the mean and standard deviation of the result used for subsequent sampling, only one relation is used here. The result of this step is an array of 100 values for t_{5-95} .

Arias intensity depends on the acceleration content of the seismic waveform. In general, the Arias intensity of an earthquake is calculated as the sum of Arias intensities of the motion in both horizontal directions, i.e., $I_h = I_{EW} + I_{NS}$. In this study, we estimate the total horizontal Arias intensity based on moment magnitude, hypocentral distance and soil class [34]. However, we need the Arias intensity specific to the dominant direction. We approximate the predominant Arias intensity to be a mean 60% of the total horizontal intensity [69]. Equation (23) gives the Arias intensity for each site class multiplied by a randomized factor k sampled from a truncated normal distribution with mean 0.6 and varying between 0.5 and 0.7. ϵ is a random error normally distributed with zero mean and specified standard deviation.

$$\text{Soil class B} \quad I_a = k * \exp(2.071M_w - 2.178 \ln R - 8.492 + \epsilon(0,1.29)) \quad (23-1)$$

$$\text{Soil class C} \quad I_a = k * \exp(2.290M_w - 1.245 \ln R - 13.539 + \epsilon(0,1.23)) \quad (23-2)$$

$$\text{Soil class D} \quad I_a = k * \exp(2.155M_w - 1.323 \ln R - 11.920 + \epsilon(0,1.25)) \quad (23-3)$$

$$\text{Soil class E} \quad I_a = k * \exp(1.746M_w - 1.585 \ln R - 7.409 + \epsilon(0,0.82)) \quad (23-4)$$

Thus, we estimate the Arias intensity for the predominant direction for different site classes. However, if the site class is unknown, then conservatively site class D may be used. In this study, for a general structure situated on a site, we have assumed the site class to be D. If further information is available about the site of interest, the relation for that particular site class may be used. The result from this step is an array of 100 values of Arias intensity.

5.1.3.5 Simulation of ground motions

Next, we simulate synthetic ground motions using the predicted earthquake parameters. This is done by modulating a normalized white noise process in time as in [14]. We choose a gamma modulating function given as

$$q(t, \boldsymbol{\alpha}) = \alpha_1 t^{\alpha_2 - 1} \exp(-\alpha_3 t) \quad (24)$$

where $q(t, \boldsymbol{\alpha})$ is the time-modulating function, t is time, and, $\boldsymbol{\alpha} = (\alpha_1, \alpha_2, \alpha_3)$ are the parameters controlling the properties of the function. α_1 controls the intensity of the process, α_2 the shape and α_3 the duration of the motion. We use Arias intensity I_a , significant duration t_{5-95} and the time of occurrence of the maximum shaking t_{mid} defined as the time of 45% Arias intensity to calculate the parameters of the modulating function.

We estimate the total time period of the seismic motion as 3 times the significant duration [34]. The maximum intensity of an earthquake typically occurs during the initial phase with a longer right-side tail. Therefore, we factor the total time by a randomized factor normally distributed about a mean of 3 with standard deviation 0.5 to estimate t_{mid} . Now, we calculate $\boldsymbol{\alpha}$ as

$$\alpha_3 = \frac{1}{-\frac{t_{mid}}{2} + \frac{1}{4} \sqrt{4t_{mid}^2 + t_{5-95}^2}} \quad (25-1)$$

$$\alpha_2 = t_{mid} * \alpha_3 + 1 \quad (25-2)$$

$$\alpha_1 = \sqrt{I_a \frac{(2\alpha_3)^{2\alpha_2-1}}{\Gamma(2\alpha_2-1)}} \quad (25-3)$$

We estimate the impulse response function (IRF) of the filter as the pseudo acceleration response of a single degree of freedom linear oscillator as

$$h(t - \tau, \tau) = \begin{cases} \frac{\omega_f(\tau)}{\sqrt{1-\zeta_f^2}} \exp[-\zeta_f \omega_f(\tau)(t - \tau)] * \sin \left[\omega_f(\tau) \sqrt{1-\zeta_f^2}(t - \tau) \right] & \tau \leq t \\ 0 & \text{otherwise} \end{cases} \quad (26)$$

where t is the time at the k^{th} step under consideration, and both t and τ range from 0 to the total time duration.

We approximate the filter frequency ω_f and filter damping ratio ζ_f using the count of zero-level up-crossings [32]. We count the cumulative number of zero-level up-crossings at each time step during the recorded 3 seconds of motion and find the best second-order curve-fit approximation for it. The slope of the curve gives ω_f as a function of time. We are assuming ζ_f to be independent of time. It is estimated using the cumulative count of positive minima and negative maxima in the recorded motion compared to the count for a target accelerogram of the same duration for ζ_f values between 0.1 and 0.9. We assume the directional components of the ground motion to be correlated to follow the same trend.

The discretized model for the ground acceleration a_g is given as

$$a_g(t) = q(t, \alpha) * \sum_{i=1}^{k-1} \{s_i(t, t_i) w_i\} \quad (27)$$

where

$$s_i(t, t_i) = \frac{h(t-t_i, t_i)}{\sqrt{\sum_{j=1}^k h^2(t-t_j, t_j)}} \quad (28)$$

k is chosen such that $t_k = t$ and w represents zero-mean white noise. We note that this simulation process slightly overestimates the response over the period of the seismic event, and it should be passed through a high-pass filter. However, we use the original simulation result as the ground acceleration in this study to be conservative in the estimation. From this process, we obtain 100 sets of time histories of the ground motion, corresponding to the 100 sets of estimated earthquake parameters. We are then able to predict the maximum structural response for each simulated ground motion using Equation (4).

5.1.4 Results

We apply the proposed methodology to a single degree of freedom lumped mass system to estimate the maximum displacement response of a cantilever 12' W10X49 column under an example earthquake event. The coefficient of damping is assumed to be 5%. The ground motion used is the Chi-Chi earthquake because of the availability of consistent high-resolution data across stations for this event. Results for the application of the proposed methodology to other earthquakes are provided later in this section. In this section, we present results on the efficiency of the proposed method in terms of number of simulations and computational time, assess the estimation accuracy of the method, provide probabilistic inference on structural risk to the earthquake event, and investigate robustness of the prediction to variation in system parameters.

5.1.4.1 Application of methodology to Chi-Chi earthquake

We first identify the parameters ω_f and ζ_f for the ground motion simulation. To estimate ω_f , we count the cumulative number of zero-level up-crossings as described in Section 3 and curve fit this

as a second-order polynomial approximation. Its differential gives a first-order polynomial that represents ω_f varying in time.

To estimate ζ_f , we compare the cumulative number of positive minima and negative maxima of the ground motion with that of simulated accelerograms using different values of ζ_f . As the estimation of ζ_f is based on a cumulative count, a full time history is required to produce a reliable estimate of ζ_f [32]. Damping ratio is a ground property and we treat it as a constant predicted from any known ground motion time history at the site. Figure (6-2) shows the cumulative count of positive minima and negative maxima for the Chi-Chi earthquake for 3 directions of ground motion and simulated accelerograms for varying values of ζ_f .

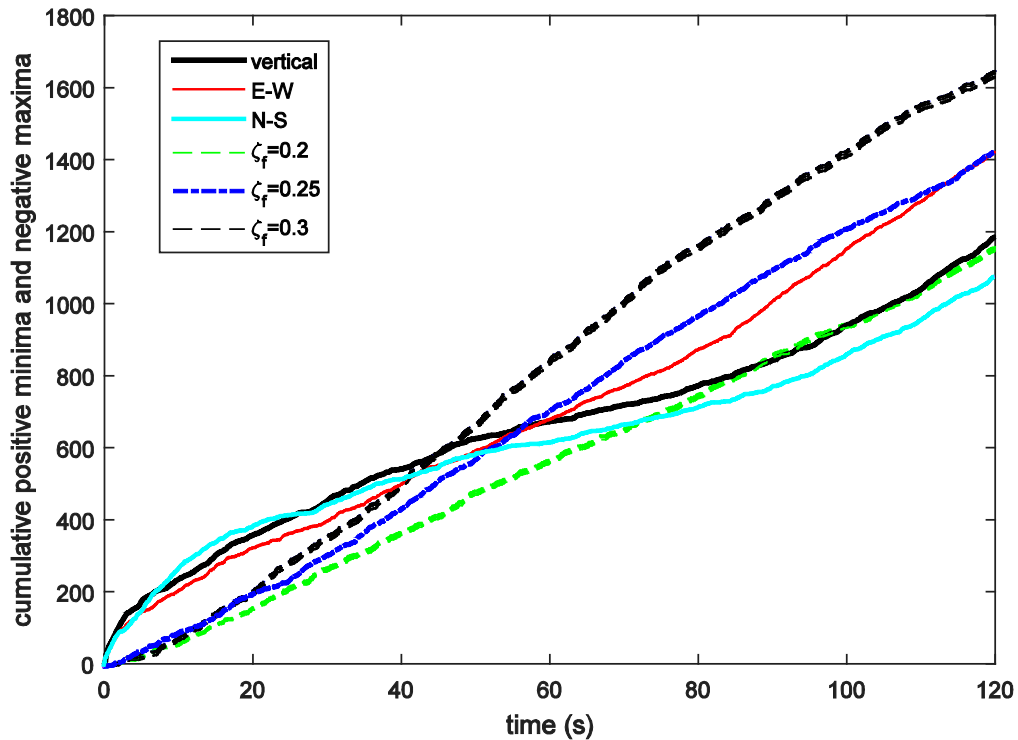


Figure 5-2 Characteristics of motion for 3 directional components of ground motion and varying values of ζ_f

From Figure (6-2), the cumulative counts of positive minima and negative maxima are similar for the 3 components of ground motion, supporting our initial assumption of a correlation between the directional components. For each ζ_f , each accelerogram will produce a different cumulative count plot. The plots for different accelerograms with similar ζ_f , however, are similar. Therefore, one simulation for each ζ_f is sufficient for comparison with the plot from the ground motion to find the best-fit ζ_f . From Figure (2), we choose $\zeta_f = 0.25$, which negates the error on either side, compared to $\zeta_f = 0.2$ and $\zeta_f = 0.3$, which underestimate and overestimate the ground motion plot, respectively. ζ_f is assumed to be constant and characteristic of the site location, calculated beforehand from any previous recording of ground motion at the site. Robustness of the proposed methodology to errors in the estimation of ζ_f is investigated later in this section.

Figure (6-3) shows an example of the separated ground acceleration in the first 3 seconds based on the structural sensor measurements. This data is used to identify the earthquake parameters as described in Section 3. From these, we then simulate 100 realizations of the ground motion, one of which is shown in Figure (6-4).

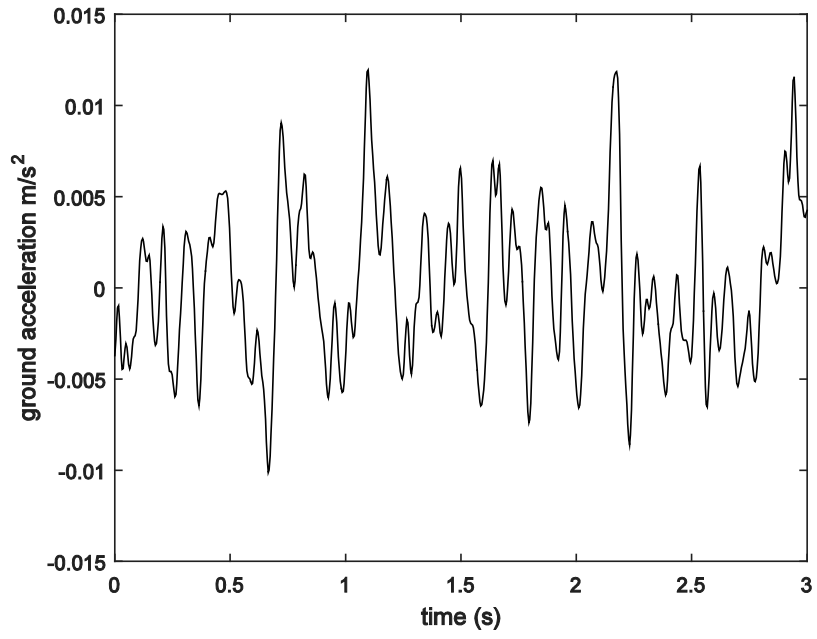


Figure 5-3 First 3 seconds of ground acceleration obtained from sensor measurements

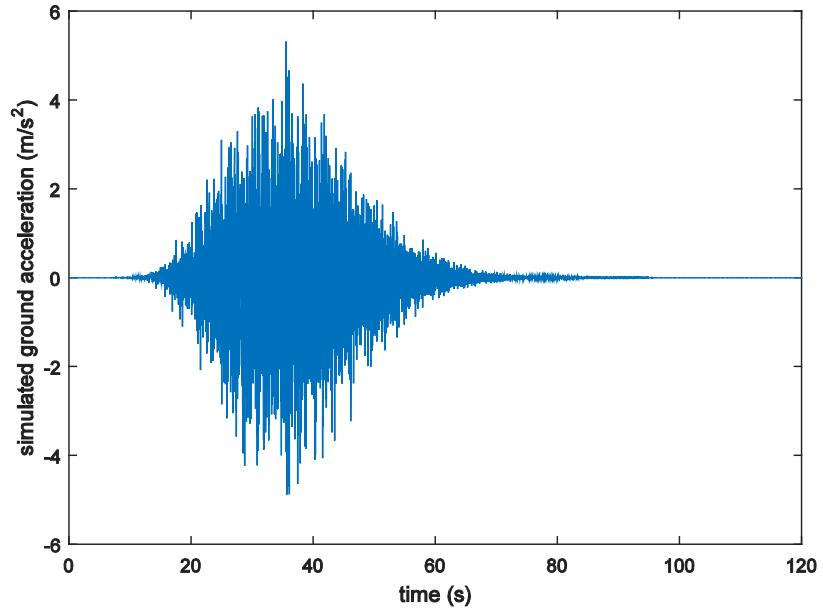


Figure 5-4 One realization of simulated ground motion

Under each ground motion simulation, we calculate the absolute maximum response of the structure using Equation (4). The predicted maximum response is then estimated as the mean of the results. This predicted maximum from the first 3 seconds of p-wave data is compared to the actual maximum response of the structure given the full ground motion record to assess the accuracy of the methodology.

5.1.4.2 Estimation accuracy and number of simulations

Figure (6-5) shows the variation in the accuracy of the methodology as a function of the number of ground motion simulations used for prediction. The rightmost plot for 100 simulations considers all 100 ground motions. The predicted maximum response (inches) is calculated as the mean of the 100 simulations. The leftmost plot considers the case of using only 1 simulation for prediction. In this case, the scatter of the possible predicted values for 100 cases of 1 simulation each is shown in the box plot, where the box represents the 25th to 75th percentile of predicted responses, the central line within the box indicates the median, and outliers are indicated as crosses. The results from using 10, 20, and 50 simulations are also shown.

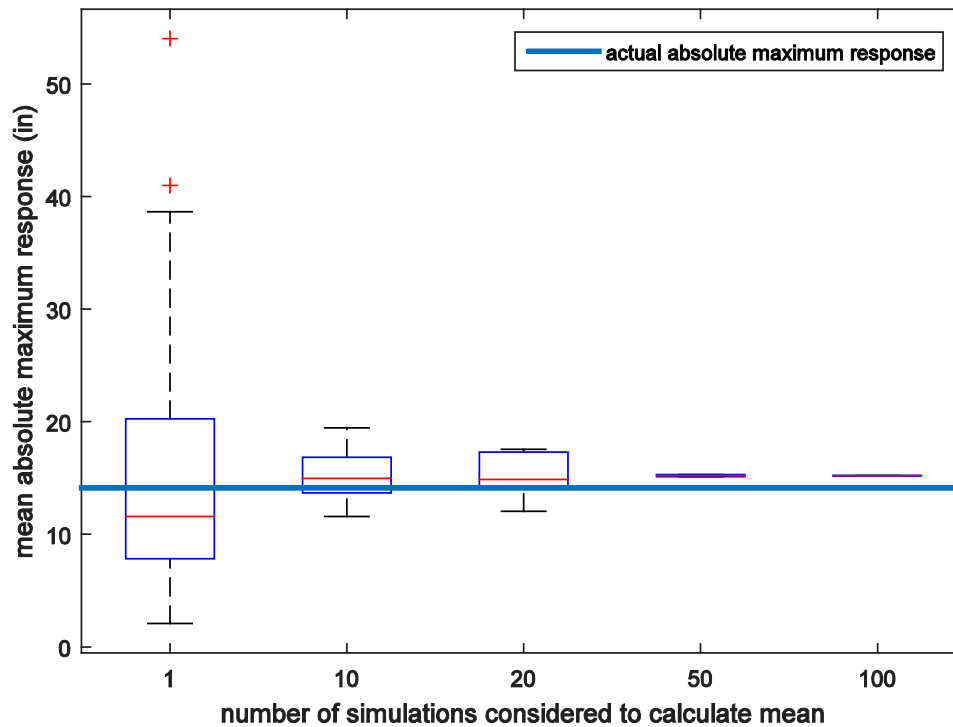


Figure 5-5 Distribution of mean maximum response with varying number of simulations

In Figure (6-5), the estimated mean maximum response converges to the actual maximum response with an increasing number of simulations. The spread of the predicted maximum response also decreases. The estimated mean converges to a value slightly higher than the actual absolute maximum response due to the conservative approach taken in the ground motion simulation process as described in Section 3.

Figure (6-6) shows the variation of root mean square (RMS) error and the total simulation time required to run the methodology for varying numbers of simulations.

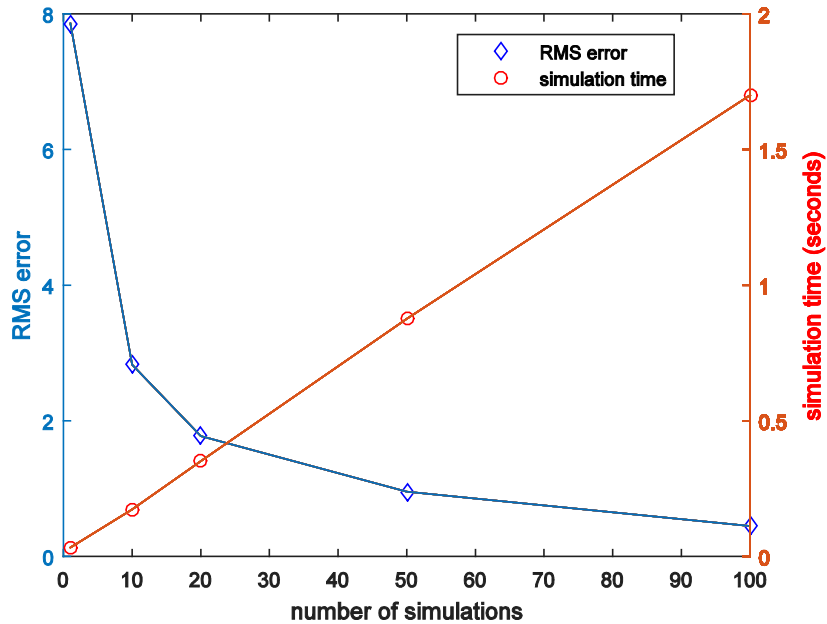


Figure 5-6 RMS error and simulation time vs. number of simulations

In Figure (6-6), we see that increasing the number of simulations decreases the error in the prediction. However, the cost of computation increases, as measured by the simulation time. The RMS error using 100 simulations is 3.17% of the actual maximum response compared to an error of 55.33% for a single realization. The time taken for 100 simulations is 1.79s compared to 0.033s for a single simulation. Looking at the trends of the two plots, the RMS error decreases exponentially, while the simulation time increases linearly as the number of simulations used in the prediction increases. The RMS error decreases with more simulations, but eventually levels off, whereas the time taken continues to increase. Using 100 realizations offers a reasonable tradeoff between computational time and RMS error. In addition, 1.78s of processing time from an initial 3s of data is an acceptable time for an earthquake early warning system, particularly considering full ground motion durations of 100-150s. Hereafter, 100 simulations of the ground motion are used for the results presented in this study.

5.1.4.3 Probabilistic inference on structural risk

Figure (6-7) shows that the distribution of the predicted maximum response follows closely the lognormal distribution. The mean and standard deviations of the fitted lognormal probability density function (PDF) are within 1% of the mean and standard deviations of the realizations. The fit is shown in the cumulative distribution function (CDF) given in Figure (6-8) as well, which plots the CDF of the realizations compared to the CDF for a fitted lognormal distribution. The highlighted boxed values are probabilities of not exceeding the actual (14.21 in) and estimated mean (14.81 in) maximum responses. Due to the conservative approach, there is a lower probability of exceedance for the estimated response. From Figure (6-7) and Figure (6-8), we see that a lognormal distribution can be used to estimate the probability of exceeding the safe threshold of a structure. Such probability of exceedance can be used to make inferences on the level of risk for a structure under a particular earthquake event.

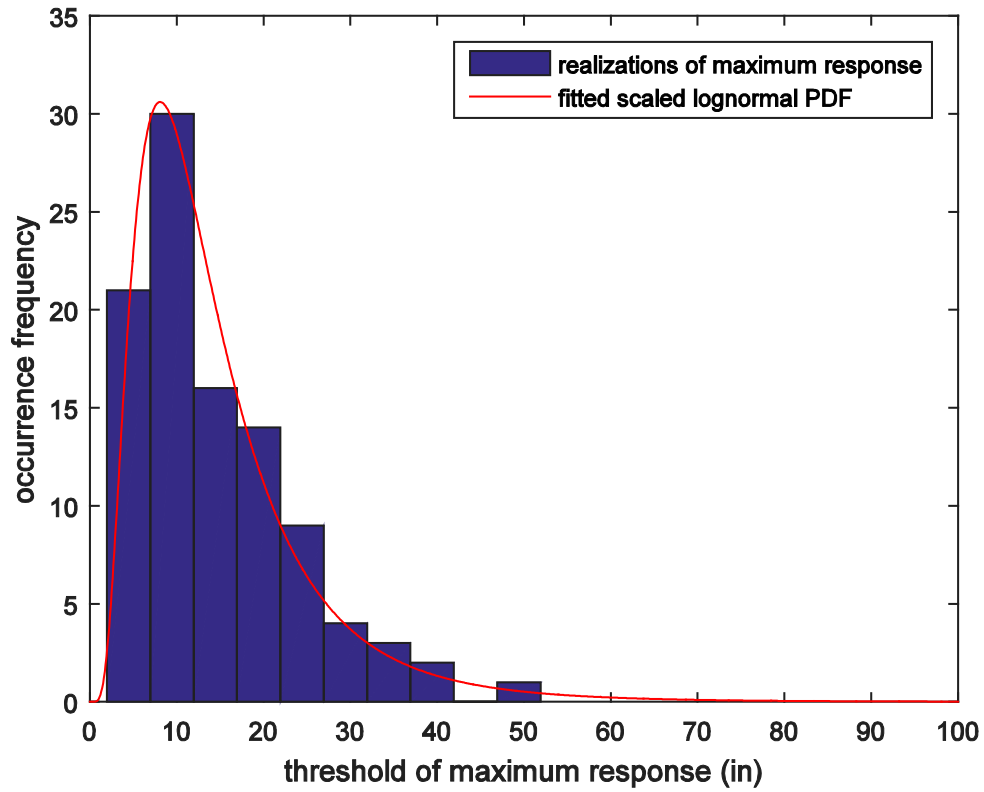


Figure 5-7 Distribution of simulated maximum responses and fitted lognormal PDF

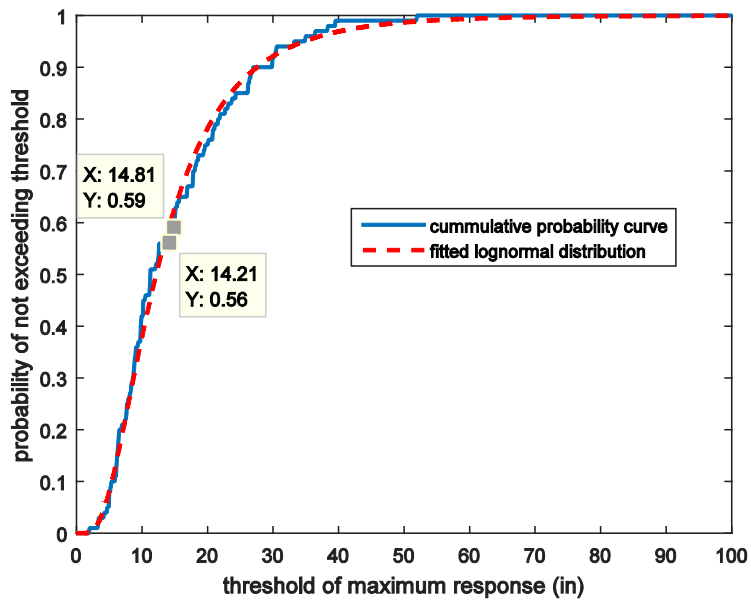


Figure 5-8 Cumulative probability of simulated maximum response and fitted lognormal CDF

5.1.4.4 Robustness to errors in estimation of ground parameters

Earlier, we described estimating the value of ground damping parameter ζ_f using the cumulative count of positive minima and negative maxima for the recorded ground motion compared to simulated accelerograms. We propose estimating ζ_f beforehand from previous recordings of ground motion at the site and using that value as a constant site parameter. Hence, ζ_f is only a function of the site and independent of other parameters. This assumption, however, introduces potential errors into the methodology. Here, we investigate the performance of the methodology given errors in the estimation of the parameter ζ_f . In Figure (6-9), we show the predicted maximum response compared to the actual response for varying values of ζ_f from 0.10 to 0.40 in steps of 0.05, as well as for parameter values randomized normally with mean 0.25 and standard deviations 0.05 and 0.10. 100 realizations of ground motion are simulated to calculate the mean absolute maximum response for each case.

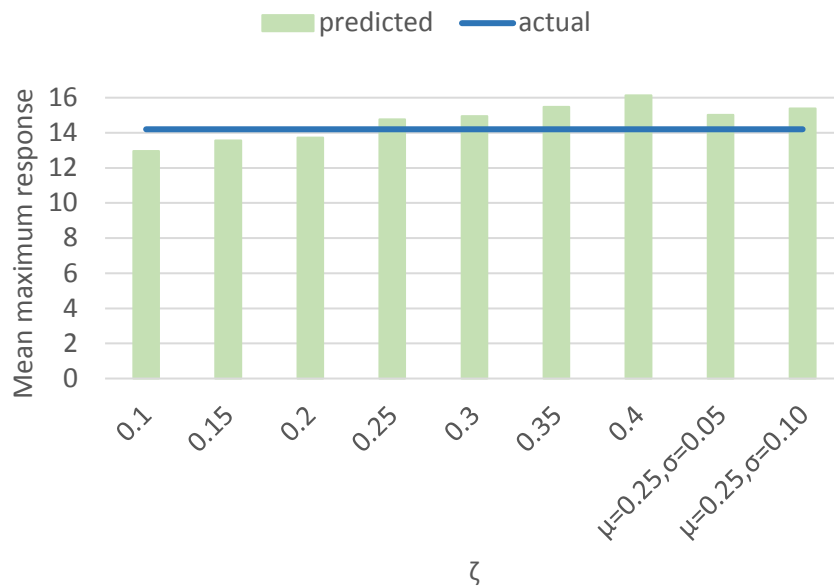


Figure 5-9 Variation of mean maximum response with varying ground damping coefficient ζ_f

Figure (6-9) shows the variation of the predicted mean maximum response for different values of ζ_f . We see that though the error increases with increasing error in estimation of ζ_f , the predicted response is within 10% of the actual response, on either side of the values of $\zeta_f = 0.25$. Additionally, the prediction shows a consistent trend over the range of ζ_f , and the two cases of randomized parameter values correspond well with the case of a deterministic $\zeta_f = 0.25$.

5.1.4.5 Robustness to uncertainty in structural parameters

The proposed methodology requires input structural parameters to calculate the structural response for each realization of ground motion. Structural parameters are typically estimated or modeled, for example, based on design drawings. There is uncertainty in this estimation, however. In the analyses thus far, we have used the assumed nominal values of the structural parameters. It is important to also assess the performance of the proposed methodology under the case of varying structural parameters subject to uncertainty. To do this, we lognormally vary the mass m , stiffness k , and damping c of the structure over a range of coefficients of variation (c.o.v.). Figure (6-10) shows the estimation results for c.o.v. of m and k ranging from 0% to 20% with a step size of 1% and c.o.v. of c varying from 0% to 40% in increments of 2%. With the 100 ground motions, we draw 20 and 100 realizations of m , k , and c for each value of c.o.v. The calculated mean of 20 and 100 mean maximum absolute responses at each variation in c.o.v. are shown.

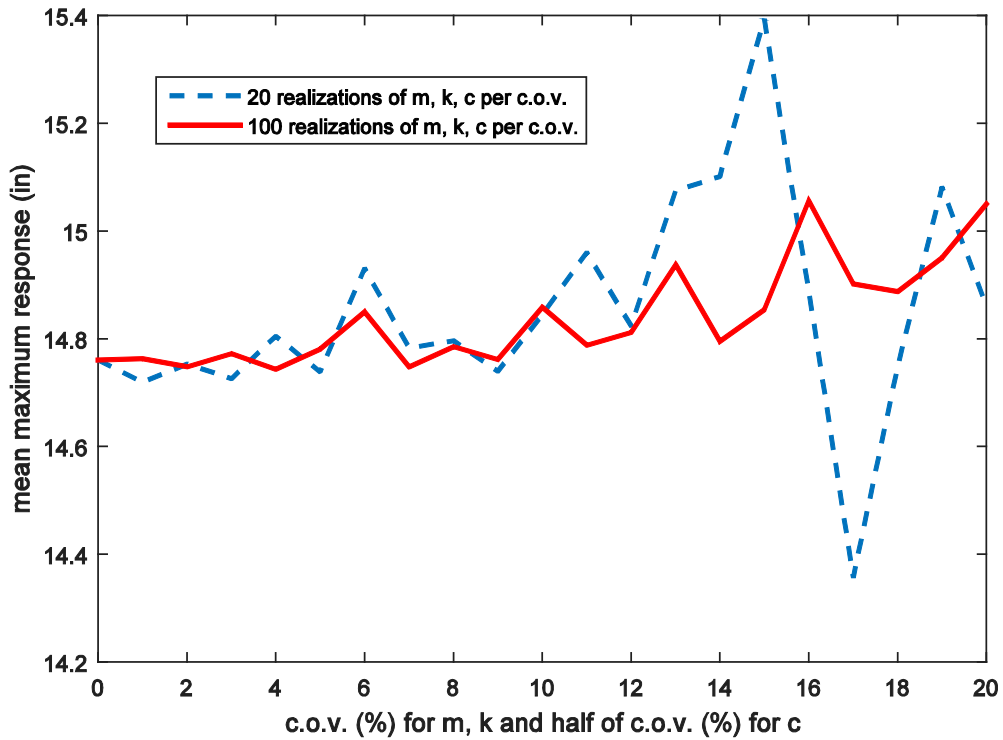


Figure 5-10 Variation of mean maximum response with varying m, k, and c

Noting the ordinate scale, Figure (6-10) shows the prediction of the maximum response to be robust to uncertainty in the structural parameters. For 20 realizations of m, k, and c, the maximum error is less than 4.5% of the estimated maximum response using the nominal values. For 100 realizations, the maximum error is less than 1.7%. The slight upward trend in the predicted mean maximum response as c.o.v. increases is due to the right skewness of the lognormal distribution. It is noted that a random variation of 20% c.o.v. for m and k and 40% for c is a significant variation from the nominal values. The accuracy of the prediction at such values shows the robustness of the methodology to uncertainty in the estimation of these structural parameters.

5.1.4.6 Cost of computation with increasing number of degrees of freedom

We have used a single degree of freedom system to demonstrate the methodology. However, it is also important to analyze the cost effectiveness of the methodology for higher degrees of freedom systems. In Figure (6-11), we compare the computational time required to run the methodology for systems with 1, 10, 100, and 1000 degrees of freedom. We first generate 100 simulations of the ground motion and calculate the response of the system under each of the ground motion realizations. We then calculate the mean of the absolute maximum response at every degree of freedom, which is the predicted maximum response at that degree of freedom.

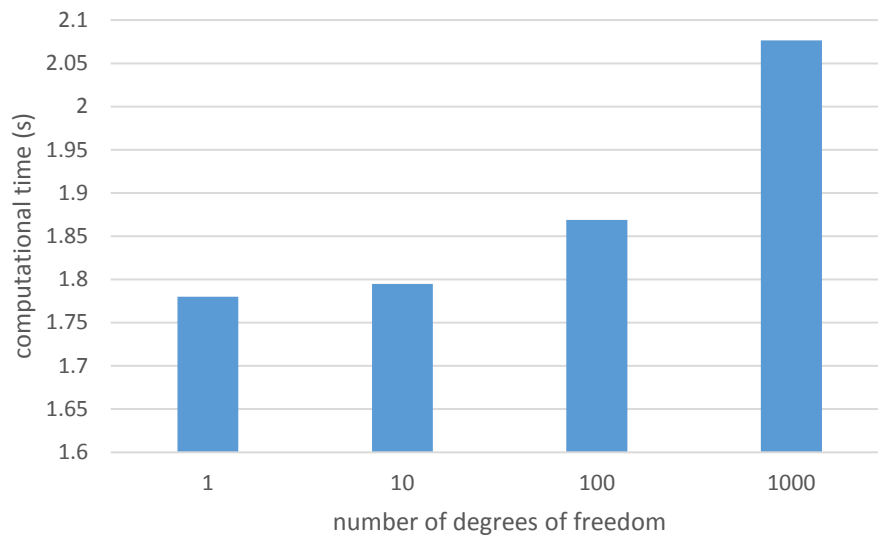


Figure 5-11 Computational time vs number of degrees of freedom of the structure

In Figure (11), we see that there is only a slight increase in the computational time as the number of degrees of freedom increases. Specifically, the computational time increases from 1.78 to 2.07 seconds when increasing from a single to 1000 degrees of freedom system. This is due to the majority of the total time being utilized by the simulation of ground motions. Once we have the 100 ground motion realizations, we are able to calculate the structural response for each realization

in parallel. Hence, the computational time is restricted not by the number of degrees of freedom of the system but the number of ground motion realizations. We note that we are using a sampling time of 0.004 seconds, corresponding to a sampling frequency of 250 Hz. This is equal to the sampling frequency of the accelerometer used to record the data for the Chi-Chi earthquake. If the sampling frequency is higher, then the computational time will be higher. A higher sampling frequency, however, provides more information, resulting in more accurate estimations. Hence, there is a tradeoff between accuracy and computational time for varying accelerometer sampling frequency. It is also noted that for practical structures, we can compress the actual system to use a model with fewer degrees of freedom if desired.

5.1.4.7 Performance of methodology for several earthquakes

Finally, we investigate the performance of the methodology for several earthquake events. These earthquakes are chosen to demonstrate the generalizability of the methodology across geographical locations and fault types. Table (6-1) provides the earthquake event, data sampling frequency, actual moment magnitude M_w , predicted M_w using the relations described in Section 3, and ground damping ratio ζ_f . The last two columns show the actual maximum response of the structure under the full earthquake event and the predicted maximum response using the proposed methodology. From Table (6-1), we see that while there is some variation in the accuracy of the estimated response across the earthquake events, the methodology based on the 3 seconds of initial data from building-mounted accelerometers is able to perform the prediction across a range of magnitudes of the maximum structural response.

Table 5-1 Performance of the methodology for several earthquakes

| Earthquake | Sampling frequency (Hz) | M_w | M_w predicted | ζ_f | Actual response (in) | Estimated response (in) |
|------------------|-------------------------|-------|-----------------|-----------|----------------------|-------------------------|
| Chi-Chi | 250 | 7.6 | 7.3 | 0.25 | 14.2 | 14.76 |
| British Columbia | 200 | 5.6 | 5.7634 | 0.35 | 0.1073 | 0.37 |
| Manjil, Iran | 100 | 7.4 | 6.4281 | 0.15 | 10.6254 | 13.53 |
| Alaska | 100 | 7.9 | 7.6487 | 0.2 | 6.2564 | 7.96 |
| Chile | 100 | 8.2 | 7.6519 | 0.2 | 1.9168 | 3.04 |
| Napa, CA | 200 | 6.0 | 6.2416 | 0.2 | 7.4328 | 9.28 |

5.2 Experimental study

5.2.1 Introduction

The experimental study uses the same setup for a two story instrumented structure, which is presented in the previous chapter. The methodology presented above is based on using the first few seconds of the p-wave data to estimate the earthquake parameters and predict the maximum structural response over the full excitation. As the accelerometers placed on the structure record absolute acceleration, we use the UKF-based formulation to separate the ground acceleration and the relative structural acceleration. The first three seconds of the p-wave acceleration is used to estimate the moment magnitude, hypocentral distance, and Arias intensity for the impending earthquake. Based on these parameters, we simulate a number of ground motions and predict the maximum structural response as an average of the maximum responses for all the simulated earthquake histories. Through numerical simulations, we have shown the predicted maximum structural response to be consistent with the observed maximum response. Performance is verified experimentally in this study with the observed maximum displacement responses for scaled earthquake histories applied to the lab-scale structure. The predicted responses are calculated independently based on the first three seconds of the p-wave data for the same earthquake.

5.2.2 Results

To evaluate the performance of the prediction methodology, three values for the maximum interstory displacement response are compared. The observed maximum response is the experimental result obtained from the LVDT measurements, the analytical maximum response is calculated based on information from the full time-history of the input acceleration, and the predicted maximum response is based on the first three seconds of the p-wave data. Table (6-2)

shows the comparison of the magnitudes of the three maximum responses for the Chi-Chi earthquake. The Chi-Chi earthquake is chosen as a demonstration due to its extensive instrumentation and study in the literature. As the LVDT cutoff is at 0.5in, the earthquake input history is scaled by 10%, 12%, and 15% for the experimental test structure. The p-wave is scaled with the same factor and used to predict the maximum structural response. To assess robustness to uncertainty in the response of a structure to a given earthquake, multiple experimental tests of a single earthquake are run.

For the 10% and 12% scalings of the input motion, the experiment is run three times. Table (6-2) shows the percent errors between the analytical and observed, predicted and analytical, and predicted and observed maximum displacement responses for each run. For the 15% scaled motion, the measured response exceeds the LVDT saturation point and therefore the comparison of accuracy for the predicted maximum is with the analytical maximum. The superscript (*) in the observed results for the case of the 15% ground motion scaling indicates that the LVDT has saturated. From Table (6-2), the predicted maximum response is slightly higher compared to the analytical or the observed response in all cases. This is due to the prediction methodology being conservative by design with the assumption of site class D soils and from not passing the process through an additional high-pass filter for the ground motion simulation.

The results in Table (6-2) show that the maximum response predicted based on the first three seconds of the p-wave data are consistent with the analytical and observed maximum responses. The predicted response is same for the three runs of the same scaling factor as it is predicted independently based only on the first three seconds of the p-wave data. The analytical and observed maximum responses are slightly different for every run of the same earthquake because of the uncertainty and noise in the actual and measured table input. Overall, the results show high

prediction accuracy, experimentally verifying the prediction methodology. The error between the three responses is quantified as a percentage error calculated as the absolute value of the difference between the two responses divided by observed or analytical response.

Table 5-2 Observed, analytical, and predicted maximum response for different scalings of Chi-Chi earthquake (* indicates LVDT saturation)

| Scaling factor for the s-wave | Observed maximum response (in) | Analytical maximum response (in) | Predicted maximum response (in) | Error (%) between analytical & observed | Error (%) between predicted & analytical | Error (%) between predicted & observed |
|-------------------------------|--------------------------------|----------------------------------|---------------------------------|---|--|--|
| 10% | 0.3347 | 0.3330 | 0.3417 | 0.51 | 2.61 | 2.09 |
| 10% | 0.3336 | 0.3315 | 0.3417 | 0.63 | 3.08 | 2.43 |
| 10% | 0.3333 | 0.3311 | 0.3417 | 0.66 | 3.20 | 2.52 |
| 12% | 0.4078 | 0.4095 | 0.4124 | 0.42 | 0.71 | 1.13 |
| 12% | 0.4073 | 0.4090 | 0.4124 | 0.42 | 0.83 | 1.25 |
| 12% | 0.4124 | 0.4146 | 0.4124 | 0.53 | 0.53 | 0.01 |
| 15% | 0.5* | 0.5636 | 0.5754 | -- | 1.02 | -- |

As shown in Table (6-2), the prediction errors are small. The results in Table (6-2) are based on utilizing three seconds of p-wave data and 100 simulations of the ground motion. In this methodology, for a useful real-time prediction of maximum response, such as for an early warning system, the time and computational cost are significant. Therefore, the effect of using varying amounts of data on the accuracy and computational time for the prediction is evaluated. Figure (6-12) shows the error in prediction of the maximum response as a function of the number of simulations of the ground motion and the amount of initial data used in terms of seconds. The error is evaluated for conducting a number of simulations ranging from 1 to 100 and using between one and five seconds of initial p-wave data. The error is calculated as the percentage of the difference between predicted and observed maximum responses with respect to the observed maximum response. As shown in Figure (6-12), as expected, the accuracy of the prediction increases with increasing number of simulations and increasing amount of initial data used. However, with increasing number of simulations and more initial data, the total computational time also increases, as shown in Figure (6-13).

The tradeoff is between accuracy and computational time, with computational time affected by both the number of ground motion simulations conducted and the amount of initial data used. Figure (6-12) shows that increasing the number of simulations has a greater effect on decreasing the error in comparison with increasing the amount of initial data used. At the same time, Figure (6-13) shows that increasing the number of simulations does not increase the computational time as much as increasing the amount of initial data used does. Therefore, increasing the number of simulations is preferred to increasing the amount of initial data in order to improve the accuracy of the prediction while limiting increases in computational time. For example, using the first three seconds of data and 100 simulations provides a reasonable tradeoff between error and total time.

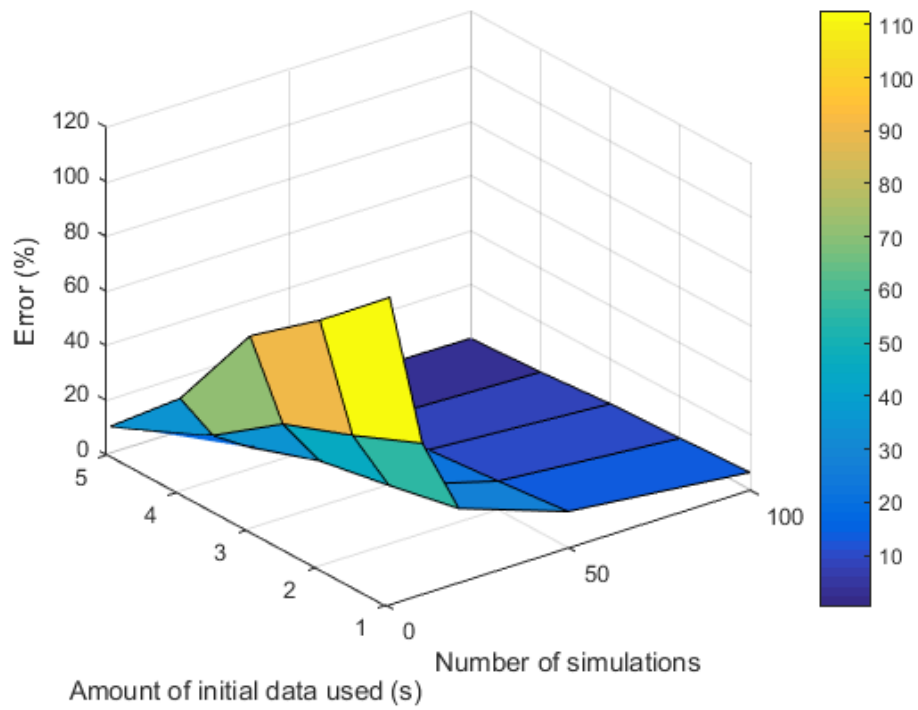


Figure 5-12 Comparison of error in prediction with respect to number of seconds of initial data used and number of ground motion simulations

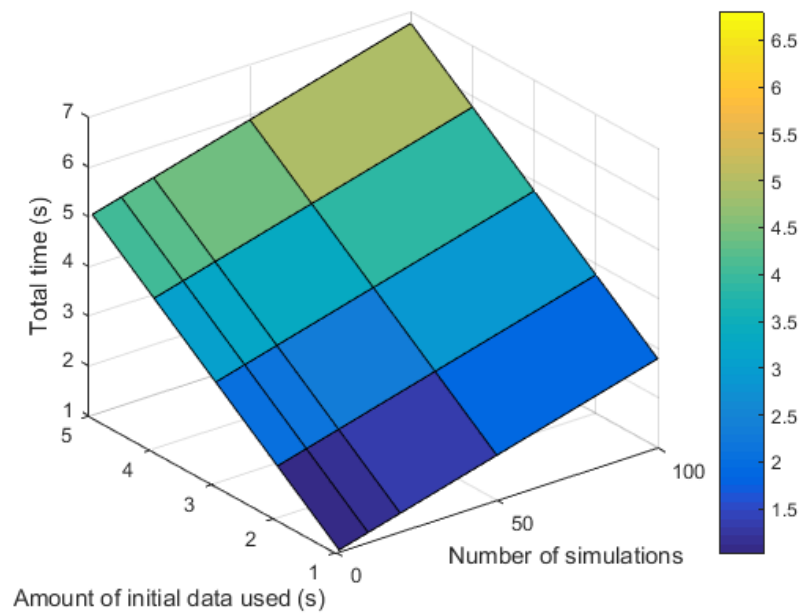


Figure 5-13 Comparison of total computation time with respect to number of seconds of initial data used and number of ground motion simulations

5.3 Conclusion

The proposed methodology provides an estimation of the maximum response of a structure under an earthquake threat. Based on the predicted maximum, a localized earthquake early warning can be issued. We use information from the first 3 seconds of data recorded by accelerometers placed on the structure, rather than seismograph data, to estimate various earthquake parameters for modeling the ground motion. We find 100 ground motion simulations to achieve a reasonable trade-off between estimation accuracy and computation time. The methodology for maximum response prediction is shown to be robust to uncertainties in the estimation of both ground and structural parameters, and applicable across earthquake-prone regions.

We infer the risk to a structure based on the predicted maximum response. However, we can also look at the projected total response of the structure depending on the criteria defined for failure. To show the generalizability of the method, in this study we did not include specific seismic or site information in the calculations. In the case of regions where studies have defined the relationships between various earthquake parameters, for example, studies for the California area on the relationships between moment magnitude, significant duration, and hypocentral distance, that information can be included in the methodology for improved estimates through fewer simulations. Information on fault type and soil class can also be easily incorporated for improved site-specific results.

The methodology for earthquake early warning enables computationally efficient inference on the specific structural risk under an earthquake threat rather than issuing a regional warning. The system can be augmented through incorporation of any known seismic information at the site under

consideration. However, we have shown that even with a minimalist approach, the information from accelerometers mounted on a structure can be used for real-time response prediction to issue a structure-specific earthquake early warning.

The formulation in the previous chapter provides a foundation, which is used to draw inferences on an impending earthquake for the prediction part of the study. In predicting the maximum structural displacement response for an impending earthquake, the predicted maximum response based on only the first three seconds of the p-wave data is compared with the experimentally observed maximum response from the full ground motion for experimental verification. Across scalings and motions, the proposed prediction methodology performs within 3% error for the prediction of the maximum response. The methodology works in real time and is shown to be efficient in terms of computation time. In assessing the impact on the accuracy of the prediction of the amount of initial data used and the number of simulations conducted, using the first three seconds of data and 100 simulations provides a reasonable tradeoff between error and total time. The framework can be used for a structure-specific earthquake early warning system based on the predicted maximum response. It can be extended to use with active or passive structural control systems to alter structural stiffness or damping based on the predicted maximum responses for increased reliability under an impending earthquake. This study experimentally verifies the methodologies for both real-time estimation and prediction of structural response based on the building accelerometer data.

CHAPTER 6. LONG-TERM RELIABILITY: IMPACTS OF CLIMATE CHANGE ON THE ASSESSMENT OF LONG-TERM RELIABILITY

6.1 Introduction

Global climate change is one of the most important concerns that we face in the coming years. The effects of climate change are multi-dimensional, ranging from natural ecosystems to the built environment, with social, health, safety, and economic impacts. Therefore, the study of the effects of global climate change is relevant in many science and engineering disciplines, including civil engineering. Civil engineering infrastructure is required to withstand and resist any weather-based environmental activity. Further, civil engineering infrastructure is designed to function over many decades. There exists a direct connection between the changes in short-term weather patterns and long-term climate fluctuations with the state of infrastructure. Therefore, it becomes necessary to study the effects of climate change on long-term structural reliability.

Climate change models provide projections of global and regional changes for different environmental parameters and natural hazards. In considering civil infrastructure reliability, environmental factors such as concentration of carbon dioxide and temperature may affect the rate of corrosion, while temperature also induces thermal loads, effectively reducing the available resistance of infrastructure components. In addition, the change in the frequency, intensity, and extent of natural hazards including hurricanes, tornados, snow, and precipitation affect the design load on the structure. While a relatively small short-term change may not be significant, the changes in long-term reliability need to be studied to address sustained incremental changes.

In this paper, the authors study the impacts of climate change by quantifying the individual effects of changes in different environmental factors on the resistance and loading of a structure. The probabilistic assessment of individual variation in both the resistance and load functions at an instant of time allows for the approximation of structural reliability at that time. Performing similar calculations over longer time scales enables estimation of the time-dependent variation of reliability over a duration of time. As infrastructure components are expected to function over long service lifetimes, it becomes important to assess the change in reliability over the duration of the design life, while simultaneously accounting for the changes in the surroundings and environment during the time period. It is noted that the results presented are valid in relative terms, compared to the case without considering such effects.

This study uses climate change projections to investigate their impacts on civil infrastructure. The effects of a rise in temperature are threefold on the structure with a decrease in modulus of elasticity, induced thermal loads, and increased rate of corrosion. The increase in the level of carbon dioxide promotes carbonation and a decrease in the strength of concrete and masonry. The increase in environmental loads depends on the increase in both the extremes and frequencies of natural events. It is noted that such changes vary from region to region. This study uses global means to investigate the need to incorporate climate change in the assessment of structural reliability.

6.2 Background

There are several extensive climate change models in the literature. However, the Intergovernmental Panel on Climate Change (IPCC) reports [15] provide the most widely accepted projections of long-term climate patterns. This study uses the mean global climate projections from

the IPCC fourth assessment report (Meehl et al, 2007) [15]. These models estimate the change of a quantity projected over a certain number of years. In this study, the authors assume that the change occurs linearly within the time period of interest. This is in accordance with the fact that the global carbon dioxide level has historically increased approximately linearly. While temperature changes appear to be correlated logarithmically to the carbon dioxide level, the difference between a linear or logarithmic assumption is negligibly small for a change of a few degrees in temperature over several years.

Studies on time-dependent structural reliability include Li, Wang, and Ellingwood, 2015 [16] who studied structural reliability under non-stationary loads. They proposed a methodology to model the time-dependent resistance function, subtracting the dead loads to obtain the resultant available resistance, and finding the probability of non-stationary loads exceeding the resistance at any time instant. Thus, time-dependent probability of failure of the structure can be estimated using the distribution of extremes of the expected live loads or environmental loads. While the effect of non-stationary environmental loads and aging are analyzed in that study, here, the authors aim to specifically investigate the impact of climate change variables on long-term structural reliability.

Peng, Shao, and Zhang, 2009 [70] studied the effect of increased carbon dioxide emissions on the carbonation of concrete structures and structural reliability over time. They used predictive carbonation depth models to estimate reliability by accounting for levels of carbon dioxide, corrosion mechanisms, material strength, structural dimensions, and the ambient structural environment. The results show that the probability of corrosion initiation can be as high as 4.6 times the non-impacted case. Stewart, Wang, and Nguyen, 2011 [71] also studied the impact of a rise in carbon dioxide levels on concrete infrastructure. They similarly used extended carbonation depth, corrosion initiation, and reliability models on carbonation to estimate the structural

reliability. An increase in damage due to carbonation of up to 400% by 2100 was found. Compared to the previous work in carbonation, this study performs a comprehensive investigation of the effects of climate change on reliability, including impacts on all degradation mechanisms and loadings on a structure. Climate change effects on a failure mechanism are correlated to strength, and a fractional change in strength is then assessed rather than using failure mechanism models. The aim is to investigate a need to include climate change in assessment of long-term structural reliability. In addition, the previously used models for carbonation require extensive knowledge of the structure and environment. The generalized methodology presented in this paper is not limited to a structure but can be used across infrastructure in a region.

The following climate-dependent modes of degradation are considered in this study. The modulus of elasticity of any structural material decreases with an increase in temperature. The decrease tends to be linear at lower temperatures and exponential at higher temperatures. Therefore, for the temperature ranges considered within the scope of this study, the decrease in modulus of elasticity with increasing temperature is assumed to be linear. The increase in temperature also induces thermal loads. Depending on the end fixity conditions, a maximum thermal stress of $E\alpha\Delta T$ is generated, where E is the modulus of elasticity, α the coefficient of thermal expansion, and ΔT the change in temperature. Temperature also affects the rate of corrosion of an element. Corrosion depends on several environmental factors including moisture content, temperature, and exposure to various chemical agents, with the rate of the chemical reaction increasing with an increase in temperature. The Arrhenius equation for reaction rates suggests that the rate of a chemical reaction increases exponentially with temperature. While long-term corrosion of civil engineering materials generally does not follow a strict exponential trend due to a simultaneous dependency on several

other factors, it is reasonable to assume an exponential variation for the temperature ranges considered in this study.

Concrete is the most widely used construction material, followed by steel and masonry. The strength of reinforced concrete and masonry is significantly affected by carbonation. Carbonation reduces the material strength and leads to the corrosion of steel reinforcement. Chi, Huang, and Yang, 2002 [72] studied the effect of carbonation on the mechanical properties of concrete. They found the strength of concrete to be inversely proportional to the depth of carbonation. A study by Sagiús, Moreno, Morris, and Andrade, 1997 [73] shows that the depth of carbonation is directly proportional to the square root of the concentration of atmospheric carbon dioxide. Therefore, it is assumed that the long-term strength is negatively correlated to the square root of the atmospheric carbon dioxide concentration. The modes of degradation as applied to a demonstrative concrete structure, as well as example steel and wood structures, are considered in this study.

6.3 Methodology

6.3.1 Modeling of structural resistance and loads

Following [16], the structural resistance is assumed to decrease with time such that $R(t) = R_0G(t)$, where $R(t)$ is the structural resistance at time t , R_0 is the initial resistance, and $G(t)$ is the degradation function. $G(t)$ is a stochastic function and it is generally modeled using simple polynomial functions as proposed in [74-76] and used [16], where the reliability is assessed using simplistic polynomial models, i.e., linear, squared, and square-root functions of time t . However, based on the mechanical properties of the modes of degradation considered and to understand the effect of these different factors on the resistance function, the authors propose a model for the degradation function given as

$$G(t) = 1 - at - b\sqrt{t} - \exp\left(\frac{c}{t}\right) \quad (1)$$

The terms in this formulation account for the variations in resistance due to different degradation factors. Specifically, the square-root term accounts for carbonation, the exponential term accounts for accelerated corrosion due to temperature, while the linear term accounts for other mechanisms of degradation including fatigue. Carbonation primarily affects concrete and masonry. Carbonation and corrosion are not independent for these structures. Carbonation acidifies the aggregate reducing the strength of the composite, while simultaneously allowing increased penetration of moisture and oxygen to the reinforcement. In this study, however, carbonation is related to the acidification of the composite and temperature is attributed to the corrosion rate. The variation in carbon dioxide and temperature levels are correlated, but treated separately in the degradation function as each factor, acidification and corrosion, affects a structure differently. In the context of climate change, increased fatigue can be due to more severe freeze-thaw cycles or heat events. The linear term could be replaced by any other simplistic polynomial function based on the dominant degradation mode. For simplicity and assuming fatigue to be dominant compared to other strength-reducing factors, it is assumed to be linear in this study.

The degradation function is applicable to other types of structures through proper choice of the parameters. A steel or wood structure, for example, will not be sensitive to carbonation. The dominant modes of degradation for a steel structure are corrosion and fatigue. Similarly, a wood structure is highly sensitive to moisture content and temperature. Almost all mechanical properties of wood decrease with increases in temperature or moisture content. Most studies on properties of wood linearly relate the logarithm of a mechanical property of wood to moisture content and

temperature as in Gerhards, 1982. Therefore, the same degradation function is applicable to steel and wood structures with the exclusion of the square-root term.

The selection of parameters has a significant impact on results. In general, the parameters of the degradation function are estimated and can be updated through periodic inspections or observations of the structure. The parameters a , b , and c are estimated by assuming that each term is driven solely by the attributed degrading mechanism, such that fatigue only affects a , carbonation b , and corrosion c . Therefore, an attributional quantification of the fraction of the total degradation caused by each degradation mechanism helps in estimating these parameters. Such fractional attribution of the degradation among several damaging mechanisms depends on the type of structure, its usage, and its location. For example, the degradation of a steel structure will be dominated by corrosion while concrete may be dominated by carbonation, and a coastal structure is more prone to corrosion while a bridge deck is prone to fatigue. The results for a demonstrative example presented in this study assume 10% of the degradation is due to carbonation, and corrosion and fatigue each contribute 45% of the degradation for a concrete structure. These values are selected as a concrete structure is most affected by corrosion and fatigue in the long run. Carbonation catalyzes corrosion and also acidifies the composite. As this study treats corrosion and acidification separately, the effect of corrosion and fatigue on the overall strength is given a higher weight compared to the carbonation-induced acidification. Results for example steel and wood structures are also given with varying parameter selection values for the degradation function. In addition, results of a sensitivity analysis are provided to investigate the effect of changes in parameters on the results presented. The attribution of fractions of degradation to specific mechanisms for different structures can be adjusted based on periodic observations and degradation quantification for any structure of interest. The periodic observations of a structure

and tests using NDE techniques can help estimate the extent of a specific degradation mode, e.g., extent of corrosion in reinforced concrete or amount of moisture in wood. These observations should be used to update the parameters selected for the degradation function to change the weights of the dominant modes of degradation for a structure over time.

The environmental load events considered in this study are assumed to be Poisson processes with time-dependent mean occurrence rate $\lambda(t)$ and mean load intensity $\mu_s(t)$, where the subscript s denotes structural loads. The changing mean rate and mean intensity parameters model the increasing frequency and severity of climate-dependent natural hazards including hurricanes, tornados, and rain and snow events.

6.3.2 Reliability analysis

The probability of failure P_f of the structure at any instant of time is given as

$$P_f(t) = P[R(t) < S(t)] = \int_0^{\infty} F_{R,t}(s) f_{S,t}(s) ds \quad (2)$$

where $R(t)$ is the resistance function, $S(t)$ denotes the load effect, and F and f represent the cumulative distribution function (CDF) and probability distribution function (PDF), respectively. R and S are assumed to be statistically independent.

The hazard function $h(t)$, defined as the probability of failure of the structure in the time interval from t to $t + dt$ given that the structure has survived up to time t , is expressed as

$$h(t) = \frac{P(t_f \leq t + dt | t_f > t)}{dt} = \frac{P(t < t_f \leq t + dt)}{P(t < t_f) dt} \quad (3)$$

where t_f is the time of failure. The numerator of equation (3) can be expressed as

$$P(t < t_f \leq t + dt) = \lambda(t)dt \cdot P[R(t + dt) < S(t + dt)] \cdot P(t < t_f) \quad (4)$$

Hence, the hazard function becomes

$$h(t) = \lambda(t) \cdot P[R(t + dt) < S(t + dt)] \quad (5)$$

Ignoring the randomness in the estimation of the parameters a , b , and c and assuming dt is infinitesimally small so that no uncertainty is induced in the estimation of $G(t + dt)$ given $G(t)$, $G(t + dt)$ and hence $R(t + dt)$ are deterministic such that

$$P[R(t + dt) < S(t + dt)] = 1 - P[S(t + dt) < R(t + dt)] = 1 - F_S[R(t + dt)] \quad (6)$$

The hazard function is then written as

$$h(t) = \lambda(t) \cdot [1 - F_S\{R(t)\}] \quad (7)$$

The hazard function is also related to the structural reliability $L(t)$ as proposed by Ellingwood and Mori, 1993

$$h(t) = -\frac{d}{dt} \ln[L(t)] \quad (8)$$

Therefore, the structural reliability and probability of failure are expressed as

$$L(t) = \exp\left[-\int_0^t \lambda(t) \cdot [1 - F_S\{R(t)\}] dt\right] \quad (9)$$

$$P_f(t) = 1 - L(t) \quad (10)$$

6.3.3 *Climate change projections*

The IPCC report, Meehl et al, 2007 presents a number of different models to project the change in the physical climate-related parameters of interest. The average global temperature increase is projected between 1.79°C and 3.13°C for 2000-2100 as estimated by different models. In this study, a temperature increase of 2.65°C in 100 years is used, a value proposed by one of the projection models and lying within the range of the projection. Similarly, different models project the increase in the concentration of carbon dioxide to be 2 to 2.5 times from 2000-2100. Hence, this study uses an estimated 100% increase in 100 years for the carbon dioxide levels.

The change in the intensity of the extremes of natural events directly affects the environmental loads on the structure. For example, the maximum surface wind speed of hurricanes and cyclones are expected to increase by 6-14% by the end of the century, precipitation extremes are projected to increase by 4-5%, increased wave heights and a rise in sea levels is expected, and there is an increased possibility of more intense extratropical storms and snow events. Such changes in the extremes of these events increase the environmental loads on structures during significant load event occurrences. Increases in hazard extreme intensity of 5%, 10%, and 15% over 100 years are used in this study.

6.4 Application and results

To estimate the parameters of the degradation function, this study assumes that the resistance at the end of 40 years is 80% of the initial resistance. This assumption is in accordance with Li, Wang, and Ellingwood, 2015 [16] to facilitate comparison of our results with those of the previous study. While the value of reduction in structural strength would vary by type of structure and location, the aim of this study is to compare the probabilities of failure at a particular time instant

with and without including the effects of climate change. Thus, $G(40) = 0.8 = 1 - a \cdot 40 - b\sqrt{40} - \exp\left(\frac{c}{40}\right)$. For this application, the authors assume that 10% of the degradation of the structure is due to carbonation while corrosion and fatigue contribute to 45% of the degradation each. The three unknown parameters may therefore be calculated by equating the fraction of total decrease to individual terms. This results in values for a , b , and c of $\frac{0.09}{40}$, $\frac{0.02}{\sqrt{40}}$, and $\ln(0.09) \cdot 40$, respectively.

The demonstrative percentages for attributional causes of degradation would vary depending on several factors, including the type of structure, location, exposure, and loading. To study the sensitivity of the degradation function to the choices of the values of the three parameters, a local sensitivity analysis is performed. A normalized sensitivity coefficient φ_i for a particular independent variable X_i for the degradation function G is calculated as

$$\varphi_i = \frac{\partial G}{\partial X_i} \cdot \frac{X_i}{G} \quad (11)$$

where $X_i = a, b, \text{ or } c$ are the parameters of degradation function. Under the current assumptions and $t = 40$ years, the absolute values for φ are $\varphi_a = 0.112$, $\varphi_b = 0.025$, and $\varphi_c = 0.271$. These values represent the sensitivity of the model to different assumed parameters and quantify how the degradation function is expected to change with changes in estimates of the parameters. From the results, the function is most sensitive to the parameter c , followed by a and then b . The parameters b and c are the climate-dependent factors in the degradation function, with the model being more sensitive to c compared to b .

The design equation $0.9R_n = 1.4D_n + 1.7L_n$ specified in ACI 318 and as used in Li, Wang, and Ellingwood, 2015 is used to estimate nominal dead load, where the subscript n denotes nominal

or code-specified values. While this code has since been superseded by newer codes, it was chosen to facilitate comparison with other studies that do not consider climate change factors. For simplicity and to be consistent with Li, Wang, and Ellingwood, 2015, it is assumed that $D_n = L_n$ and $R_n = R_0$. The dead load is assumed to be stationary and constant such that it can be directly subtracted from the resistance function to estimate the reliability of the remaining effective resistance against the environmental load. The reliability hence becomes

$$L(t) = \exp\left[-\int_0^t \lambda(t) \cdot [1 - F_S\{R_0 \cdot G(t) - D_n\}] dt\right] \quad (12)$$

The environmental load is assumed to be Poisson distributed with mean rate of occurrence 1/year. This models an extreme environmental load such as a hurricane. The occurrence of such loads can be estimated as Poisson events though their effect on a structure is not necessarily Poisson. Here, the effect is also estimated to be Poisson, due to an estimate of a simultaneous reaction of a structure to the load and negligible residual effects compared to the service life of the structure. The case for two dependent or simultaneously occurring environmental load events can be similarly analyzed by using the joint rate of occurrence and joint mean intensity.

Here, the mean of the extreme load is assumed to be $\mu_S = 0.6L_n$ (which will later be varied in this study to reflect increasing intensity of extreme hazard events with climate change), with coefficient of variation 0.3, and it is assumed to follow a Type 1 distribution as in Li, Wang, and Ellingwood, 2015. This choice of the mean of the extreme load makes the design equation the critical design equation at the mean. Note that, in general, the critical design equation depends on load combinations and type of dominant hazards in the area.

With the selected parameters, first, the impact of climate change on the resistance is studied without varying the properties of environmental loads. The effect of changes in each parameter is studied separately and then aggregated to analyze the combined effect. The modulus of elasticity decreases with elevated temperatures and is directly proportional to the structural resistance. The change in resistance is normalized to the fractional change in the modulus of elasticity. This is accounted for in the reliability as

$$L(t) = \exp \left[- \int_0^t \lambda(t) \cdot \left[1 - F_S \left\{ R_0 \left(G(t) - \frac{\Delta E}{E} \cdot \Delta T(t) \right) - D_n \right\} \right] dt \right] \quad (13)$$

where ΔE is the change in modulus of elasticity per °C at lower temperatures, E is the design modulus of elasticity, and ΔT is the change in temperature with time. ΔE is taken to be 17 MPa per °C, E 31 GPa (typical for concrete) from Naus, 2005, and ΔT 2.65°C in 100 years, assuming temperature change to be linear in time.

Elevated temperatures also increase thermal loads in the structure. Assuming end conditions such that temperature increases cause corresponding full thermal stresses, the degradation function decreases by an amount equal to $\alpha \Delta T$. Though this assumption may not be valid for the case of expansion and construction joints, given the value of the coefficient of expansion for structural materials and the projected change in temperature, the effects are small for the assumption to be valid. This is reflected in a corresponding change in structural reliability as

$$L(t) = \exp \left[- \int_0^t \lambda(t) \cdot \left[1 - F_S \left\{ R_0 \left(G(t) - \alpha \Delta T(t) \right) - D_n \frac{\Delta E}{E} \cdot \Delta T(t) \right\} \right] dt \right] \quad (14)$$

where α is taken to be 10×10^{-6} (approximate median for concrete).

Reduction in strength due to carbonation is captured in coefficient b in the degradation function. The IPCC report suggests an increase of 2 to 2.5 times in the carbon dioxide levels in 100 years and historically the levels of carbon dioxide have increased linearly. This study uses the lower projected estimate of a 100% linear increase in 100 years for carbon dioxide levels and the coefficient b correspondingly increases by the same amount. Similarly, the accelerated corrosion due to an increase in temperature affects c . Assuming that the rate of corrosion increases by 2% per °C from Pijanowski and Mahmud, 1969 and Qi et al, 2014, c changes by the same amount linearly with temperature, which is consistent with the exponential effect of temperature particularly at low temperatures with an increase of 2.65 °C in 100 years.

With the impact of the choice of parameters on the results, a sensitivity analysis of the calculated reliability or probability of failure to the choice of parameters for the degradation function can be performed similar to Equation (11), changing G to L or P_f . The analysis at $t = 40$ years results in the sensitivity indices of $\varphi_a = 7.47 \times 10^{-4}$, $\varphi_b = 1.78 \times 10^{-4}$, and $\varphi_c = 1.63 \times 10^{-3}$ for P_f . As these are sensitivity magnitudes, the results are the same for L . This shows the effect of changes in parameters on the failure probability results presented. The parameters b and c correspond to the climate-dependent parameters and the probability of failure P_f is more sensitive to c compared to b , which is consistent with the sensitivity analysis of the degradation function, G .

Accounting for these climate-dependent factors affecting the resistance, Figure (7-1) shows the effect of individual factors on structural reliability over time. These are compared with the probability of failure calculated without incorporation of increased degradation due to climate change, indicated as “natural” on the plot. The combined effect of all environmental factors, indicated as “net effect” on the plot, is also shown. The climate projections in the IPCC report are

for 100 years from 2000-2100. Therefore, the structural reliability plots are plotted for 85 years, until the year 2100.

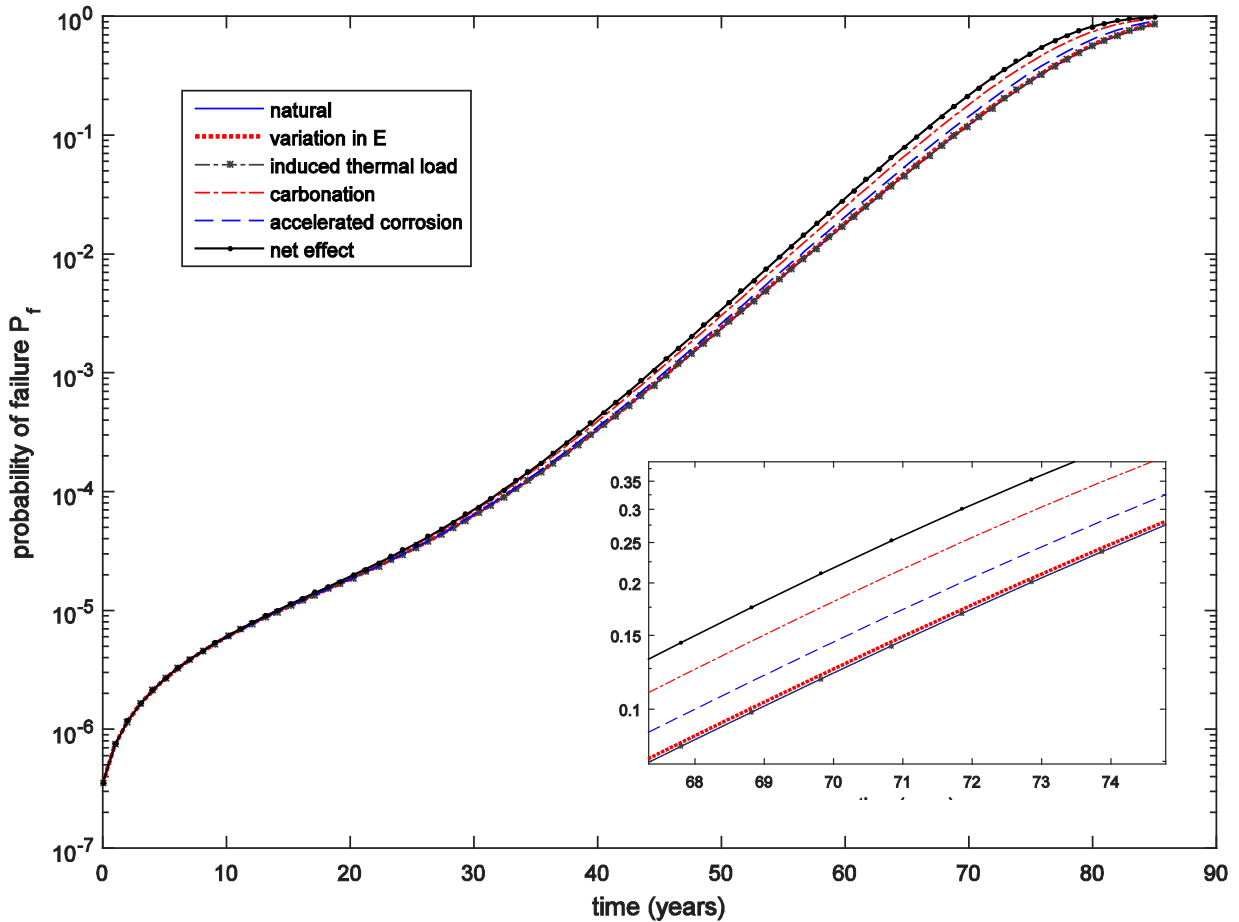


Figure 6-1 Probability of failure vs time, with changes in resistance due to environmental factors

From Figure (7-1), the effect of induced thermal loads is negligible compared to the probability of failure without the consideration of any climate effects. The difference in reliability is on the order of 0.6% between the two cases, resulting in overlapping lines on the plot. The effect of change in modulus of elasticity is slightly larger than for thermal loads, though also negligible in the considered time period. It shows that the scale of change in temperature does not cause significant changes in the modulus of elasticity or thermal loads of a concrete structure. Carbonation and

accelerated corrosion are found to have larger effects. The order of change depends on the fraction of degradation attributed to each factor. For the assumptions of this study, carbonation has the largest effect. As described previously, the fractional attribution to each degradation mechanism can be adjusted based on the type and location for any structure of interest. Looking at the net effect line in Figure (7-1), we see that the net probability of failure accounting for the climate change effects on resistance is nearly double that of the natural degradation line after 40 years, with a greater increase in probability of failure as time increases. The degradation of the structure is accelerated under climate projections through 2100, showing the importance of accounting for climate change in structural reliability assessment.

As discussed in the methodology section, the degradation for steel and wood can be similarly modeled using the same degradation function but ignoring the carbonation term. Figure (7-2) shows the change in reliability for steel and wood due to environmental-induced changes in material properties. Figure (7-2a) is the probability of failure of an example steel structure. It is generated by neglecting the carbonation term and attributing equal degradation weights of 50% each to fatigue and corrosion as both factors are dominant factors for the degradation of steel. Figure (7-2b) is similarly generated for wood. The dominant degradation mechanisms for wood are fatigue, biochemical attacks, and moisture-temperature effects. All of these factors have an effect on the mechanical properties of wood. Assigning equal weights to the four factors and attributing fatigue, biochemical attacks, and moisture to the linear term in the degradation function, 25% of the degradation is attributed to temperature. Hence, the exponential term accounts for a quarter of total degradation and the square-root term is neglected. As per Gerhards, 1982 [77], at lower temperatures of 0-50°C, a change of 10°C in environmental temperature decreases the strength parameters by 2-3% and the effect on the natural logarithm of the mechanical property is

directly related to a linear change in temperature. Therefore, the plot is generated using a change of 2% and the exponential relationship with temperature. It is also noted that while moisture content and temperature affect the properties of wood simultaneously, the effect of moisture is not considered separately because projection of moisture content levels is difficult and specific to time and region. It is also noted that the exponential term for wood correlates the strength property, which is modulus of elasticity in the studied case, to temperature. Therefore, the temperature term is sufficient and the fractional modulus of elasticity term in Equations (12-13) is not considered separately to avoid double counting the environmental effects on resistance.

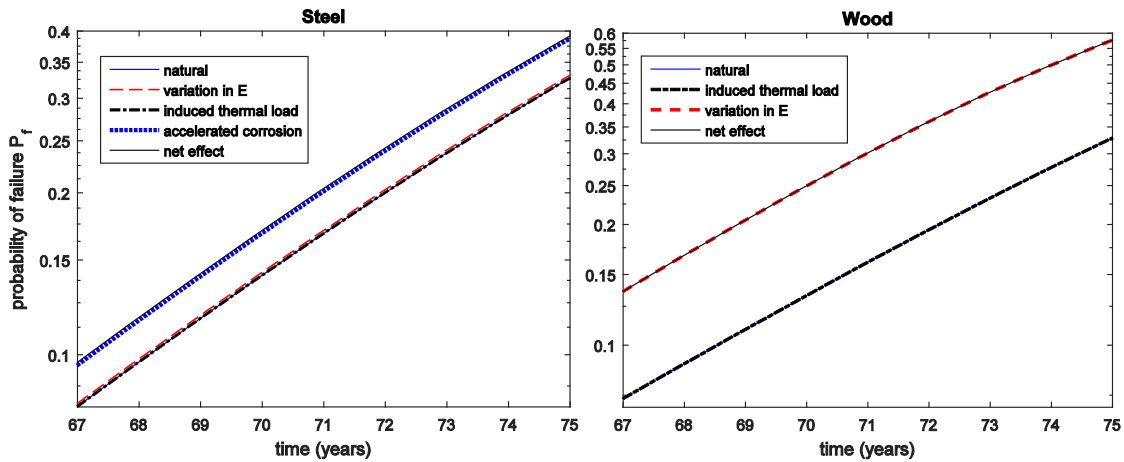


Figure 6-2 Probability of failure of example (a) steel and (b) wood structures with change in resistance due to environmental factors

From Figure (7-2a), despite equal weights for corrosion and fatigue in the degradation function, corrosion has the greatest effect on decreasing the reliability of the steel structure over time. Figure (7-2b) shows the increase in probability of failure for the wood structure due to variation in modulus of elasticity. The strength of a wood structure depends on the moisture content of the air. However, we are presenting a relative change in the reliability due to changes in environmental parameters over long time periods. It is difficult to quantify and project the changes in moisture

content over a long duration of time and therefore, its relative impact on reliability is not included. The effect of induced thermal loads is negligible in both cases.

Next, the authors study the effect of changes in the extremes of environmental loads. As previously discussed, the frequency of natural hazards and the intensity of the extremes of these events is expected to increase. The effects of extreme loads may not be directly proportional to the increase in intensity. Therefore, different load effect scenarios are considered, which will depend on the region, loading event, and structure. The IPCC provides projections of increases in maximum wind speed, precipitation extremes, and snow events. The projections also estimate an increase in the number of severe events. However, no clear consensus exists on a quantification of the increase in number of occurrences. Therefore, in this study, the authors assume that the mean rate of occurrence remains the same, while the intensity of extremes changes. It is noted that any resulting increase in probability of failure will thus be a conservative estimate of decreasing reliability. Further increases in failure probability are expected if increases in the mean rates of natural hazard event occurrences are included. The projections of change in number and intensity of events vary by site and hazard. Region-specific studies for particular hazards, such as hurricanes for the Eastern U.S., can be used to provide estimates of the impact of climate change on reliability for a structure located at a specific site under a specific hazard. The increase in the severity of environmental events depends on the region being studied. Here, however, rather than restricting the analysis to a specific region, the effect on reliability due to a 5%, 10%, and 15% increase in the intensity of extremes in 100 years is studied. The coefficient of variation is assumed to remain constant while the mean changes with time such that it increases by the given percentage in 100 years. Figure (7-3) shows the effect on reliability of changes in the intensity of extremes of significant environmental load events over time. For comparison, reliability without (indicated as “natural at

existing environmental load”) and with (indicated as “net at existing environmental load”) decreased resistance due to climate change factors are shown.

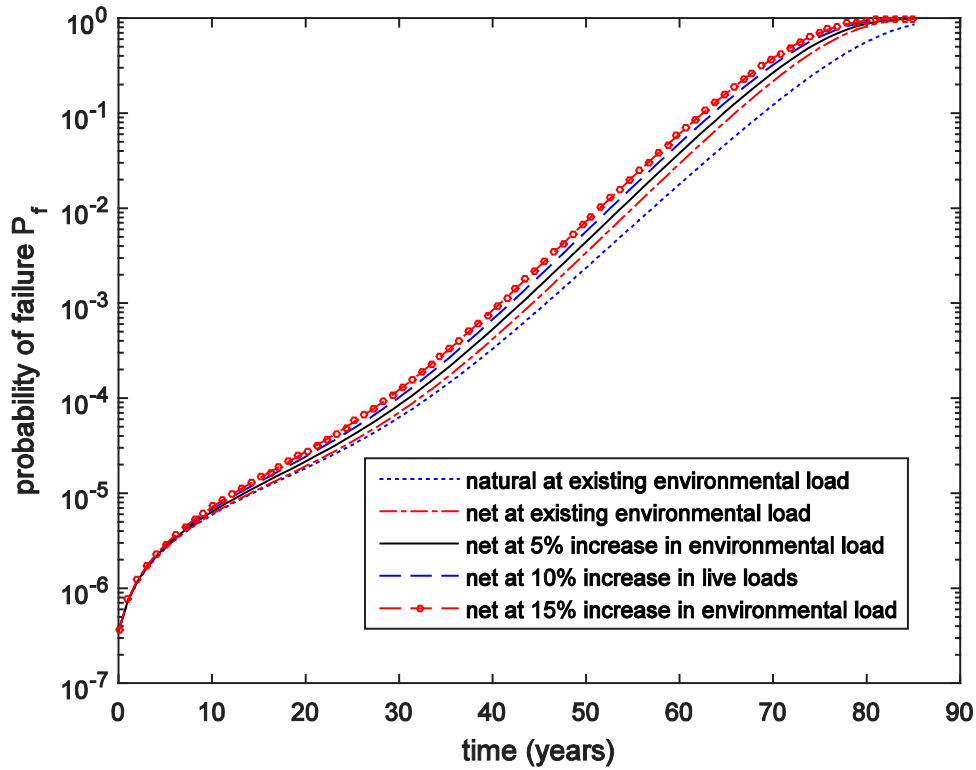


Figure 6-3 Probability of failure vs time, with increase in the extremes of loads, corresponding to an increase of 5%, 10%, and 15% increase in the mean in 100 years

Figure (7-3) shows the impact of an increase in the mean intensities of environmental load events on the reliability of structures. The probability of failure is increased at each instant of time. The failure probability increases by as large as 3.5 times compared to the original curve.

Finally, with increasing natural hazards, the authors study the variation in reliability in the presence of two different environmental load events. The first load events are modeled with the same characteristics as above. The second process models more frequent, lower intensity events, with an assumed rate of occurrence of 10/year, mean $\mu_{S2} = 0.4L_n$, coefficient of variation 0.4, and following a Type 1 distribution. The mean for the first load event increases linearly in time

corresponding to the specified increase in intensity in 100 years, while the increase in the mean intensity of the extreme of the second event is assumed to be exponential to vary the fraction of change corresponding to each event. The probability of occurrence of the extremes of both loads simultaneously is assumed to be negligibly small with independence between the two load events, so that the two Poisson processes can be merged directly. Figure (7-4) shows the reliability over time under the action of two load events.

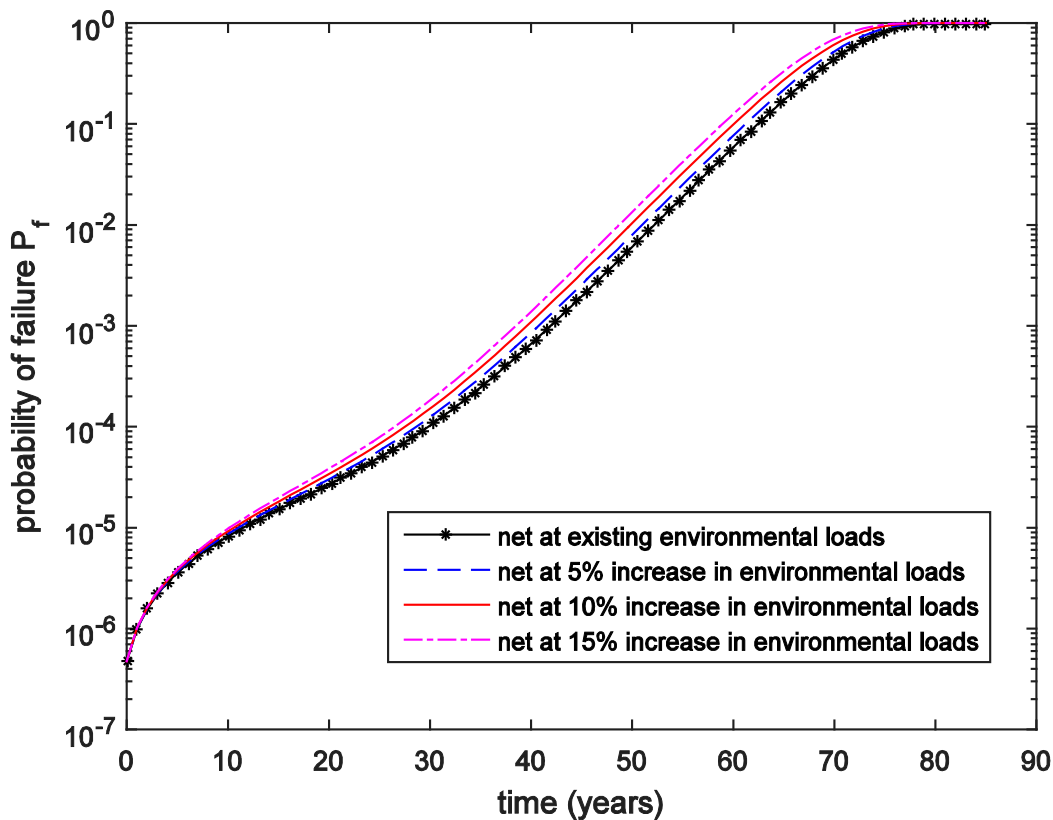


Figure 6-4 Probability of failure vs time, where two different significant load events act on the structure

In Figure (7-4), the lowest probability of failure curve provides the failure probability of the structure when the mean intensity of the extremes of the two environmental loads remains constant over time but the resistance of the structure changes with the varying environmental conditions. The remaining lines show the reliability for the corresponding percentage changes in the mean

intensities in 100 years. From Figure (7-4), the reliability decreases with the increase in load intensities. There is an increase in probability of failure at each time step, with the failure probability increasing by as large as 2.5 times compared to the case without accounting for increased environmental loads.

6.5 Conclusion

This study focuses on the need to incorporate climate change in the assessment of long-term structural reliability. Generally, the service life of civil infrastructure spans across decades and in many cases, structures are used past their design service lives. When looking over these longer time horizons, it becomes important to account for changes in environmental patterns to accurately assess the future reliability of a structure. The authors use global mean projections for estimated changes in environmental factors to investigate their impact on structural reliability. This study shows the significant effect of changing climate patterns on the long-term performance of civil infrastructure.

Climate change affects both the resistance of a structure and the loadings on the structure. The resistance is most affected by carbonation and accelerated corrosion due to an increase in temperature. While a general structure with assumed structural parameters is used in the application of this study, given the attribution of different degradation mechanisms to different factors in the resistance function, the resistance of coastal structures would likely be affected even more compared to land structures. The authors also show the importance of accounting for changes in the extremes of live load events in reliability studies. The effect on reliability of increases in event intensity depending on the type of hazard and projected hazard levels is significant. With the combined effect of climate change on the resistance and loading, the probability of failure based

on global means increases by 2-4 times. The increase may be even higher depending on the type and location of a structure. It should also be noted that the projections and impacts are estimated at lower values. Therefore, the estimates of increases in failure probability are conservative.

While global means are used in this study, we can use the extensive regional projection data available to assess the long-term reliability of a particular structure. It may be useful to account for extended hazard models based on expected service life and usage of the structure instead of code-specified hazard intensities. A general methodology is presented here. Location-specific assessment should account for the projected increase in the extremes of the relevant natural hazards in the area, including hurricane and non-hurricane winds, precipitation, snow, and wave-heights. Structures under more than one type of dominant hazard would have a multiplicative effect on the reliability and would be more prone to damage and failure. The results shown are therefore conservative estimates of the impact of climate change on structural reliability. Based on the type and usage of a structure, other modes of degradation can be included which may be affected by the variations in environmental parameters due to climate change.

CHAPTER 7. LONG-TERM RELIABILITY: A STOCHASTIC MODEL FOR LONG-TERM STRUCTURAL DEGRADATION

7.1 Introduction

The quantification and estimation of structural reliability enables us to forecast risk over the lifetime of a structure. With a growing focus on increasing the resilience of structures to future loading events, it becomes even more important to be able to accurately quantify the structural reliability at any instance of time. Such information can be used to predict structural behavior under risk conditions, understand long-term behavior and levels of serviceability at a given time, and optimize repairs and rehabilitation to increase structural performance and resilience over the service life. Different stochastic models exist to estimate structural reliability. Most are based on calculating a probability of failure, defined as the probability of structural loading exceeding structural resistance. The structural resistance is modeled in terms of the degradation in structural strength over time with respect to the initial strength. Therefore, an accurate estimator of the degradation is essential for improved estimates of reliability. Such a model should reflect the long-term structural behavior and be adaptive to new information at any time during the structural lifetime. The complexity of the problem increases because as structures age, they are subject to numerous factors degrading their strength. Due to the number of degradation modes, their effects, external variables, the long time duration of analysis, and many sources of uncertainties, estimating structural degradation, and correspondingly structural strength, can be difficult.

In this paper, a new model for structural degradation is proposed. Compared to previous studies, it is based on the mechanical properties of individual degradation modes with an emphasis on

matching structural degradation mechanisms and physical correctness. The proposed model is a random sum of a random number of degradation modes, where individual modes are estimated as stochastic functions based on their mechanical properties. Some modes are modeled as Poisson arrival processes to account for those modes that start acting after a given time compared to those that begin at initial construction and affect the structure throughout its lifetime. Terms that capture the effect of a degradation mode on the rate of another are also included. In the process of deriving the final function, each individual degradation mode is multiplied by a corresponding weight to quantify its effect on the total degradation. The weights are chosen to be random to form the function as the random sum of degradation modes. The final form of the proposed model is a function of only two parameters, with the derivations shown in this paper. The parameters can be estimated from any available structural inspection data. The degradation model is continuous and can be directly used to calculate structural reliability at any point in time. It can also be updated in time with structural inspection data as it is available. The proposed degradation model does not provide information about the particular type or amount of damage of a structure at an instant of time. Rather, it gives a global estimate of the change in structural strength over time with the purpose of facilitating more accurate long-term reliability estimates. The results show the proposed model to be more accurate in estimating the average change in structural strength over a long duration of time than existing models used in reliability calculations.

The rest of the paper is organized as follows. The following section provides background on structural degradation modeling and describes the proposed degradation function in the context of previous work. Next is the detailed methodology, which explains the derivation of the proposed function. Estimation of the model parameters is also described. The use of the proposed function is then illustrated with data from a monitored pedestrian bridge. The data is used to estimate the

model parameters and results from the proposed model are compared with those from other widely used degradation functions. Finally, the paper concludes with a discussion of the characteristics of the proposed function and its use for future applications.

7.2 Background

A number of studies assess structural reliability under different conditions [16], [74], [76], and [78]. In these studies, while structural degradation is modeled stochastically, simple functions are used to calculate structural reliability. At a basic level, single functions, such as exponential or polynomial functions [16] and [78], provide a way to estimate individual degradation modes. These functions, however, fail to capture total structural degradation, which is influenced by multiple and varying modes of degradation at any one time. The rates and impacts of individual degradation modes also vary in time. Therefore, previous studies use distributions to model degradation to represent a combination of several degradation modes. These estimators can be more general, for example, the gamma distribution [4] as a sum of individual exponential functions. However, such models do not account for changing rates of individual modes, the effect of modes on each other, and modes that do not affect a structure at all times. These purely stochastic models do not reflect the structural properties; therefore, they are not adaptable to the structural health monitoring data collected at various stages throughout the lifetime of the structure. Continuous time Markov chains [79-80] have also been used to predict degradation. This approach captures the time evolution of structural degradation and is consistent with the degradation at a particular time being a function of the previous state of the structure. However, such a model requires estimation of transition probabilities and rates. These values are estimated based on detailed knowledge about structural parameters and states, which in many cases is not

available. These models can be updated based on the availability of different varieties of health monitoring data.

We propose a new stochastic model for degradation, which is based on the aggregation of different degradation modes for a structure. The model is more closely based on the physical mechanisms of degradation than previous models by capturing individual modes and combining multiple effects. It is more adaptable to changes in rates and modes of degradation over time, and is a function of only two parameters. The model and its parameters can be updated with the availability of data over time. This model does not provide information about the mechanical degradation or localized damage to the structure at a specific instance of time. However, it attempts to accurately estimate the overall effect of material degradation on the average mechanical strength over time. The quantification of degradation is strictly for the purpose of reliability calculations in long-term. It provides an estimate for the relative strength of the structure under loading.

The following studies inform the proposed degradation model. The modeling of time-dependent structural reliability under non-stationary loads in [16] provides a comparison of different stochastic models for structural degradation. The study formulates a time-dependent resistance function, subtracts the dead loads to obtain the resulting available resistance, and calculates the probability of non-stationary loads exceeding the resistance at any time instant. The structural resistance is normalized relative to the initial structural strength and polynomial, exponential, and gamma models for long-term structural degradation are used. These models often are good estimators for single degradation modes. However, they do not capture the entire structural degradation process, which includes the effects of multiple modes and interactions between modes. In addition, these models can be physically incorrect. For example, they do not satisfy constraints

of degradation, including having values representing no degradation at the initial time step and complete degradation at the final time step.

The degradation model in [78] is proposed to account for the effects of multiple degradation modes. By separating out terms of different forms, the authors are able to investigate the impacts of changing environmental variables including those due to climate change on varying degradation modes. However, the model does not yet match expected properties of the degradation function as the proposed model in this paper seeks to do.

The functions for degradation described thus far provide analytical assessments of degradation. Other studies have modeled degradation based on experimental data [81] or numerical methods combined with fracture analysis to model degradation at the material level [82]. These studies contribute to the understanding of the mechanics of structural degradation. However, the available data for a given structure is often limited. Therefore, our model is derived as a simple stochastic function, composed of two parameters, which is adaptable over time based on availability of data.

In seeking to account for multiple degradation modes in the proposed model, the varying effects of each mode on a structural component are included. Every mode for material deterioration impacts the mechanical properties and overall relative strength of the structure. Here, relative strength indicates the current mechanical strength of the structure with respect to the initial strength. A number of studies look to understand the differing rates and appropriate models for individual modes of degradation. A summary of these are given in Tables (8-1:8-3), which describe some of the dominant degradation modes for concrete, steel, and wood structures. The modes, their effects, the estimator functions used to quantify them over time, and representative corresponding references are provided. Degradation rates differ based on the effect of a particular mode on the

mechanical properties of the structural component. Integrating the estimated degradation rate results in an approximate estimator for that particular mode. For example, a constant rate of degradation for a particular mode when integrated results in a linear degradation estimator. In Tables (8-2:8-3), E indicates the modulus of elasticity.

Table 7-1 Selected degradation modes for concrete, their effects, and estimator models

| Concrete degradation modes | Effects | Approximate estimator |
|-----------------------------------|--|-------------------------------|
| Tensile loading | Cracks and fatigue | Exponential [83] |
| Compression loading | Fatigue | Linear [84] |
| Corrosion | Reduced bond and flexural strength, cracks | Exponential [85] |
| Carbonation | Reduced compressive strength, increased corrosion rate | Polynomial (square-root) [86] |
| Chloride attack | Increased corrosion rate | Shifted exponential [87] |

| | | |
|---------------------------|---|--|
| Sulfate attack | Cracking, expansion, reduced bond | Linear [88] |
| Alkali-aggregate reaction | Cracking, spalling, or expansion | Linear [89] |
| Acid attacks | Deterioration and debonding | Exponential [90] |
| Fire/heat | Reduced strength only at elevated temperature | Function of modulus of elasticity [91] |
| Abrasion/erosion | Reduced strength and increased corrosion | Exponential [92] |
| Freeze-thaw cycles | Reduced compressive and shear strength | Linear [93] |

Table 7-2 Selected degradation modes for steel, their effects, and estimator models

| Steel degradation modes | Effects | Approximate estimator |
|--------------------------------|----------------|------------------------------|
|--------------------------------|----------------|------------------------------|

| | | |
|----------------------|--|--------------------------------|
| Corrosion | Reduced strength and load bearing area | Exponential [94] |
| Fatigue | Reduced E | Polynomial [95] |
| Heat and temperature | Reduced E and increased thermal loads | Pre-defined function of E [96] |

Table 7-3 Selected degradation modes for wood, their effects, and estimator models

| Wood degradation modes | Effects | Approximate estimator |
|-------------------------------|--|--------------------------------|
| Natural decay | Reduced strength and load bearing area | Exponential [97] |
| Fatigue | Reduced E and strength | Pre-defined function of E [98] |

| | | |
|-----------------|--|------------------|
| Termite attacks | Reduced strength and load bearing area | Exponential [99] |
|-----------------|--|------------------|

In Tables (8-1:8-3), the rates for most degradation modes are estimated to be exponential or constant. Therefore, most individual modes can be estimated as exponential or linear functions. In rare cases, modes are estimated to have a linearly increasing rate and therefore result in a polynomial function of degree two, for example, the effect of fatigue on steel. Carbonation reduces the strength of reinforced concrete and leads to the corrosion of steel reinforcement. Studies on the effect of carbonation on the mechanical properties of concrete found the depth of carbonation to be directly proportional to the square root of the concentration of atmospheric carbon dioxide [70]. The carbonation depth is directly proportional to the rate of corrosion and strength, while the concentration of carbon dioxide is approximately linearly increasing in time. Hence, a polynomial term of degree 0.5 is also added to account for the effect of carbonation with time.

As any number of degradation modes can be acting on a structure at a given time, we develop the proposed model as the sum of all possible degradation modes. In its final form, the proposed model is a function of two different parameters, with the model adjusting for the weightage of the individual degradation modes depending on the estimated values of the parameters. For any given structure, based on its characteristics including material, age, and location, some modes will be dominant while others will not act. The parameters of our model estimated from structural health monitoring data account for the dominant modes of degradation, the individual rates, and the number of modes acting.

7.3 Methodology

7.3.1 Derivation of proposed model

The degradation for this study is defined as the decrease in the relative strength under loading. The long-term reliability can be estimated in terms of probability of failure defined as the probability of resistance being lower than the loading. Therefore, degradation in terms of relative strength provides an estimate of resistance for the reliability calculations. It is an estimated quantification of the net decrease in the global strength over a long duration of time. We define $\theta(t)$ as the degradation function such that the resistance of a structural component decreases with time and $R(t) = R_0(1 - \theta(t))$, where $R(t)$ is the resistance at time t and R_0 is the initial resistance. Based on this, the degradation function must have the following properties:

- $\theta(0) = 0$
- $\theta(\infty) = 1$
- $\theta(t)$ is monotonically increasing over time except for external interventions such as repairs or retrofits

The degradation function is formulated as a sum of various degradation modes, with weights indicating the respective contributions of each mode to overall degradation, as

$$0 \leq \theta(t) = \sum_{i=1}^{N(t)} w_i F_i(t) \leq 1 \quad (1)$$

$$\sum_{i=1}^{N(t)} w_i = 1 \quad (2)$$

where $N(t)$ is the number of degradation modes acting at time t , and $F_i(t)$ is the estimator model and w_i the corresponding weight for the i^{th} degradation mode. Each individual degradation mode can be modeled as an estimator function. However, each mode may not act independently of all others. An individual degradation mode can be influenced by the impact of another mode. For example, in reinforced concrete structures, carbonation or abrasion can increase the rate of corrosion. Therefore, to account for these effects, we model the estimator for the i^{th} mode as

$$F_i(t) = f_i(t) + f_{ji}(t) \quad (3)$$

where $f_i(t)$ is the estimator function for the individual i^{th} mode and $f_{ji}(t)$ is the effect of the j^{th} mode on the i^{th} mode. $f_{ji}(t)$ is assumed to follow the same form as $f_i(t)$, but its arrival is the same as the arrival of the j^{th} mode. Thus, we model the influence of one mode on the rate of another while not changing the way in which the original mode affects a structural component.

Most degradation modes can be modeled with either exponential or constant rates and therefore exponential or linear functions as shown in Tables 1-3. Assuming that the numbers of degradation modes following polynomial functions with degrees 0.5 or 2 are significantly lower compared to either linear or exponential modes, we estimate them with single terms modeling a small effect on the overall degradation. The degradation function then becomes

$$\theta(t) = \sum_{i=1}^{N_e(t)} w_{ei} F_{ei}(t) + \sum_{i=1}^{N_l(t)} w_{li} F_{li}(t) + w_s a_s t^2 + w_r a_r \sqrt{t} \quad (4)$$

where the subscript e denotes exponential, l linear, s square, and r square-root. a_s and a_r are the coefficients for the square and square-root terms respectively. For the linear term,

$$F_{li}(t) = a_i(t - t_i) + a_{ji}(t - t_j) \quad (5)$$

where t_i and t_j are the arrival times for modes i and j , respectively. a_i is the linear coefficient for mode i and a_{ji} is the linear coefficient for the effect of mode j on mode i . We consider modes that begin at time of initial construction and act through the lifetime of the structure, and others that begin at a later time. Therefore, we assume that some degradation modes start acting on the structure at time $t = 0$, while the others have a time of arrival. Without loss of generality, we can assume that arrival times $t_1 < t_2 < \dots$. The linear functions term then becomes

$$\begin{aligned} \sum_{i=1}^{N_l(t)} w_{li} F_{li}(t) &= w_a a_a t + w_b a_b t + w_c a_c t + \dots \\ &+ \begin{cases} 0 & t < t_1 \\ w_d a_d (t - t_1) & t > t_1 \end{cases} \\ &+ \begin{cases} 0 & t < t_2 \\ w_e a_e (t - t_2) & t > t_2 \end{cases} + \dots \end{aligned} \quad (6)$$

where terms a, b, c, \dots denote modes acting starting at time $t = 0$, and terms d, e, \dots denote modes starting at a later time. Assuming the arrival times of the later modes to be Poisson with a fixed rate, Equation (7) represents the sum of linear terms in a compact form.

$$\sum_{i=1}^{N_l(t)} w_{li} F_{li}(t) = \sum_{i=1}^n P(n = k) \left[t \sum_{i=1}^k a_i - \sum_{i=1}^k a_i t_i \right] + At \quad (7)$$

where A is the coefficient for all the linear terms starting at $t = 0$ and n is the number of linear terms with a non-zero arrival time. Similarly, we expand the exponential terms. The number of unknown parameters decreases in all cases after expanding and adding similar terms. λ_i indicates the exponential rate of the i^{th} exponential mode.

$$F_{ei}(t) = (1 - e^{-\lambda_i(t-t_i)}) + (1 - e^{-\lambda_i(t-t_j)}) \quad (8)$$

$$\begin{aligned} \sum_{i=1}^{N_e(t)} w_{ei} F_{ei}(t) &= \sum_{i=1}^{N_e(t)} w_i + \sum_{i=1}^n P(n=k) \sum_{i=1}^k w_i + w_a e^{-\lambda_a t} + w_b e^{-\lambda_b t} + w_c e^{-\lambda_c t} \dots \\ &+ \begin{cases} 0 & t < t_1 \\ w_a e^{-\lambda_a(t-t_1)} & t > t_1 \end{cases} \\ &+ \begin{cases} 0 & t < t_2 \\ w_e e^{-\lambda_e(t-t_2)} & t > t_2 \end{cases} + \dots \end{aligned} \quad (9)$$

n is the number of exponential terms with a non-zero arrival time and $k \in [1, n]$ such that every possible number of terms is considered. The expression for the exponential terms becomes

$$\sum_{i=1}^{N_e(t)} w_{ei} F_{ei}(t) = c + \sum_{i=1}^{N_e(t)-n} w_i e^{-\lambda_i t} + \sum_{i=1}^n P(n=k) \sum_{i=1}^n w_i e^{-\lambda_i t} e^{\lambda_i t_i} \quad (10)$$

where $c < 1$. We solve this by considering each of the three terms on the right-hand side of Equation (10) as the probability density of a convolution of exponentially distributed random variables with different parameters as suggested in [99]. First, we multiply and divide each term by its respective λ_i . The probability density of a convolution of exponential distributions with different parameters is given by

$$S_n(t) = \sum_{i=1}^n \frac{\lambda_1 \dots \lambda_n}{\prod_{\substack{j=1 \\ j \neq i}}^n (\lambda_j - \lambda_i)} e^{-\lambda_i t} \quad (11)$$

Now, we assume that some of the degradation modes are more dominant than others in affecting the structure such that, in most cases, $(\lambda_j - \lambda_i) \sim \lambda_j$. This is indicating that we are approximating the rate of total degradation of the structure as being dictated by a smaller number of dominant

modes while a larger number of other modes have a relatively smaller effect. Therefore, the rate λ_j for a subset of dominant exponential modes j is much higher than that of other modes. With this assumption, we use the convolutions for each term to obtain the exponential terms, and then add the estimations for the linear, square, and square-root terms.

We then use the Taylor expansion of each term to simplify and aggregate similar terms, expanding the four terms and merging those of the same order. The higher order terms for the square and square-root terms are ignored because of the assumption of their lower relative impact on the extent of degradation. This assumption is based on the estimators for the individual degradation modes presented in the previous section, where most of the modes are estimated as linear or exponential. Only one mode has an estimator with a polynomial square-root term. Similarly, only one mode is polynomial with a square term. Therefore, the relative impact of these modes on the overall degradation is lower compared to the exponential or linear terms. These two terms are assumed to not have an arrival time. It is assumed that they act throughout the lifetime of the structure. These terms correspond to carbonation and fatigue, which generally do not require an initiation time. Therefore, these terms do not have a Poisson arrival and are simply added as polynomials in the methodology. The weights multiply with the coefficients of expanded terms to give new coefficients for each term, similar to the computations for the linear terms. Therefore, we are left with polynomial terms with one coefficient each through the Taylor series. Some terms of the Taylor expansion directly converge into an exponential function. Therefore, the Taylor expansion is separated into two groups: the first group that directly converges into an exponential function and the second with convergence estimated as in [101]. The final form for the degradation function is the following:

$$\theta(t) = 1 - e^{-\lambda t} + \frac{\log(1+(\lambda t)^{\frac{1}{n}})}{n!} e^{-\frac{\lambda}{n}t} \quad (12)$$

This function has two unknown parameters n and λ . n can be viewed as the number of degradation modes and λ the Poisson rate of arrival of later degradation modes. It is important to note that these parameters are estimators for the number of degradation modes and the rate and they do not represent the actual physical parameters at a specific time. Therefore, the parameter n is not constrained to natural numbers. As an estimator, it is only constrained to have positive real values. These parameters are adaptable to new information and should be updated if data is available. This model fits the expected fundamental properties of degradation as discussed in terms of bounds and limits. The function is adaptable to change in structural properties over time based on the change in the two parameters. As there are only two parameters that need to be estimated, the function provides a way to estimate long-term structural degradation with limited data.

7.3.2 *Parameter estimation*

To estimate the parameters of the model, we need at least two different observations of structural monitoring data at different times. The model represents the relative change in the structural strength. Therefore, we need at least two observations for a parameter corresponding to structural strength. If a structural system is instrumented using, for example, accelerometers and LVDTs placed on the structure, then we can estimate the structural parameters as described in [102-103]. Such an instrumented system will measure input accelerations and displacement histories over time. By using an unscented Kalman filter approximation on the data, the mass, damping, and stiffness parameters corresponding to every degree of freedom of the structure can be estimated. Assuming that the geometric properties of the structure remain the same, we can estimate

degradation by using the fractional change in stiffness over time. In such a scenario, the stiffness matrix is used to estimate the parameters of the degradation function.

In other cases, systems instrumented with, for example, strain gauges also provide enough information to estimate the degradation model parameters. The strain gauges will measure the strain at a particular instance of time. Assuming that the geometric properties are constant, the mechanical strains will be directly proportional to the modulus of elasticity of the system. Mechanical strains may be affected by other processes, e.g., creep in concrete. However, based on data availability, changes in modulus of strength provide an estimation for the changes in the relative strength of the structure over time. In such cases, modulus of elasticity will be an estimate for the long-term reduction in strength. Assuming degradation to be the fractional decrease in the modulus of elasticity of the structure over time, we estimate the parameters of the model by

$$\varepsilon_m(t) = \frac{k}{E} \quad (13)$$

$$\theta(t) = \frac{E(0) - E(t)}{E(0)} \quad (14)$$

$$\theta(t) = \frac{\frac{1}{\varepsilon_m(0)} - \frac{1}{\varepsilon_m(t)}}{\frac{1}{\varepsilon_m(0)}} \quad (15)$$

where ε_m represents mechanical strains, E modulus of elasticity, and k a constant assuming the geometric properties of the structural component do not change during the time of data collection. It is also assumed that different data points are collected under similar loading scenarios. However, as the strains are a function of the loading applied on the structure, using data from multiple strain measurements increases the confidence in our estimates of the parameters of the model.

7.4 Application on data

To illustrate use of the proposed degradation model, we apply it to data from the Streicker Bridge, a pedestrian bridge located on the Princeton University campus. The available data are measurements of strain, prestress losses, and temperature collected continuously over three years. The data is collected at the mid-span of the bridge. The strain and temperature data is collected every five to 15 minutes, while the prestress data is collected at varying times over the three-year period. Figure (8-1) shows the strain and temperature data collected over the first three years. The prestressing force over the three years is shown in Figure (8-2).

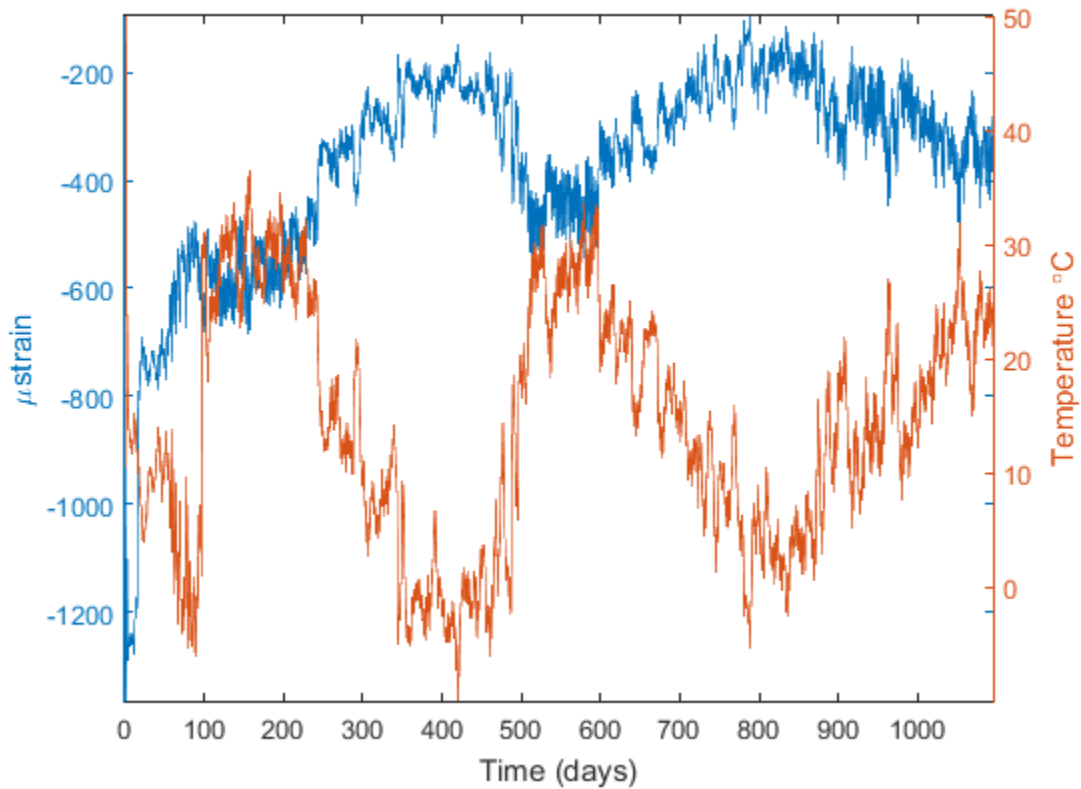


Figure 7-1 Data for strain (left axis) and temperature (right axis) for three years

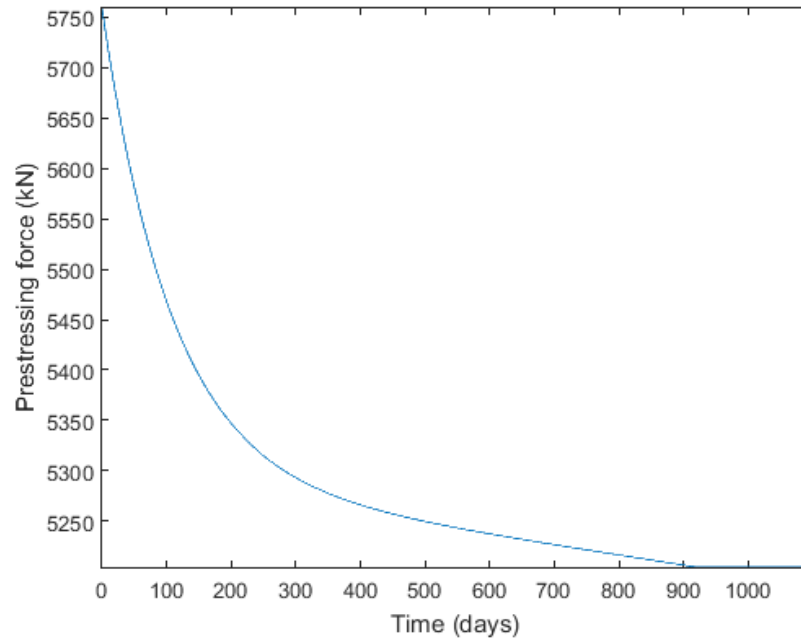


Figure 7-2 Prestressing force over time

To evaluate performance of the model, we divide the data into two sets. The first two years of data is used as a training set to estimate the parameters of the model. The data from the third year is used as the testing set. This separation of the data enables us to test the generalizability of the model and assess the accuracy of the model on previously unseen data. As the data is collected over small durations of time, this separation helps us with the assumption that the loading is on average constant. It also helps in reducing the effect of creep in the analysis when the duration between two adjacent observations is small because we have not quantified the effect of creep based on available data. We compare the performance of our proposed model on the testing dataset with results from widely used exponential, gamma, and linear regression models.

As the data is from a pedestrian bridge and it is collected over three years, we assume that the loading remains on average constant. We recognize that as the objective is to model long-term degradation, longer time periods of analysis may be desired. The model presented is general and

can be applied to any dataset. Here, we focus our analysis on the period when continuous monitoring data is available. The total strain measured for the bridge will be a sum of the thermal strain and the mechanical strain. We assume that the mechanical strain directly relates to the degradation. The total strain ε is given as

$$\varepsilon = \varepsilon_{thermal} + \varepsilon_{mechanical} + \varepsilon_{prestress} \quad (16)$$

and the thermal strain can be calculated as

$$\varepsilon_{thermal} = \alpha(T - T_{ref}) \quad (17)$$

where α is coefficient of thermal expansion, T is temperature at time under consideration, and T_{ref} is the reference temperature. Hence, the total strain at time t in this case is given as

$$\varepsilon(t) = \alpha\Delta T + \frac{k}{E(t)} + \frac{\Delta P}{E(t)} \quad (18)$$

where ΔP is the prestress loss until time t . The strain at time 0 will be given as

$$\varepsilon(0) = \alpha\Delta T + \frac{k}{E(0)} \quad (19)$$

Assuming the loading is on average constant and there is no change in the geometric properties of the structure, we use equation (14) to estimate $\theta(t)$. We then use adjacent pairwise values of $\theta(t)$ to calculate n and λ . The final values of the two parameters are the average values across the training dataset.

7.5 Results

The strain and temperature data shown in Figure (8-1) includes the testing as well as training data. The measured strains are total strains. We are interested in estimating the overall change in the structural strength under loading. The thermal strains are localized and fluctuate depending on the temperature. The change in prestressing force also causes the change in strength but our focus is on the overall effect of the degradation in the material on the strength. Therefore, we use the temperature data along with prestress data to subtract the thermal strains and strains due to prestress loss to obtain the values of mechanical strains. The mechanical strains are used to estimate modulus of elasticity, which is a representative for the change in the relative strength of the structure. The value of the thermal coefficient is assumed to be $\alpha = 10 \times 10^{-6}$. The reference temperature is $T_{ref} = 20^{\circ}\text{C}$, which is close to the average of the temperature measurements in the training set. We estimate the model parameters using the value of degradation at each time step. Each time step is taken to represent a single day. We then calculate the average of the values from the estimates at each time step to obtain the value for each parameter. The final estimated degradation model parameters are $n = 3.4$ and $\lambda = 0.07$. We then use the testing data from the third year to calculate the value of degradation from the proposed model using Equations (14) and (18).

To assess performance of the proposed degradation model, we compare the result with that from traditional exponential and gamma models, and also a basic linear regression model minimizing error between the predicted and observed datapoints. The parameter values are calculated for each of these comparison models based on the training set data from the first two years. For each model, the parameters are estimated pairwise for adjacent datapoints and the average over all points used

as the corresponding model parameter. After obtaining the values of the parameters, we apply them to the testing data to evaluate performance. In Figure (8-3), we plot the resulting estimates of the third-year degradation from the proposed model and the three comparison models based on the parameters estimated using the training data. We compare all four models with the measured degradation at each time step, shown as open circles in Figure (8-3). Every circle represents the average degradation for a single day. To evaluate the performance of the varying models across longer structural lifetimes, Figure (8-4) shows the results of the four models for their estimates of the long-term structural degradation over 100 years. The calculated degradation values use the parameters estimated from the training data of the first two years evaluated over 100 years.

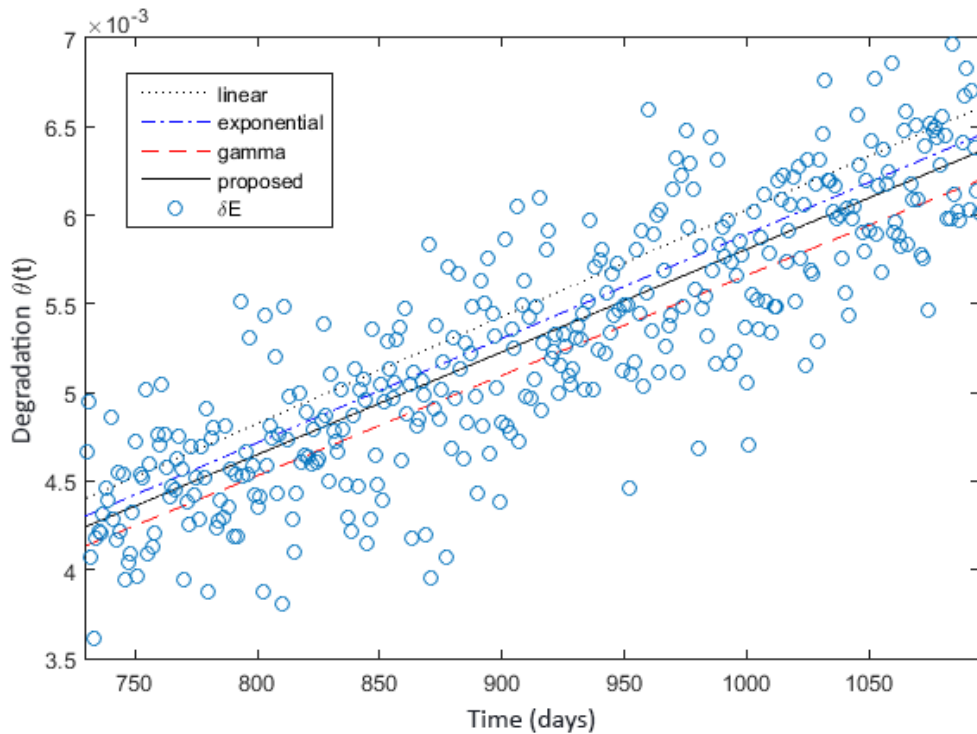


Figure 7-3 Results from varying degradation models for third-year testing data

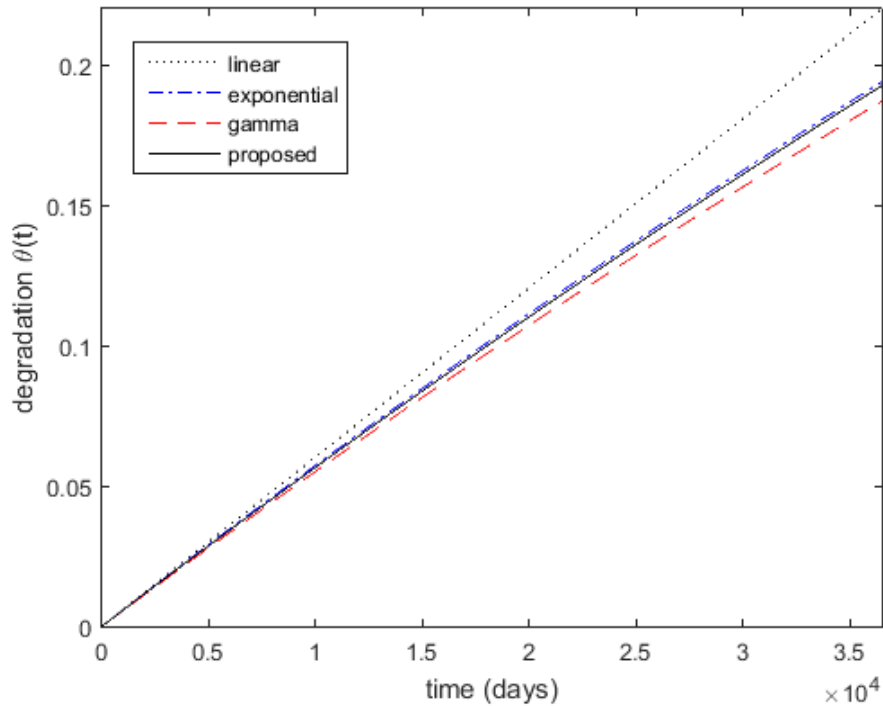


Figure 7-4 Total degradation curves over 100 years for varying models

From Figure (8-3), the proposed degradation model outperforms the other models in terms of accuracy. The root mean square error (RMSE) for the proposed model is 5.17%, while it is 10.98% for linear regression, 9.16% for exponential, and 7.44% for gamma models. The RMSE is calculated as the root mean square of the difference between the measured value and the estimated value of the degradation at every time step in the testing dataset. The RMSE will increase for assessments over longer structural lifetimes, particularly for the unbounded linear model, as seen in Figure (8-4).

Compared to the exponential and gamma models, the proposed model has several advantages. First, it is more consistent with the mechanics of degradation, accounting for the varying rates of degradation and effects across modes. Second, it satisfies the necessary boundary conditions for a degradation model. Finally, it is more adaptable to changes, both in the rate of degradation over

time as a structure ages or environmental parameters change, and in the structural parameters through any repairs or retrofits. For instance, if the dominant degradation mode changes and the form of the dominant term changes, then the gamma or exponential models will not be able to account for the new term and will be more prone to error. For the effects of varying structural parameters, the parameters of the proposed model will adjust accordingly based on structural monitoring readings. While the model parameters for exponential and gamma functions can similarly be updated, if the dominant degradation mode for the structure changes to a mode which cannot be captured using these two functions, then there will be errors in the estimation even after the updated parameters. In terms of computation, the proposed model is equally computationally efficient compared to other models. The computation time is negligible, taking 0.8s for the full calculation over 100 years on a personal computer. Any updates to the model parameters and long-term degradation estimates based on collected structural inspection data will take a similar time.

7.6 Conclusions

In this study, we propose a new stochastic model for modeling structural degradation. The model is formulated as a random sum of a random number of degradation modes acting on a structure at a particular time. This model provides an estimate for a change in relative structural strength over time without informing about the local material deterioration at a specific instant of time. This model is important for accurate estimations of structural reliability over the lifetime of the structure. We estimate the models for individual modes based on their mechanical properties. The resulting proposed model requires estimation of only two parameters. We derive the model, analyze its properties, and discuss methods for estimating the parameters of the model. We apply the proposed model to collected structural monitoring data, estimating the model parameters based on training data and evaluating it against a test set. The model is shown to perform better than

current models that are widely used to estimate degradation in reliability calculations. In addition to this improved performance, the proposed model is based on the varied physical mechanisms of degradation, is flexible to account for degradation modes of varying rates and arrival times over the lifetime of the structure, and matches expected properties of degradation. The model can be readily incorporated into stochastic reliability calculations and to estimate future structural resilience against stationary or non-stationary loads. As structures age and the useful life of structures around the world increases, the proposed function provides a way to better estimate degradation and corresponding reliability over longer structural lifetimes.

CHAPTER 8. LONG-TERM RELIABILITY: ESTIMATION OF RELIABILITY, QUANTIFICATION OF RESILIENCE, AND DYNAMIC RESOURCE ALLOCATION FOR REPAIR AND MAINTENANCE

8.1 Introduction

Civil engineering structures and infrastructure components are designed for tens to hundreds of years of expected service life. A structure needs repairs and maintenance over time for it to provide an expected level of service over long durations of time. Structural reliability based methods help us in projecting the structural behavior over time under regular loading and natural or man-made shock events. These methods can be used for the modeling the extent and cost of structural repair after a shock event. We extend a reliability approach to define and quantify structural resilience to introduce a method that continuously accounts for the repair and restoration throughout the lifetime of the structure. This approach accounts for the repair after a shock event based on a desired performance level, repair time of the component, and post-repair performance of the structure. We use the resilience levels to choose optimal repair strategy to maximize the overall resilience over the structural lifetime and minimize the repair costs.

The first step of the method is to estimate structural reliability. We model structural degradation over time and simulate structural live loads to estimate reliability for each component in terms of probability of failure. We use a system-reliability approach to model overall reliability of the structural system based on the individual component reliabilities. We introduce repair criteria and repair cases, define resilience and estimate structural resilience over time. The shock loads are modeled as Poisson events. Therefore, we simulate 1000 scenarios at each time step and list the

components needing repair whenever applicable and estimate the running probability of repair for each component over time. We use these results for the cost analysis over time to find the optimal strategy.

The applicability of the approach is demonstrated using an existing highway bridge in Colorado as presented in [1]. We estimate reliability of each component over a time-span of 100 years, model the bridge as a series-parallel system to use a system reliability approach to estimate its structural reliability. Based on the repair cases, the resilience is estimated, and an optimal strategy is chosen based on projected costs and resilience. We show our strategy to be consistent with [1] as a validation for the proposed approach.

8.2 Background and related work

The reliability methods have been increasingly gaining popularity in civil engineering to estimate project and infer structural behavior over its lifetime. Researchers either use a system reliability approach based on the possible structural failure modes or a representative stochastic model to quantify reliability. In [17], the researchers use a system reliability approach to visualize a bridge as a series-parallel combination of individual components, based on the failure modes and load propagation. Limit state equations are developed for each failure mode and loads are modeled to calculate the reliability of the bridge system for cost-assessment purposes. Such an approach is specific to a structure and it requires an analysis to identify all the failure modes at component level. On the contrary, another study [16] proposes a stochastic model to quantify structural reliability. Representative distribution functions are used to model loadings and deterioration of the structure to estimate reliability over the structural lifetime. Such a model is scalable and universally applicable to any structure with proper identification of model parameters. We use a

hybrid approach where we use a stochastic formulation to estimate reliability at the component level as proposed in [78] and then use a system based approach visualizing the system as a series-parallel combination of its component and the total probability rule to calculate system reliability. We model structural degradation using the approach proposed in the previous chapter, where degradation is modeled as a probabilistic sum of a random number of degradation modes acting on a component at a particular time. The proposed degradation function also accounts for the change in environmental properties affecting the degradation over time. The loads are modeled as Poisson events.

The modern societies and studies are increasingly focusing on more resilient infrastructure. The evaluation of risk, reliability, and restoration are all important aspects of resilience. We can model structural risk based on regional hazard maps or by simulating specific shock scenarios. A number of studies that focus on structural restoration in the aftermath of a single natural or manmade catastrophe. For example, the process of restoration under a seismic hazard is assessed and studied in [104]. However, the resilience of a structure is a combination of multiple aspects before, during, and after a shock event. There are varying definitions of resilience across different fields. The US Department of Homeland Security [105], Multidisciplinary Center for Earthquake Engineering Research (MCEER) [104], and Haines [106] have defined resilience for civil engineering systems. . The US Department of Homeland Security says that resilience is “the capacity of an asset, system, or network to maintain its function during or to recover from a terrorist attack or other incident”. MCEER defined it as “the ability of the system to reduce the chances of shock, to absorb a shock if it occurs and to recover quickly after a shock (re-establish normal performance)”. One of the most commonly cited definition by Haines is “the ability of the system to withstand a major disruption within acceptable degradation parameters and to recover within an acceptable time and

composite costs and risks”. These definitions highlight the significance of estimation of each of the risk, reliability, and restoration as a part of structural resilience.

The quantification of structural resilience is a combination of multiple metrics. In [107], resilience is defined as the area under the reliability-performance curve for a specific period of time. Resilience is quantified as the probability that a water-delivery system maintains its robustness and rapidity standards under a seismic event in [108]. In [109], resilience is quantified in terms of system reliability along with an addition of repair costs. An annual resilience metric is proposed in [110], which is a measure of actual annual reliability to the target reliability. We extend this approach to quantify resilience to account for repair time in the reliability estimates to quantify an expected annual resilience.

In the Methodology Section, we first describe the method to quantify component reliability which includes a degradation model, followed by quantification of system reliability. We then propose repair cases and resilience formulation. Finally, we use the resilience quantification to estimate repair costs and find the optimal repair strategy. In the Application Section, we apply the proposed method on a highway bridge from [17] and present the results in the Results Section.

8.3 Methodology

8.3.1 Flowchart

The general flowchart for the method is as follows in Figure (9-1)

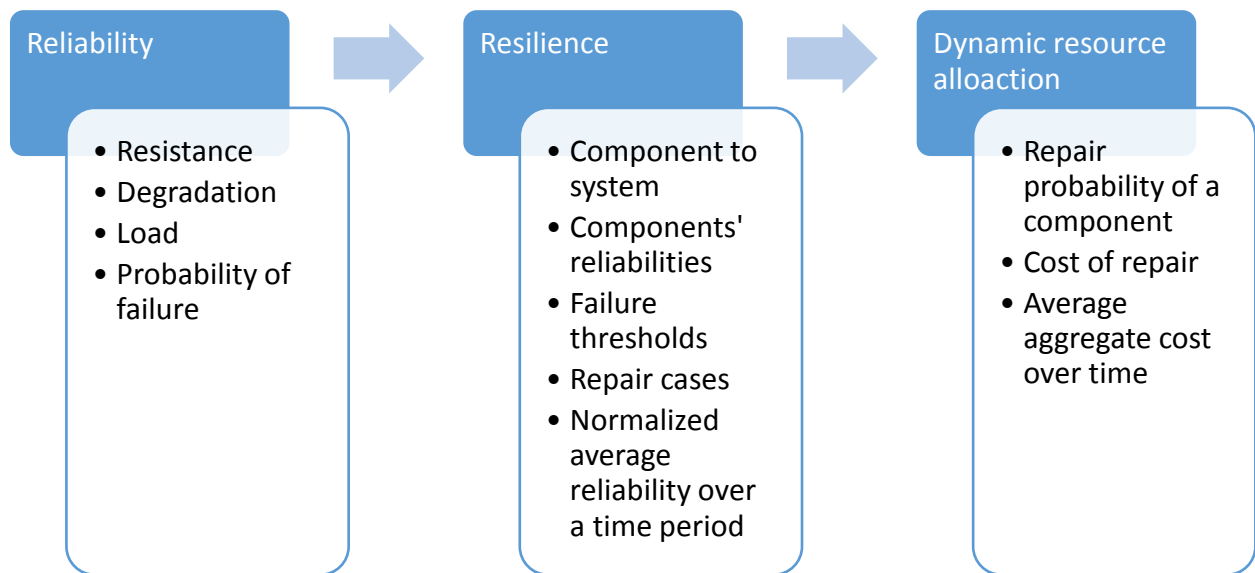


Figure 8-1 Flowchart for the methodology

8.3.2 Component reliability

Component reliability is calculated using the approach proposed in [16] and as used in [78]. The reliability of a structural component is described in terms of the probability of failure. The probability of failure is calculated as the probability of the structural resistance at any time step being lower than the loading. The probability of failure P_f of a component is a function of time given as

$$P_f(t) = P[R(t) < S(t)] = \int_0^\infty F_{R,t}(s) f_{S,t}(s) ds \quad (1)$$

where $R(t)$ is the resistance as a function of time, $S(t)$ is the load function, and F and f denote respectively the CDF and PDF. The loading and the resistance are assumed to be statistically independent, as the structural resistance is modeled in terms of degradation.

Now, we define hazard function $h(t)$ as the probability of failure of the structure in the time interval from t to $t + dt$ given that the structure has survived up to time t as

$$h(t) = \frac{P(t_f \leq t+dt | t_f > t)}{dt} = \frac{P(t < t_f \leq t+dt)}{P(t < t_f) dt} \quad (2)$$

where t_f is the time of failure. Assuming the loads to be Poisson with an arrival rate of $\lambda(t)$, the numerator of equation (2) can be expressed as

$$P(t < t_f \leq t + dt) = \lambda(t) dt \cdot P[R(t + dt) < S(t + dt)] \cdot P(t < t_f) \quad (3)$$

Hence, the hazard function is given as

$$h(t) = \lambda(t) \cdot P[R(t + dt) < S(t + dt)] \quad (4)$$

Assuming dt is infinitely small

$$P[R(t + dt) < S(t + dt)] = 1 - P[S(t + dt) < R(t + dt)] = 1 - F_S[R(t + dt)] \quad (5)$$

Therefore, hazard function is

$$h(t) = \lambda(t) \cdot [1 - F_S\{R(t)\}] \quad (6)$$

The hazard function is also related to the structural reliability $L(t)$ as

$$h(t) = -\frac{d}{dt} \ln[L(t)] \quad (7)$$

Therefore, the structural reliability and probability of failure are expressed as

$$L(t) = \exp\left[-\int_0^t \lambda(t) \cdot [1 - F_S\{R(t)\}] dt\right] \quad (8)$$

$$P_f(t) = 1 - L(t) \quad (9)$$

8.3.3 Degradation function

Structural degradation for the purpose of this study is assumed to be the structural deterioration due to natural and environmental causes over time, and due to the change in mechanical properties due to regular everyday loading. It is derived in the previous chapter. The degradation function is derived as a time dependent random weighted sum of various degradation modes acting on the structure, with weights indicating the respective contributions of each mode to overall degradation $\theta(t)$, as

$$0 \leq \theta(t) = \sum_{i=1}^{N(t)} w_i F_i(t) \leq 1 \quad (10)$$

$$\sum_{i=1}^{N(t)} w_i = 1 \quad (11)$$

where $N(t)$ is the number of degradation modes acting at time t , and $F_i(t)$ is the estimating stochastic function and w_i the corresponding weight for the i^{th} degradation mode. Each individual degradation mode can be modeled as an estimator function. However, not all modes act independently as there are mechanical interdependencies between different modes. For example,

in reinforced concrete structures, carbonation or abrasion can increase the rate of corrosion. Therefore, to account for these effects, we model the estimator for the i^{th} mode as

$$F_i(t) = f_i(t) + f_{ji}(t) \quad (12)$$

where $f_i(t)$ is the estimator function for the individual i^{th} mode and $f_{ji}(t)$ is the effect of the j^{th} mode on the i^{th} mode. $f_{ji}(t)$ is assumed to follow the same form as $f_i(t)$, but its arrival is the same as the arrival of the j^{th} mode. Thus, we model the influence of one mode on the rate of another while not changing the way in which the original mode affects a structural component.

The final form for the degradation function is the following

$$\theta(t) = 1 - e^{-\lambda t} - \frac{\log(1+(\lambda t)^{\frac{1}{n}})}{n!} \frac{e^{-\frac{\lambda}{n}t}}{rn} \quad (13)$$

This function has two unknown parameters n and λ . n can be viewed as the number of degradation modes and λ the Poisson rate of arrival of later degradation modes. This model fits the expected fundamental properties of degradation as discussed in terms of bounds and limits. The function is adaptable to change in structural properties over time based on the change in the two parameters. As there are only two parameters that need to be estimated, the function provides a way to estimate long-term structural degradation with limited data.

8.3.4 Risk quantification

The first step in reliability analysis is to estimate and quantify the risk on the structure. Risk is quantified in term of the live loading on the structure. The regular live load on a structure can be estimated based on the design live loads as per the design equations. Additionally, the intensity and frequency of live loads due to natural hazards can be estimated based on the hazard maps of

the region. Our methodology also helps in the estimation of the effect of shock events on the structure through the quantification of reliability under the shock loading. The intensity of these live loads is used in the methodology as a fraction of the structural resistance, converted using critical design equations.

System reliability

The reliability of the system is also defined in term of the probability of failure of the system by Equation (9). To calculate the probability of failure of the system, we first visualize the system as a series-parallel system of its components. We use a hybrid approach instead of using failure modes. First, we select different subsystems of the structure which are essential for the structure to be functional. For a bridge system, every bridge column is a separate subsystem along with the superstructure as one separate subsystem. Similarly, for a building structure, every story is a separate subsystem and every load bearing column is also a subsystem. At the subsystem level, we create a series-parallel system based on load distribution. The system is visualized a system of all the subsystems in series with each other. The probability of failure of the system is calculated using the total probability rule as the probability of at least one subsystem in series failing.

8.3.5 Repair cases

We set a threshold of probability of failure to decide that a component requires repair. We differentiate between repair of the structural system and repair of an individual component. If the probability of failure of a component is higher than the set threshold then that component is replaced in the aftermath of a shock event. This act of replacing an individual component is defined as repair for the structural system. Therefore, repair is quantified in terms of replacement of a single component, which is a small part of the structural system. We assess the probability of

failure of the system and each component and set two different thresholds for the failure of the structural system and the failure of a component, respectively. The threshold for the probability of failure of system is used to define Class E, which is the complete failure of the system. Based on the thresholds, following strategy is used:

- Class A- No failure, functional structure, no repair
- Class B- Functional structure but failure of non-critical components, no repair
- Class C- Functional structure but failure of multiple non-critical components, repair
- Class D- Non-functional structure, failure of one or more critical components, replacement of failed components
- Class E- Failure of all critical components, replacement of the entire structure

The critical components are the subsystems in series. We assume that the structure is not functional if at least one of the critical components fail and a repair must be undertaken. We use this described repair strategy to decide repair. Under this analysis, we simulate 1000 different scenarios as the loading is assumed to be Poisson and the need for repair is assessed at every point in time and repair is undertaken as soon as it is necessary. If a component has a probability of failure higher than the threshold at any time, then the process for its replacement immediately starts. The probability of repair of a component at any time is the total number of scenarios when it is replaced up till the time in consideration out of the total 1000 scenarios given as

$$P_{repair}(t) = \frac{\text{Total number of repairs till } t}{1000} \quad (14)$$

The repair time and cost of repair is decided at the component level. It is assumed that the reliability of component becomes 1, after a replacement. Therefore, the total reliability of the structure is expected to increase after a repair for the specific scenario. The repair time is a combination of response time and the replacement time. Figure (9-2) shows a representative reliability curve of a component after a shock event.

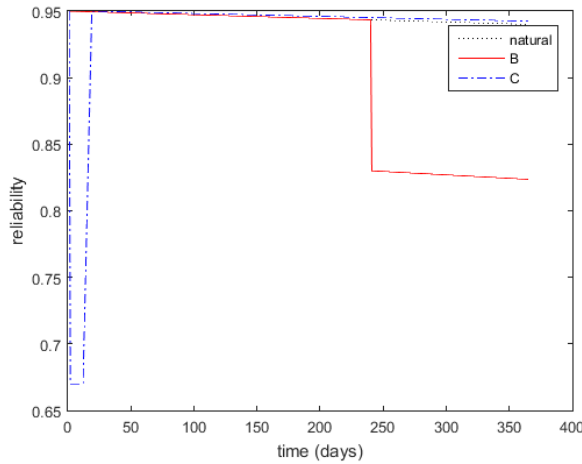


Figure 8-2 Reliability of a component under different repair scenarios

From Figure (9-2), for a hypothetical threshold for probability of failure of 0.3, we replace the component for repair case C. In this case, a shock event occurs in the beginning and the probability of failure is higher than the repair threshold, therefore, we start the process of replacing the component at the time of the event. The component reliability is the same as its reliability in the immediate aftermath of the event during the response time of a few days. Then the reliability gradually increases to 1 during the replacement time. It is compared to the ‘natural’ reliability of the component which is based on a scenario with no shock event and natural degradation. After replacement, the reliability of component is higher than its natural state without any repairs. Similarly, another shock event of a lower intensity occurs later in the next case where the

probability of failure is lower than the threshold and the component falls under repair scenario B. In this case, the component does not require a replacement and can continue to function even though its overall reliability has reduced due to the event.

8.3.6 Resilience

Resilience is calculated as an annual running average of fraction of actual reliability with respect to a target reliability curve. The target reliability curve should be user defined based on expected performance levels over time. Ideally, we should have expected target reliability levels at certain time intervals over the lifetime of the structure and a curve-fit should result in the target reliability curve. For this study, we assume that the target reliability is the reliability curve of the structure without any shock loads. It is the reliability based on natural degradation. The actual reliability is based on shock events and repair cases. Resilience at a particular instant of time is based on the average fraction over the year leading up to the time under consideration.

$$\rho = \frac{\int_0^T L_S(t)dt}{\int_0^T L(t)dt} \quad (15)$$

where, $L_S(t)$ is the reliability curve under simulated shock events while $L(t)$ is the natural reliability curve, and T is 365 days. The time period to calculate an average is chosen to be 365 days to standardize the resilience value as annual resilience, so that we can compare the annual resilience levels for different scenarios and quantify the difference at a set standard. As the reliability and repair will depend on the Poisson distributed loading, the resilience at a particular time is calculated as the mean of 1000 different resilience curves based on different loading scenarios over the yearly time period. Resilience can be improved by increasing reliability or decreasing repair time.

8.3.7 *Dynamic resource allocation*

The resource allocation for this study is the choice of repair strategies and allocation of associated costs. The resilience curve is used for the optimization of the resource allocation for the structure. It helps to come up with a strategy to optimize the repair and maintenance of the structure over its time period. The system resilience curve at any time contains a table of repair probabilities for each component up to that time and the current reliability of each component and the system as a whole. The system resilience and repair probabilities for each components are based on the set threshold for probability of failure. The goal is to optimize under the constraints of maximizing system resilience and reducing costs. At every point in time, we get probability of repair and cost of repair for each component. The cost of repair is calculated as the expected cost of repair for the particular component, calculated as the cost of replacement of the component times the probability of repair of the component. We can compare the lifetime cost curves to lifetime system resilience curves for decision making. The cost curve for one specific resilience curve would provide multiple options for repair and maintenance of the structure over its lifetime. The number of components needing repair increase along with the increasing cost over time. This methodology helps in choosing a resilience level and deciding a repair strategy to optimize for cost over the structural lifetime. It is best shown in the application example in the next sections. This methodology results in sets of projected cost curves and resilience curves at different performance levels. A decision making process will involve choose for a tradeoff between cost and performance level. Once a specific set of resilience and sot-curve is chosen, then the most optimal repair strategy in terms of component repair can be identified.

8.4 Application

The proposed approach is applied to a highway bridge in the state of Colorado and the plan for the bridge is shown in Figure (9-3), as adopted from [1].

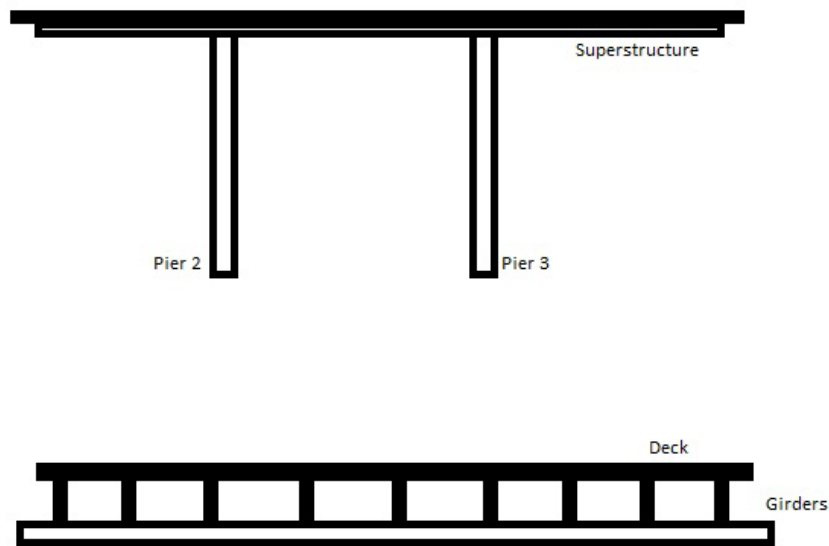


Figure 8-3 Representative plan for the Highway Bridge, elevation and cross-sectional views, from [1]

Figure (9-3) shows the bridge system with two columns and a superstructure consisting of 9 girders. This is a representative figure showing the components that are used in this study. For the bridge in consideration, the structural system is a series combination of the two piers and the superstructure. The superstructure subsystem consists of the deck in series with the girders in parallel. The component reliability analysis is based on the structural and loading properties from [2] and [3]. The design equation $0.9R_n = 1.4D_n + 1.7L_n$ specified in ACI 318 and used in [2] and

[3] is used to estimate nominal dead load, where the subscript n represents the code specified values. While this code has since been superseded by newer codes, it was chosen to facilitate comparison with the cited studies. For simplicity and consistency, it is assumed that $D_n = L_n$ and $R_n = R_0$. R_0 is the component resistance at time 0. The structural resistance $R(t) = R_0 \cdot \theta(t)$. The mean values for parameters for $\theta(t)$ are $n = 3.4$ and $\lambda = 0.07$ as used in [4]. These parameters are distributed with a covariance of 0.1 for each component. There are three different loadings assumed to be applicable on the structure. The first live load with mean intensity $LL_1 = 0.15L_n$ has a Poisson arrival rate of 1/day, while the shock loads, 2nd live load has the mean intensity of $LL_2 = 0.40L_n$ and occurs once/year, and the third live load with mean intensity $LL_3 = 0.80L_n$ occurs once every four years. The covariance for first live load is 0.1 and 0.2 for the other two events.

The response time for repairs is assumed to be normally distributed taking positive values with mean 10 and standard deviation of 5. The replacement time for each girder is similarly normally distributed with positive values with a mean of 1 and standard deviation of 0.2, the replacement time for deck has mean 3 and standard deviation 1, for columns the mean is 7 and standard deviation is 2. The cost of replacing components is based on costs from [1] and are extrapolated to component level costs. A 3% rate of inflation per year is added in cost calculations.

8.5 Results

Based on the parameters mentioned in the previous Section, we run 1000 different simulations that calculate the reliability and automatically use the repair cases wherever necessary. Figure (9-4) shows a distribution of reliability curves for a single component for a year. At every time step there are 1000 different simulations of loading and we obtain a reliability value corresponding to that

load. When the reliability is below the threshold of 0.5, there is a repair time for the component during which the reliability stays below the threshold and the process of undertaking a replacement is initiated. Once the repair process is complete, the component is replaced and its reliability goes to 1. For other simulations, where the reliability plummets but is still above the threshold, the reliability curve shows a sudden decrease at the shock loading event and then continues its decreasing trend. However, for most of the simulations, the loading is regular and they do not suffer a shock loading due to the Poisson arrival nature and low frequency of the events, and therefore, most of the reliability curves lie in a small band close to a value between 0.95-0.97. So, the reliability increases for some of the simulations after a repair but most of the simulations still have show a decreasing trend. Therefore, on average the trend is decreasing at any time step.

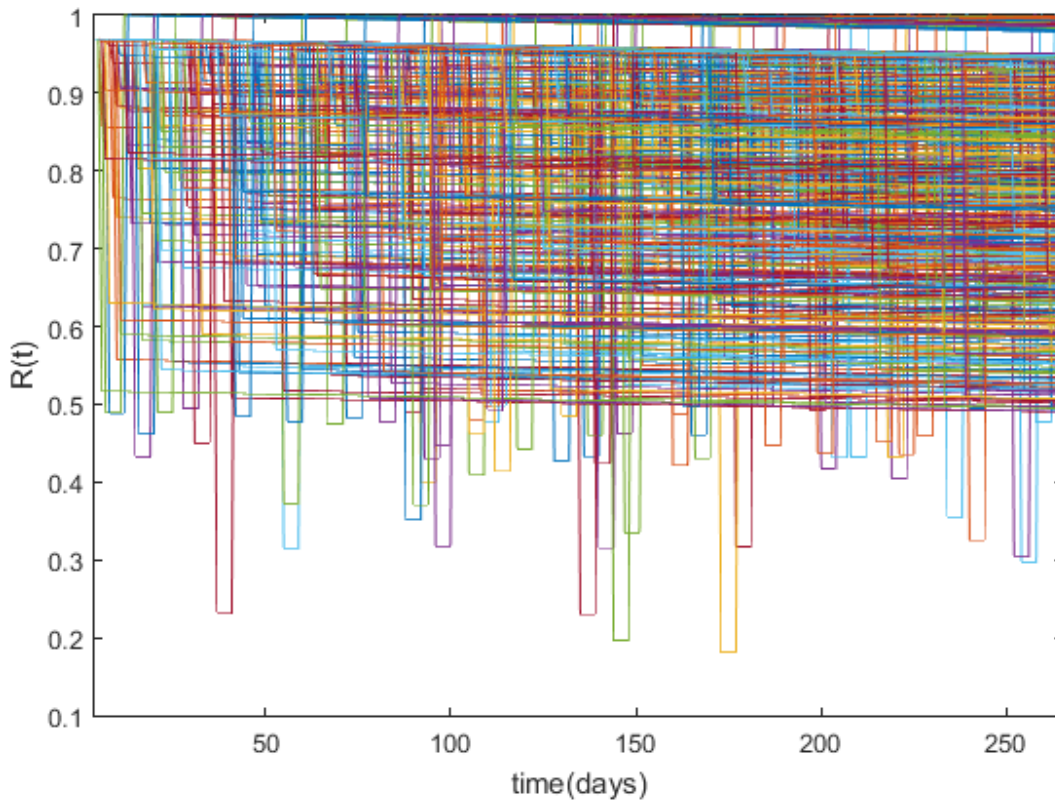


Figure 8-4 1000 simulations of reliability for a single component over one year

Figure (9-5) shows the resilience curve for a single component over a duration of time. The resilience curve is an average of 1000 reliability curves as a fraction of natural reliability curve. At any instant of time, it tells the resilience of the component and the probability of it being in different repair scenarios. It calculates the total cost of repairs for the component until the time in consideration and the repair scenarios invoked. This plot is a representation of the information available and represented by the resilience curve through time. The system resilience curve contains all of this information for each component which will help in decision making along with the cost.

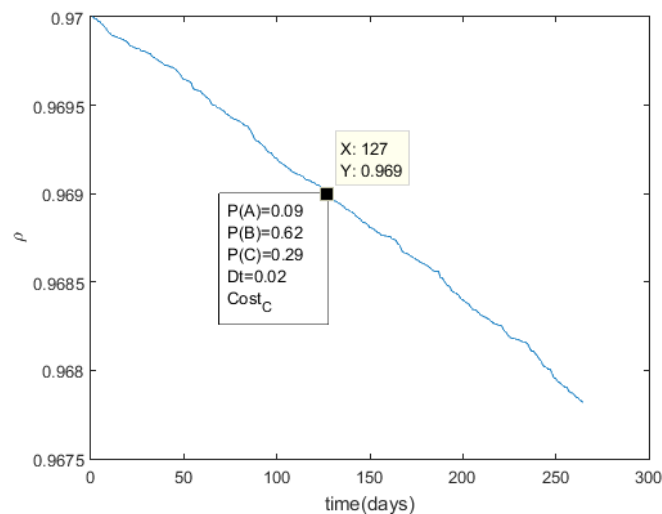


Figure 8-5 Resilience curve for a single girder

Figure (9-6) shows the 100 year curves for the resilience of the structure for different levels of reliability thresholds for the system. For this study, we use the same reliability thresholds for both the system and components to choose the repair scenarios. Each of these curves is an average of 1000 different simulations of loading scenarios. Under each scenario, the methodology chooses the repair case at every instant of time based on the reliability threshold. If required, it replaces the component needing repair, increasing its reliability to 1, and increasing the overall reliability of

the system. However, the repair cases are relatively low at each time step, hence the overall average is still globally decreasing as most of the other scenarios at that time will have a lower resilience than previous time step due to natural deterioration. Initially, the difference in resilience is increasing with the decrease in reliability threshold because fewer and fewer repairs are undertaken. However, the curves for the reliability threshold of 0.2 and 0.1 are close because the reliability of system gradually decreases at a much higher rate because of the lack of repairs and it will require a number of simultaneous repairs in the end. These curves for the mean resilience based on reliability thresholds also document the total number of repairs per component across all the scenarios to calculate the probability of repair for each component at every time step.

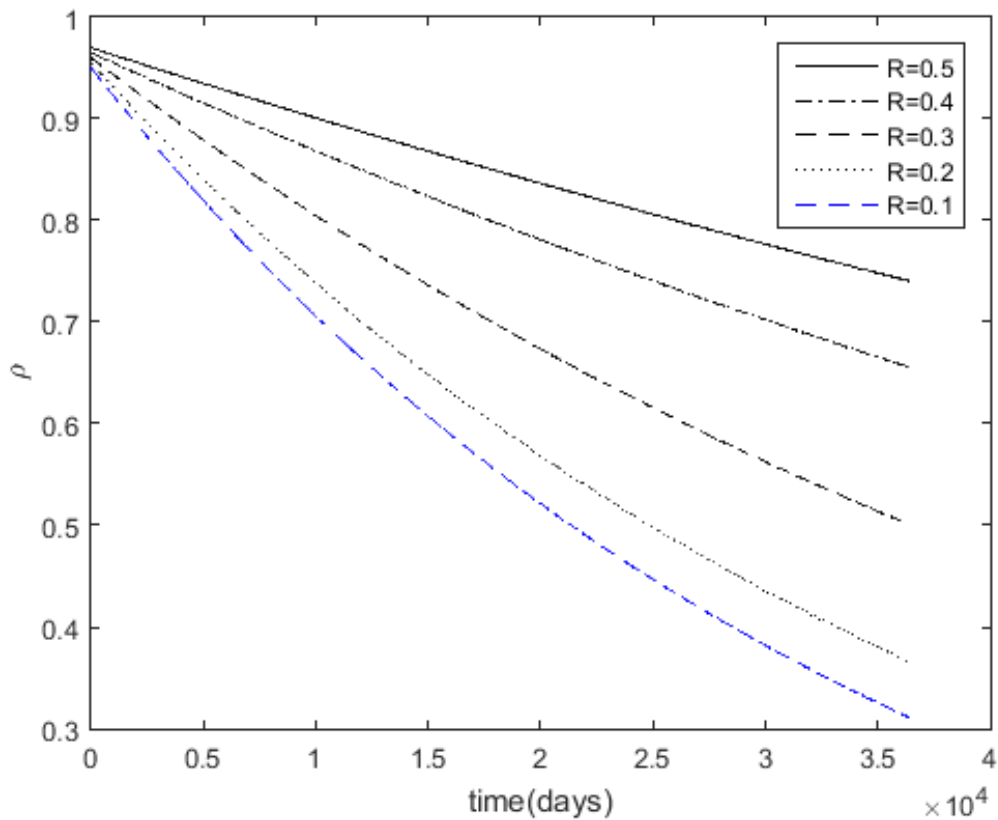


Figure 8-6 Resilience curves for different reliability thresholds

Corresponding to each resilience curve for every reliability threshold, the cost curves are presented in Figure (9-7). The costs are calculated based on the expected cost of total repairs until a certain point in time, which is the sum of expected cost of replacing different components. The expected cost of replacing a component at a time is calculated as a multiplication of the cost of replacing that component and the probability of repair of the component.

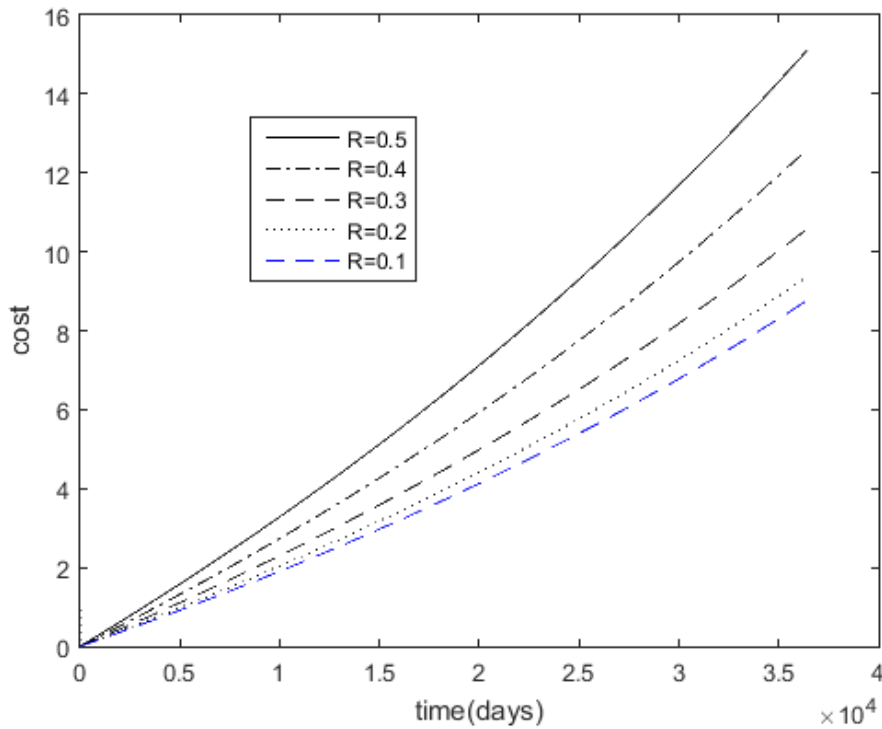


Figure 8-7 Cost curves for different reliability thresholds

Figure (9-6) and (9-7) together show a direct tradeoff between expected resilience of the structure and the associated costs over the lifetime. The first step in approximating the allocation of resources is to choose a strategy based on an expected performance level of the structure. Based on the choice of the performance level and the corresponding resilience curve, we get the associated cost curve. The 2nd step is to use the cost curve to choose the repair strategy over the

structural lifetime keeping in mind that the projected costs for the desired resilience level are exponentially increasing over the time.

For this study, we choose a performance level corresponding to a reliability threshold of 0.5 for the structure and its individual components. Figures (9-8) and (9-9) show the distribution of resilience for the chosen performance level. The plots shows the distribution of resilience about the mean and 2 degrees of standards deviation calculated from the 1000 different resilience curves for the desired performance level. Figure (9-9) shows the fluctuations over time steps in details because of the stochastic modeling of the intensity and the arrival time of the shock loading. It provides an insight on the projected resilience distribution for simulated intensities of shock events and an estimate of the worst case deviation.

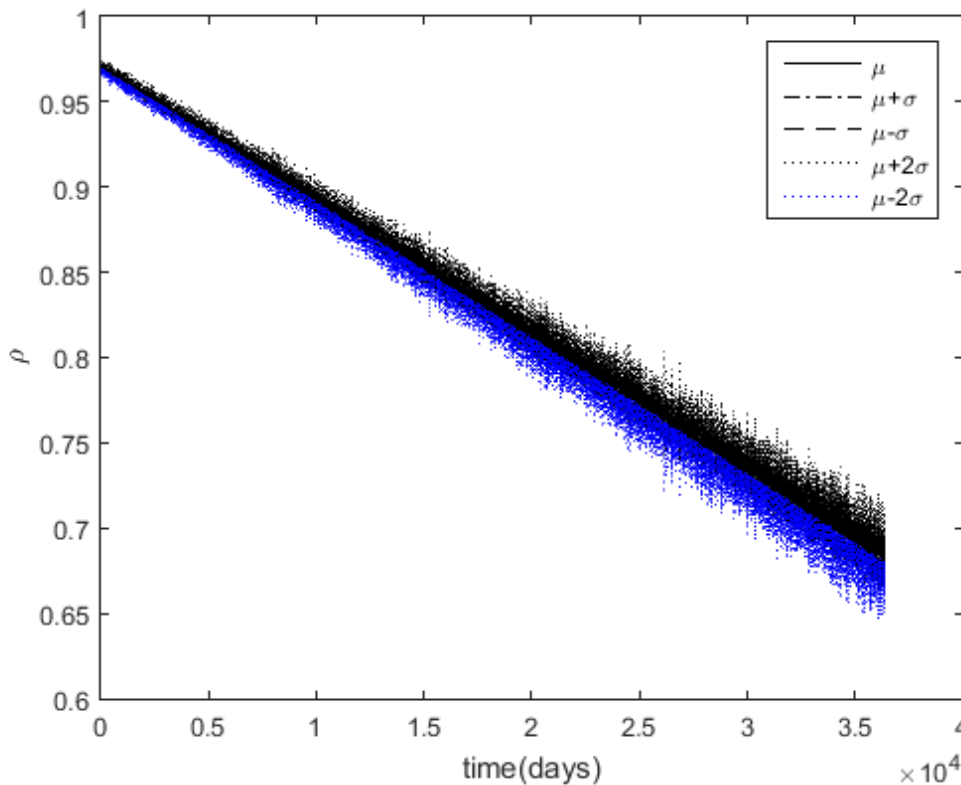


Figure 8-8 Resilience distribution with mean and standard deviation for reliability threshold of 0.5

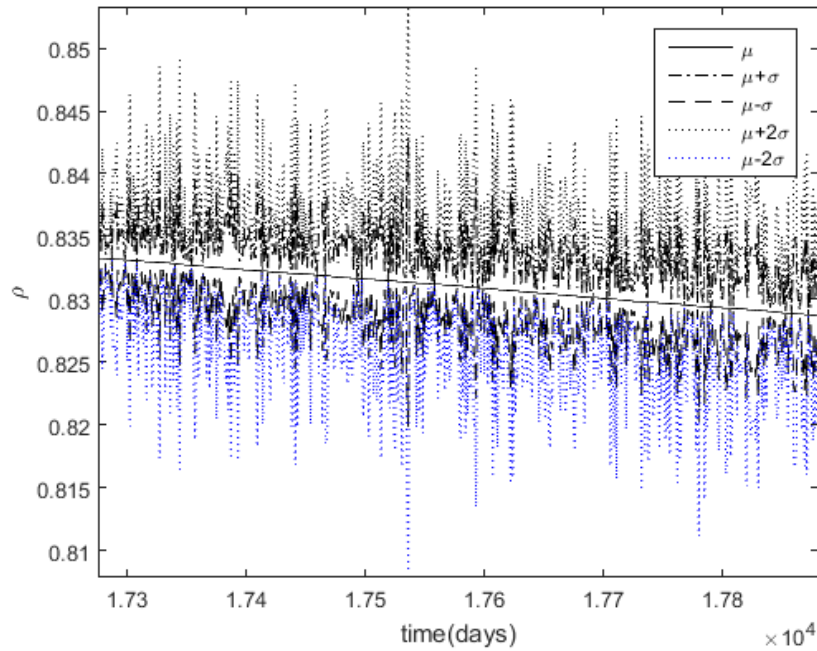


Figure 8-9 Resilience distribution with mean and standard deviation for reliability threshold of 0.5, zoomed

Figures (9-10) and (9-11) show a similar distribution of associated costs with respect to the chosen performance level. It helps us with the decision making providing a cost range at every time step. It also helps in quantifying the uncertainty in associated costs. The methodology can include more factors inducing uncertainty to provide a good estimate of the range of costs at any time.

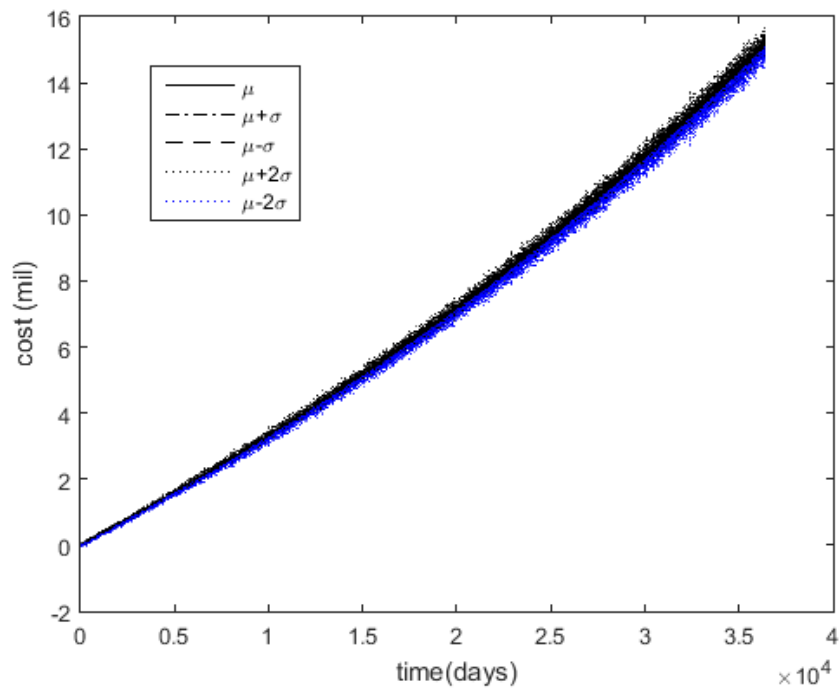


Figure 8-10 Cost distribution for the reliability threshold of 0.5

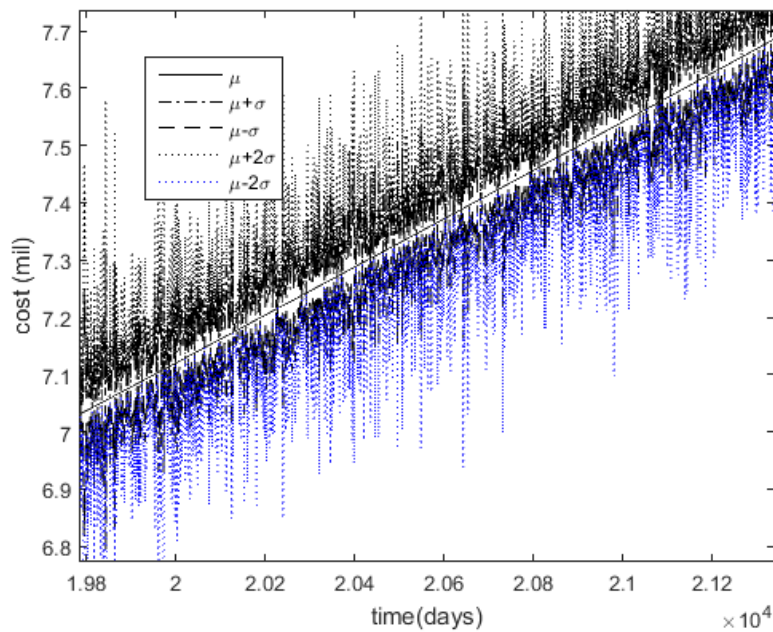


Figure 8-11 Cost distribution for the reliability threshold of 0.5, zoomed

The final step of the process is to use the resilience and cost plots for a chosen performance level for the decision making in allocating resources at specific times. We choose the repair strategy based on the repair probabilities of the components calculated at each time step. Given the constraints in replacing individual components, we choose a strategy based on a limited number of options, which are, replacing only the deck, replacing the superstructure, and replacing the entire structure. We constrain for the maximum repair probabilities of components and lowest lifetime system cost. Following are the optimal outcomes for the given structure:

- Replace the deck after 27 years, superstructure after 56 years, and the deck again after 87 years
- Replacement of the superstructure after 47 years and the entire bridge after 94 years
- Replacement of the entire bridge after 79 years

The options described above are the most optimal options for the desired performance level while minimizing the costs. These results are consistent with [1] in terms of action years. From a decision maker's perspective, this method helps in choosing multiple options along with the distribution of costs over a structural lifetime for different performance levels. The method is also not specific to a particular structure.

Now, we extend this approach to a network of 10 bridges as shown in Figure (9-12a) and Figure (9-12b). Figure (9-12a) shows the network on a 10X10 grid network, where each bridge is placed at the center of a random cell. Figure (19-2b) shows the resulting transportation network for an O-D pair at the diagonal ends of the grid. These bridges are similar to the bridge discussed in previous section. The structural parameters for each bridge are normally distributed with a c.o.v. of 20% and mean equal to the parameters in the previous section.

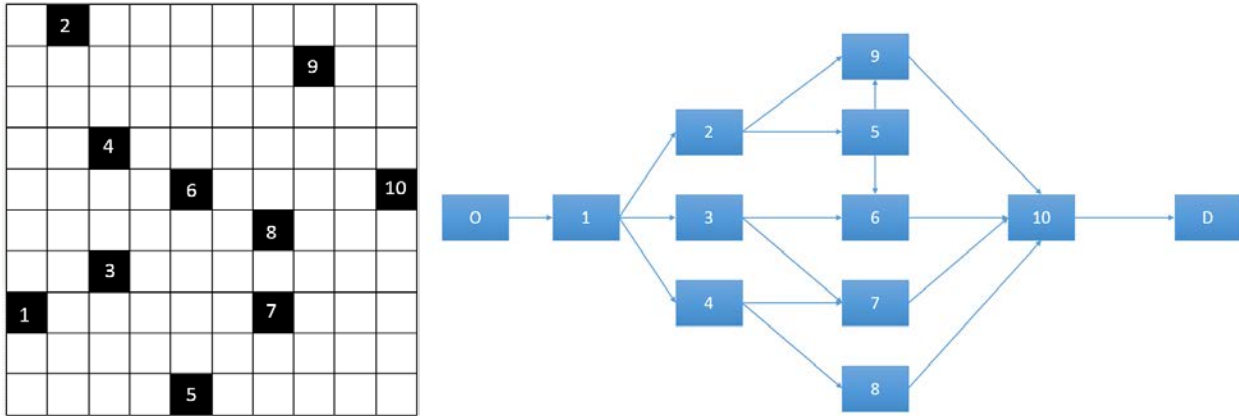


Figure 8-12 10 bridge network (a) on the grid, (b) as transportation network

For a network, we are interested in quantifying the impact on the resilience of the network if a component is shut down. A component may be shut down due to repair or a localized shock load event. In both the cases, the first step is to redistribute the loads on the rest of the network and then we quantify the reliability and impact on the long-term resilience due to the additional redistributed loads. If a component i is shut then the additional loading on component j will be $w_j l_i$, where l_i is the load corresponding to component i and w_j is the fractional weight for component j such that the load is distributed throughout the network. For an example case scenario, where component number 3 is shut down for usage, Figure (9-13) shows the weights for the redistribution of additional loads for each factors. These factors are estimated based on the distance of the grid and randomized travel costs, and using incremental analysis for 5% increments. Under such a scenario, the load associated with component number 3 is redistributed across the network.

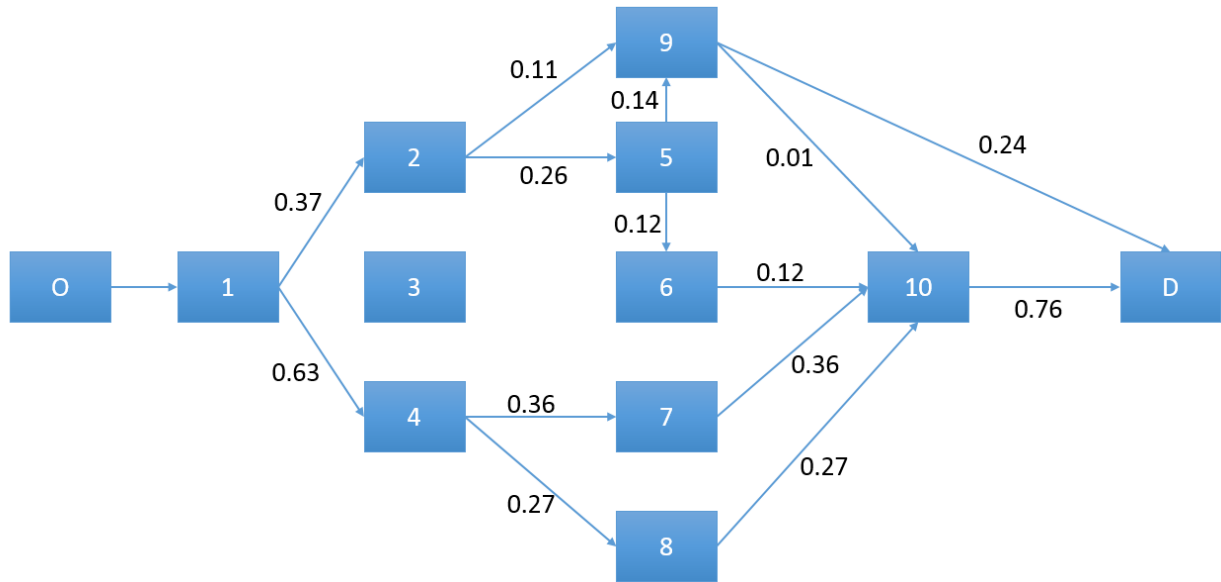


Figure 8-13 Associated weights for the redistribution of load due to component number 3

We generate the resilience and cost plots for each of these bridges by accounting for the additional load corresponding to the weight factors. Based on the repair cases presented in the methodology section, if a bridge is under repair case D or E, then it is shut down and it is distributed across the network for the duration of its repair. We then calculate the resilience of the rest of the bridges under the additional load for every simulation and obtain the resilience and cost plots. Figure (9-14) shows a scenario, where bridge 3 is shut down due to repair, and while its resilience increases after the repair process, the resilience of the rest of the bridges in the network decrease due to additional loads of bridge 3.

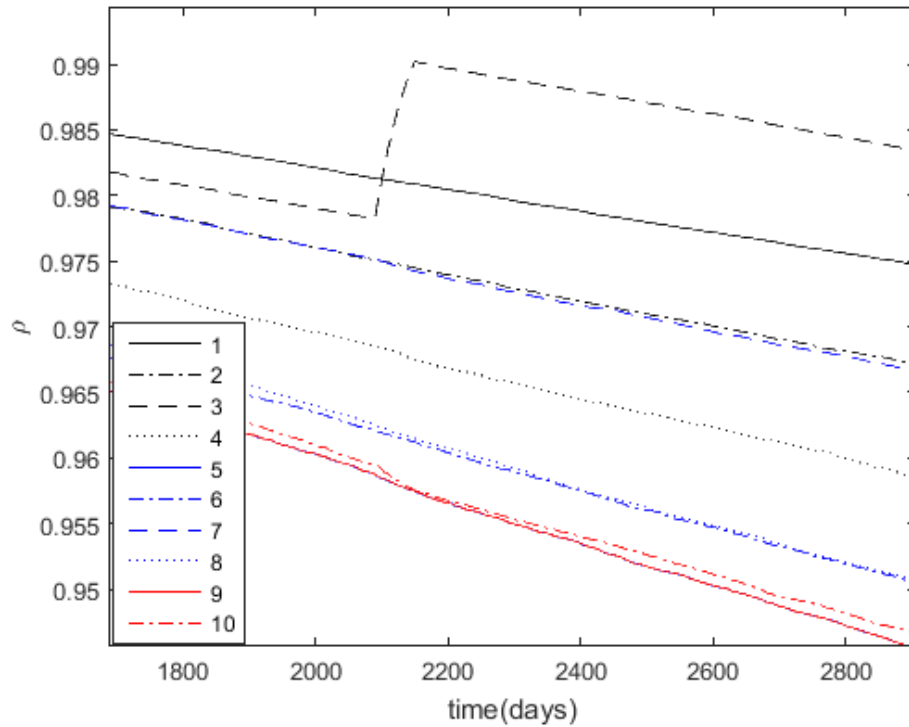


Figure 8-14 Change in the resilience of the network over time due to the shut down of component number 3 for repair

8.6 Conclusion

We propose a method to quantify resilience and use it to optimize resource allocation over the lifetime of a structure. The method extends the reliability-based approach from a component level to a system level while accounting for repair time and costs. The approach is not specific to any structure and can be used on any structure. We use a degradation model and simulate loads to quantify component reliability. A system based visualization helps in quantifying the overall reliability of the structure. We propose repair cases based on reliability thresholds and use it to quantify resilience as a continuous metric as a function of reliability and repairs over time. We estimate the associated repair costs for each component and use the costs to introduce continuous cost curves over time. The resilience and cost curves are simultaneously used to choose a performance level and find optimal repair strategies and options over the lifetime of the structure.

We use the proposed method on a highway bridge from Colorado, used in a cited study. With the help of the example case, we demonstrate the applicability of the method and show that the results are consistent with an approach specific to that bridge. We then extend this approach to a network to account for the effect of one component on others.

CHAPTER 9. FUTURE WORK

The work on near-term reliability processes accelerometer data in real time to infer the structural state. We have proposed general methodologies to estimate and predict the structural response and tested the proposed methodologies using experimental data at the laboratory scale. Future work is to use these methodologies on real-world data in the field on full-scale structures. Therefore, the fabrication of a localized structure-specific earthquake early warning system is the next step. This system should contain accelerometer(s) connected to a processor, which performs the proposed inference in real time, with connection to active or passive structural control systems. The implementation of such a system on a real-world structure will bring unique challenges. It is important to develop a system that is robust to noise and uncertainty in the system and ensure that it can be effectively implemented. Theoretically, our method is general and scalable. However, the next goal is to fabricate a system and ensure its generalizability and scalability on real structures.

The work on long-term reliability provides a general formulation to assess structural performance over longer periods of time. Future work extending the methods proposed in this research is to quantify the resilience of the system and predict its behavior under different levels of shock events at different times during the lifetime of the structure. This will enable predictions of system response for emergency resource allocation and preparedness under anticipated events. It will also help determine optimal structural repair strategies after an event to achieve pre-event service levels. The proposed resilience-cost plots can be used to evaluate tradeoffs to achieve target performance levels, with the objective to incorporate these results as early in the decision making process as possible. The aim is to incorporate these methods and their inference first, at the design

stage of a structure, and next, for maintenance decisions at each point in time, to improve the performance of the structure over its lifetime and increase its resilience to future events.

Throughout the lifetime of the structure, the availability of data about the structure and loadings facilitates more accurate the structural assessments with the proposed methodologies. However, few, if any, structures provide reliable data over full structural lifetimes. Additionally, the life of a structure spans over several decades and hence a full analysis over time is often not feasible. Therefore, a robust general stochastic formulation that is able to utilize any collected data is required to estimate the reliability and quantify the resilience of structures. A final area for future research is to implement the proposed method on a real-world infrastructure network to assess the performance under varying scenarios and support decision making to increase the reliability and resilience of structural systems.

REFERENCES

- [1] Tien, I.; Pozzi, M.; and Der Kiureghian, A. “Inference on maximum structural response based on measured accelerations using dynamic Bayesian network”, *Structural Safety*, 61:43-56, July 2016
- [2] Sakamoto, T.; Hori, N.; and Ochi Y. “Exact linearization and discretization of nonlinear systems satisfying a Lagrange PDE condition”, No. 10-CSME-68, E.I.C. Accession 3231, August 2010
- [3] Kalman, R.E. “A new approach to linear filtering and prediction problems”, *Journal of Basic Engineering*, 82(1): 35-45, 1960
- [4] Terejanu, Gabriel A. “Extended Kalman Filter tutorial”, University at Buffalo, Buffalo, 2008
- [5] Mariani, S.; and Ghisi, A. “Unscented Kalman filtering for nonlinear structural dynamics”, *Nonlinear Dyn* (2007) 49:131-150, Springer Science+Business Media B.V. 2007, January 2007
- [6] Nakamura, Y. “On the urgent earthquake detection and alarm system (UrEDAS)”, *Proceedings of 9th World Conference on Earthquake Engineering*, Tokyo-Kyoto, Japan, 1988
- [7] Kanamori, H. “Real-time seismology and earthquake damage mitigation”, *Annual Review of Earth and Planetary Sciences*, 33, 195-214, 2005
- [8] Wu, Y.M.; and Kanamori, H. “Experiment on an onsite early warning method for the Taiwan early warning system”, *Bulletin of the Seismological Society of America*, 95, 347-353, 2005
- [9] Wu, Y.M.; and Kanamori, H. “Rapid assessment of damaging potential of earthquakes in Taiwan from the beginning of P waves”, *Bulletin of the Seismological Society of America*, 95, 1181-1185, 2005
- [10] Wu, Y.M.; and Kanamori, H. “Exploring the feasibility of on-site earthquake early warning using close-in records of the 2007 Noto Hanto earthquake”, *Earth, Planets and Space*, 60, 155-160, 2008
- [11] Wu, Y.M.; and Kanamori, H. “Development of an earthquake early warning system using real-time strong motion signals”, *Sensors*, 8, 1-9, 2008
- [12] Allen, R.M.; and Kanamori, H. “The potential for earthquake early warning in southern California”, *Science*, 300, 786-789, 2003
- [13] Olson, E.L.; and Allen, R.M. “The deterministic nature of earthquake rupture”, *Nature*, 438, 212-215, 2005
- [14] Rezaeian, S; and Der Kiureghian, A “Simulation of synthetic ground motions for specified earthquake and site characteristics”, *Earthquake Engineering and Structural Dynamics*, 39, 1155-1180, 2014
- [15] Meehl, G.A., T.F. Stocker, W.D. Collins, P. Friedlingstein, A.T. Gaye, J.M. Gregory, R. Knutti, J.M. Murphy, A. Noda, S.C.B. Raper, I.G. Watterson, A.J. Weaver, and Z.-C. Zhao, (2007) “Global Climate Projections. In: *Climate Change 2007: The*

- Physical Science Basis. Contribution of Working Group I to the Fourth Assessment Report of the Intergovernmental Panel on Climate Change [Solomon, S., Qin, D., Manning, M., Chen, Z., Marquis, M., Averyt, K.B., Tignor, M., and Miller, H.L. (eds)]” Cambridge University Press, Cambridge, United Kingdom and New York, NY, USA
- [16] Li, Q., Wang, C., and Ellingwood, B.R. (2015) “Time-dependent reliability of aging structures in the presence of non-stationary loads and degradation” *Structural Safety*, 52, 132-141
- [17] Estes, A.; and Frangopol, M. “Repair optimization of highway bridges using system reliability approach” *Journal of Structural Engineering*, 125(7), July 1999
- [18] Murphy, K. “Dynamic Bayesian networks: representation, inference and learning”, Doctoral Thesis, 2002
- [19] Murphy, K. “Machine Learning: A Probabilistic Perspective”, MIT Press, 2012
- [20] Barber, D. “Bayesian reasoning and machine learning”, Cambridge University Press, 2012
- [21] Vanik, M.W.; and Beck, J.L. “A Bayesian probabilistic approach to structural health monitoring”, *Proceedings of the International Workshop on Structural Health Monitoring*, Lancaster, PA, 140-151, 1997
- [22] Vanik, M.W.; Beck, J.L.; and Au, S.K. “Bayesian probabilistic approach to structural health monitoring”, *Journal of Engineering Mechanics*, 126(7): 738-745, 2000
- [23] Katafygiotis, L.S.; and Yuen, K.V. “Bayesian spectral density approach for modal updating using ambient data”, *Earthquake Engineering and Structural Dynamics*, 30(8): 1103-1123, 2001
- [24] Yuen, K.V.; and Katafygiotis L.S. “Bayesian modal updating using complete input and incomplete response noisy measurements”, *Journal of Engineering Mechanics*, Vol. 128 No. 3: 340-350, 2002
- [25] Au, S.K.; Zhang, F.L.; and Ni Y.C. “Bayesian operational modal analysis: theory, computation, practice”, *Computers and Structures*, 126: 3-14, 2013
- [26] Tien, I. “Bayesian network methods for modeling and reliability assessment of infrastructure systems”, Doctoral Thesis, University of California, Berkeley, 2014
- [27] Zhang, F.; and Au, S. “Probabilistic model for modal properties based on operational modal analysis”, *ASCE-ASME J. Risk Uncertainty Eng. Syst., Part A: Civ. Eng.*, 10.1061/AJRUA6.0000843, B4015005, September 2015
- [28] Hoshiya, M.; and Saito E. “Structural identification by extended Kalman filter”, *Journal of Engineering Mechanics*, 110(12): 1757-1770, 1984
- [29] Jeen-Shang, L.; and Yigong, Z. “Nonlinear structural identification using extended Kalman filter”, *Computers and Structures*, Vol. 52, Issue 4, 757-764, August 1994
- [30] Al-Hussein, A. and Haldar, A. “Novel unscented Kalman filter for health assessment of structural systems with unknown input”, *Journal of Engineering Mechanics*, 141(7), July 2015
- [31] Mu, H.Q. and Yuen, K.V. “Novel outlier-resistant extended Kalman filter for robust online structural identification”, *Journal of Engineering Mechanics*, 141(1), January, 2015

- [32] Yang, J.N.; Lin, S.; Huang, H.; and Zhou, L. “An adaptive extended Kalman filter for structural damage identification”, *Structural Control and Health Monitoring*, 13(4): 849-867, 2006
- [33] Yang, J.N.; Pan, S.; and Huang, H. “An adaptive extended Kalman filter for structural damage identification II: unknown inputs”, *Structural Control and Health Monitoring*, 14: 497-521, 2007
- [34] Wu, M.; and Smyth, A.W. “Application of unscented Kalman filter for real-time nonlinear structural system identification”, *Structural Control And Health Monitoring*, 14:971-990, 2007
- [35] Chatzi, E.N.; and Smyth A.W. “The unscented Kalman filter and particle filter methods for nonlinear structural system identification with non-collocated heterogeneous sensing”, *Journal of Structural Control and Health Monitoring*, 2008
- [36] Xie, Z.; and Feng, J. “Real-time nonlinear structural system identification via iterated unscented Kalman filter”, *Mechanical Systems and Signal Processing*, Vol. 28, 309-322, April 2012
- [37] Hori, N.; Mori, T.; and Nikiforuk, P.N. “A new perspective for discrete-time models of a continuous-time system”, *IEEE Transactions on Automatic Control*, Vol. 37, No. 7, pp 1013-1017, 1992
- [38] Markazi, A.H.D. and Hori, N. “Discretization of continuous-time control systems with guaranteed stability”, *IEE Control Theory and Applications*, Vol. 142, No. 4, pp 323-328, 1995
- [39] Guy, J. “Lagrange characteristic method for solving a class of nonlinear partial differential equations of fractional order”, *Applied Mathematics Letters*, Vol. 19, Issue 9, 873-880, Sept 2006
- [40] Bouc, R. “Forced vibration of mechanical systems with hysteresis (Abstract)”, *Proc., 4th Conf. on Nonlinear Oscillation*, Prague, 1967
- [41] Wen, Y.K. “Methods of random vibration for inelastic structures”, *Applied Mechanics Reviews*, 42(2), 39-52, 1989
- [42] Rice, S. O. “Mathematical analysis of random noise”, *Bell System Technical Journal*, Vol. 23, No. 3, pp. 282-332, July 1944
- [43] Kijewski-Correa, T.; Kareem, A.; and Kochly, M. “Experimental verification and full-scale deployment of global positioning systems to monitor the dynamic response of tall buildings”, *Journal of Structural Engineering*, 132, 1242-1253, 2006
- [44] Filiatrault, A.; Christovasilis, I.P.; Wanitkorkul, A.; and van de Lindt, J.W. “Experimental seismic response of a full-scale light-frame wood building” *Journal of Structural Engineering*, 136(3), 246-254, 2010
- [45] Van de Lindt, J.W.; Pei, S.; Pryor, S.E.; Shimizu, H.; and Isoda, H. “Experimental seismic response of a full-scale six story light-frame wood building” *Journal of Structural Engineering*, 136(10), 1262-1272, 2010
- [46] Mahsuli, M.; and Haukaas, T. “Seismic risk analysis with reliability methods, part 1: models”, *Structural Safety*, Vol. 42, 54-62, May 2013
- [47] Bonstrom, H.; and Corotis, R.B. “Building portfolio seismic risk assessment using the first-order reliability method”, *Structural Safety*, Vol. 52 part A, 113-120, January 2015

- [48] Ellingwood, B.R.; and Kinali, K. “Quantifying and communicating uncertainty in seismic risk assessment”, *Structural Safety*, Vol. 31, Issue 2, 179-187, March 2009
- [49] Goulet, C.A.; Haselton, C.B.; Mitrani-Reiser, J.; Beck, J.L.; Deierlein, G.G.; Porter, K.A.; and Stewart, J.P. “Evaluation of the seismic performance of a code-conforming reinforced-concrete frame building- from seismic hazard to collapse safety and economic losses”, *Earthquake Engineering and Structural Dynamics*, 36:1973-1997, 2007
- [50] Liel, A.B.; Haselton, C.B.; Deierlein, G.G.; and Baker, J.W. “Incorporating modeling uncertainties in the assessment of seismic collapse risk of buildings”, *Structural Safety*, Vol. 31, Issue 2, 197-211, March 2009
- [51] Pant, D.R.; Constantinou, M.C.; and Wijeyewickrema, A.C. “Re-evaluation of equivalent lateral force procedure for prediction of displacement demand in seismically isolated structures”, *Engineering Structures*, Vol. 52, 455-465, July 2013
- [52] Decó, A.; Bocchini, P.; and Frangopol, D.M. “A probabilistic approach for the prediction of seismic resilience of bridges”, *Earthquake Engineering and Structural Dynamics*, Vol. 42, Issue 10, 1469-1487, August 2013
- [53] Bozorgnia, Y.; and Bertero, V.V. “Damage spectra: characteristics and applications to seismic risk reduction”, *Journal of Structural Engineering*, 129(10), 1330-1340, 2003
- [54] Singhal, A.; and Kirmidjian, A.S. “Method for probabilistic evaluation of seismic structural damage”, *Journal of Structural Engineering*, 122(12), 1459-1467, December 1996
- [55] Wurman, G.; Allen, R.M.; and Lombard, P. “Toward earthquake early warning in northern California”, *Journal of Geophysical Research*, 112-B8, 2007
- [56] Allen, R.M. “The ElarmS earthquake early warning methodology and its application across California”, *Earthquake Early Warning Systems*, Springer, 21-44, 2007
- [57] Allen, R.M.; Brown, H.; Hellweg, M.; Khainovski, O., Lombard, P.; and Neuhauser, D. “Real-time earthquake detection and hazard assessment by ElarmS across California”, *Geophysical Research Letters*, 36, 2009
- [58] Cua, G.; and Heaton, T. “The virtual seismologist (VS) method: a Bayesian approach to earthquake early warning”, Springer: Berlin Heidelberg, 97-132, 2007
- [59] Wu, Y.M.; Kanamori, H.; Allen, R.M.; and Hauksson, E. “Determination of earthquake early warning parameters, τ_c and P_d , for southern California”, *Geophysical Journal International*, 170, 711-717, 2007
- [60] Shieh, J.T.; Wu, Y.M.; and Allen, R.M. “A comparison of τ_c and τ_p^{\max} for magnitude estimation in earthquake early warning”, *Geophysical Research Letters*, 35, 2008
- [61] Böse, M.; Hauksson, E.; Solanki, K.; Kanamori, H.; and Heaton, T.H. “Real-time testing of the on-site warning algorithm in southern California and its performance during the July 29 2008 Mw 5.4 Chino Hills earthquake”, *Geophysical Research Letters*, 36, 2009
- [62] Böse, M.; Heaton, T.; and Hauksson, E. “Rapid estimation of earthquake source and ground-motion parameters for earthquake early warning using data from a single three component broadband or strong-motion sensor”, *Bulletin of the Seismological Society of America*, 102-2, 738-750, 2012

- [63] Cheng, M.H.; Wu, S.; Heaton, T.H.; and Beck J.L. “Earthquake early warning application to buildings”, *Engineering Structures*, 60, 155-164, 2014
- [64] Tien, I.; Pozzi, M.; and Der Kiureghian, A. “Inference on maximum structural response based on measured accelerations using dynamic Bayesian network”, In G. Deodatis, B. Ellingwood, and D. Frangopol, eds. *Safety, Reliability, Risk and Life-Cycle Performance of Structures and Infrastructures*, New York: CRC Press, 2481-2488, June 2013
- [65] Saini, A.; and Tien, I. “Estimating maximum nonlinear structural response based on sensor measurements: a probabilistic framework”, EMI/PMC 2016
- [66] Esteva, L.; and Rosenblueth, E. “Espectros de temblores a distancias moderadas y grandes”, *Boletín Sociedad Mexicana de Ingeniería Sísmica*, 2:1–18, 1964, In Spanish
- [67] Housner, G. “*Engineering Seismology*”, 1965
- [68] Snaebjornsson, J.T.; and Sigbjornsson, R. “The duration characteristics of earthquake ground motions”, *The 14th World Conference on Earthquake Engineering*, Beijing, China, 2008
- [69] Hwang, H.; Lin, C.K.; and Yeh, Y.T. “Derivation of attenuation relations of Arias intensity using the Chi-Chi earthquake data”, *13th World Conference on Earthquake Engineering*, Vancouver, B.C., Paper No. 3108, Canada, 2004
- [70] Peng, J., and Shao, X., Zhang, J. (2010) “Climate change, CO2 emission scenarios and effects on carbonation-induced cracking and time-dependent reliability of concrete structures” *China Civil Engineering Journal*, 43(6), 74-81
- [71] Stewart, M.G., Wang, X., and Nguyen, M.N. (2011) “Climate change impact and risks of concrete infrastructure deterioration” *Engineering Structures*, 33(4), 1326-1337
- [72] Chi, J.M., Huang, R., and Yang, C.C. (2002) “Effects of Carbonation on Mechanical Properties and Durability of Concrete Using Accelerated Testing Method” *Journal of Marine Science and Technology*, 10(1), 14-20
- [73] Sagüés, A.A., Moreno, E.I., Morris, W., and Andrade, C. (1997) “Carbonation in Concrete and Effect on Steel Corrosion” *Florida Department of Transportation, Final Report, State Job No. 99700-3530-119, WPI 0510685*
- [74] Enright, M.P., and Frangopol, D.M. (1998) “Service-life prediction of deteriorating concrete bridges” *J. Struct. Eng.*, 10.1061/(ASCE)0733-9445 (1998) 124:3(309), 309-317
- [75] Melchers, R.E. (2003) “Probabilistic models for corrosion in structural reliability assessment part 2: models based on mechanics” *Journal of offshore mechanics and arctic engineering*, 125,272-280
- [76] Ellingwood, B.R. (2005) “Risk-informed condition assessment of civil infrastructure: state of practice and research issues” *Structure and Infrastructure Engineering*, 1, 7-18
- [77] Gerhards, C. C. (1982) “Effect of moisture content and temperature on the mechanical properties of wood: an analysis of immediate effects”, *Wood and fiber*, 14(1), 4-36
- [78] Saini, A., and Tien, I., “Impacts of climate change on the assessment of long-term structural reliability” *ASCE-ASME Journal of Risk and Uncertainty in Engineering Systems*, Vol. 3, No. 3, September 2017

- [79] Possan, E., and de Oliveira Andrade, J., “Markov chains and reliability analysis for reinforced concrete structure service life” *Materials Research*, vol. 17, issue 3, 593-602, 2014
- [80] Feng, Z., “Markov chains applied to degradation modeling” thesis, NTNU
- [81] Kumar, R., and Gardoni, P., “Modeling structural degradation of RC bridge columns subjected to earthquakes and their fragility analysis” *Journal of Structural Engineering*, vol. 138, Issue 1, January 2012
- [82] Golgoon, A., and Yavari, A., “Nonlinear elastic inclusions in anisotropic solids” *Journal of Elasticity*, vol. 130, issue 2, 239-269, February 2018
- [83] Lu, Y.B.; and Li, Q.M., “About the dynamic uniaxial tensile strength of concrete-like materials” *International Journal of Impact Engineering*, vol. 38, issue 4, 171-180, April 2011
- [84] Karsan, I.D.; and Jirsa, J.O., “Behavior of concrete under compressive loadings” *Journal of the Structural Design*, vol. 95, 2543-2563, December 1969
- [85] Pijanowski, B.S.; and Mahmud, I., “A study of the effects of temperature and oxygen content on the corrosion of several metals” Report 69-2, Cooperative Program in Ocean Engineering, N00014-67-A-0377-003, June 1969
- [86] Chi, J.M.; Huang, R.; and Yang, C.C., “Effects of carbonation on mechanical properties and durability of concrete using accelerated testing method” *Journal of Marine Science and Technology*, vol. 10, no. 1, 14-20, 2002
- [87] Mu, R.; Miao, C.; Luo, X.; and Sun, W., “Interaction between loading, freeze-thaw cycles, and chloride salt attack of concrete with and without steel fiber reinforcement” *Cement and Concrete Research*, vol. 32, issue 7, 1061-1066, July 2002
- [88] Park, Y.S.; Suh, J.K.; Lee, J.H.; and Shin, Y.S., “Strength deterioration of high strength concrete in sulfate environment” *Cement and Concrete Research*, vol. 29, issue 9, 1397-1402, September 1999
- [89] Swamy, R.N.; and Al-Asali, M.M., “Engineering properties of concrete affected by alkali-silica reaction” *Materials Journal*, vol. 85, issue 5, 367-374, September 1988
- [90] Roy, D.M.; Arjunan, P.; and Silsbee, M.R., “Effect of silica fume, metakaolin, and low-calcium fly ash on chemical resistance of concrete” *Cement and Concrete research*, vol. 31, issue 12, 1809-1813, December 2001
- [91] Naus, D.J., “The effect of elevated temperatures on concrete materials and structures” Oak Ridge National Laboratory, Oak Ridge, TN, US Nuclear Regulatory Commission, 1886-N674-1Y, November 2005
- [92] Liu, Y.W.; Yen, T.; and Hsu, T.H., “Abrasion-erosion of concrete by water-borne sand” *Cement and Concrete Research*, vol. 36, issue 10, 1814-1820, October 2006
- [93] Ueda, T.; Hasan, M.; Nagai, K.; and Sato, Y., “Stress-strain relationship of concrete damaged by freezing and thawing cycles” *Journal of Advanced Concrete Technology*, vol. 2, issue 1, 89-99, February 2004
- [94] Koh, S.K.; and Stephens, R.I., “Mean stress effects on low cycle fatigue for a high strength steel” *Fatigue and Fracture of Engineering materials and Structures*, vol. 14, issue 4, 413-428, April 1991

- [95] Wang, W.Y.; Liu, B.; and Kodur, V., “Effect of temperature on strength and elastic modulus of high-strength steel” *Journal of Materials in Civil Engineering*, vol. 25, issue 2, 174-182, February 2013
- [96] Gerhards, C. C. “Effect of moisture content and temperature on the mechanical properties of wood: an analysis of immediate effects”, *Wood and fiber*, 14(1):4-36, 1982
- [97] Bonfield, P.W.; and Ansell, M.P., “Fatigue properties of wood in tension, compression, and shear” *Journal of Materials Science*, vol. 26, issue 17, 4765-4773, September 1991
- [98] Walther, T.; Kartal, S.N.; Hwang, W.J.; Umemura, K.; and Kawai, S., “Strength, decay and termite resistance of oriented kenaf fiberboards” *Journal of Wood Science*, vol. 53, issue 6, 481-486, December 2007
- [99] Akkouchi, M. “On the convolution of exponential distributions” *Journal of the Chungcheong Mathematical Society*, vol. 21, no. 4, December 2008
- [100] Cherruault, Y., and Adomian, G. “Decomposition methods: a new proof of convergence” *Mathematical Computational Modeling*, vol. 18, no. 12, 103-106, 1993
- [101] Portnoy S. “Asymptotic behavior of likelihood methods for exponential families when the number of parameters tends to infinity” *The Annals of Statistics*, vol. 16, no. 1, 356-366, March 1988
- [102] Saini, A.; and Tien, I. “Framework for probabilistic assessment of maximum nonlinear structural response based on sensor measurements: discretization and estimation”, *ASCE Journal of Engineering Mechanics*, vol. 143, issue 9, 2017
- [103] Saini, A.; and Tien, I. “Methodology for real time prediction of structural seismic risk based on sensor measurements”, *Structural Safety*, vol. 73, 54-63, July 2018
- [104] Bruneau, M.; Chang, S.E.; and Eguchi, R.T. et al “A framework to quantitatively assess and enhance the seismic resilience of communities” *Earthquake Spectra*, 19(4), 737-8, 2006
- [105] US Department of Homeland Security, *National Infrastructure Protection Plan, partnering to enhance protection and resiliency*, 2009
- [106] Haimes, Y. “On the definition of resilience In systems” *Risk Analysis*, 29(4), 498-501, 2009
- [107] Cimellaro, G.; Reinhorn, A.; and Bruneau, M. “Seismic resilience of a hospital system” *Structural Infrastructure Engineering*, 6(1), 127-144, 2010
- [108] Chang, S.E.; and Shinozuka, M. “Measuring improvements in the disaster resilience of communities” *Earthquake Spectra*, 20(3), 739-755, 2004
- [109] Vugrin, E.D.; Warren, D.E.; Ehlen, M.A., and Camphouse, R.C. “A framework for assessing the resilience of infrastructure and economic systems” In: Kasthurirangan C, Gopalakrishnan, Srinivas Peeta, editors, *Sustainable and Resilient Infrastructure Systems: Simulation, Modeling, and Intelligent Engineering*, Berlin: Springer-Verlag, Inc., 2010
- [110] Ouyang, M.; Duenas-Osorio, L.; and Min, X. “A three stage resilience analysis framework for urban infrastructure systems” *Structural Safety*, 36, 23-31, 2012